The Influence of Mesoscale Eddies on the Internal Tide

by

Michael Dunphy

A thesis
presented to the University of Waterloo
in fulfillment of the
thesis requirement for the degree of
Master of Mathematics
in
Applied Mathematics

Waterloo, Ontario, Canada, 2009

I hereby declare that I am the sole author of this thesis. This is a true copy of the thesis, including any required final revisions, as accepted by my examiners.

I understand that my thesis may be made electronically available to the public.

Abstract

The barotropic tide dissipates a well established estimate of 2.5 TW of energy at the M_2 frequency. Bottom topography is responsible for part of this dissipation, and the generation of the internal tide is also partly responsible. The fate of this energy is largely described by a cascade from large scales to small scales by non-linear wave-wave interactions where it gets dissipated.

This thesis aims to investigate how the presence of mesoscale eddies (vortices) in the ocean affect the internal tide. Previous work has looked at the interaction of the barotropic tide with eddies. Krauss (1999) found that the interaction can produce a modulated internal tide, however a scaling analysis suggests that the effect may not be as strong as reported.

The MITgcm is used to simulate internal wave generation by barotropic flow over topography and comparisons are made with Dr. Lamb's IGW model. Baroclinic eddies are analytically prescribed and then geostrophically adjusted also using the MITgcm. Finally, the two are combined, and the internal tide field is analysed with and without the presence of eddies of various magnitude and length scales.

The results of this investigation do not find a strong transfer of energy between modes; the modal distribution of energy in the internal tide remains the same when an eddy is added. However, focusing and shadow beams of internal waves are produced in the wake of an eddy as the internal waves pass through it. The beams show very strong variations in intensity, vertically integrated energy flux can reduce almost to zero in the shadow regions and increase more than double in the focusing regions.

Modal decomposition of the horizontal flow field reveals that mode 2 and 3 waves are most strongly affected by the eddies and contribute strongly to the formation of the beams. Mode 1 appears to be less affected by the eddy. The larger wavelength and faster group velocity of mode 1 supports the notion that the eddy interacts with it less.

Acknowledgements

Thanks to my father Paul Dunphy for his unwavering encouragement and thanks to the rest of my family for their invaluable support, without which this thesis would not have been possible. I would also like to thank my supervisor Dr. Lamb for his guidance and enthusiasm in learning this material and preparing this thesis. Thanks also to my friends and colleagues who have helped me along the way including Dr. Stastna, Dr. Poulin, Tim Rees, Christopher Subich, Derek Steinmoeller, Wentao Liu, Georges Djoumna and Volodymyr Gerasik. Finally thanks also to my housemates Alex Shum, Antonio Sanchez and Ben Turnbull for being such wonderful friends.

Contents

List of Tables

List of Figures

Chapter 1

Introduction

The purpose of this thesis is to investigate the interaction of internal waves with mesoscale eddies. Internal gravity waves of tidal frequency (internal tides) are generated by barotropic tides flowing over topography and represents a conversion of energy from barotropic to baroclinic modes. The length scales of such waves are tens to hundreds of kilometres. These waves interact with other features in the ocean including other internal waves, and the energy cascades to small scales where it is dissipated. The interaction of interest here is that with oceanic mesoscale eddies. Such eddies are typically generated by meandering jets such as the Gulf Stream and can be observed year round in the ocean. A typical mesoscale eddy is 50-200 km in radius and can penetrate several kilometres deep into the ocean.

Work by Krauss (1999) suggests that the interaction of eddies and the barotropic tide can result in the generation of a modulated baroclinic tide. However by considering the scales of these phenomena, such an interaction may not be as significant as proposed. The barotropic tides are typically basin-scale (order 1000-5000 km) and mesoscale eddies much smaller (50-200 km). Thus it is expected that eddies will be primarily advected by the barotropic tide without transfer of energy.

The total global rate at which M_2 tidal energy is dissipated is a well determined value of 2.5 ± 0.1 TW (Ray, 1997). However the details of how this energy is accounted for is less clear. Bottom topography and conversion to baroclinic modes are two agents responsible for a sizable chunk of the energy. The fate of the baroclinic energy is largely dissipation at small scales after cascading downscale, however some may be transferred to eddies. Eddies such as Gulf Stream rings are often reabsorbed into the Gulf Stream and this may be a secondary fate for internal tide energy.

Chapter 2

Background

This chapter presents background material needed and describes techniques used to investigate the interaction of eddies with internal waves. The first section is a summary of the equations of motion that describe fluid flow on a rotating sphere. The next section deals with internal waves; observational information, theory and techniques used to analyse such waves is provided. Mesoscale eddies are described in the third section including observations and their connection to quasigeostrophic theory. The fourth and final section is concerned with the MITgcm (Massachusetts Institute of Technology's General Circulation Model), the numerical model chosen to conduct numerical experiments in this investigation.

2.1   Equations of motion

The equations of motion governing idealised oceanic flow on a rotating sphere that we consider are

$$\rho \frac{D\vec{u}}{Dt} + \rho 2\vec{\Omega} \times \vec{u} = -\nabla p + \rho \vec{g} + \mu \nabla^2 \vec{u}, \tag{2.1}$$

$$\frac{1}{\rho}\frac{D\rho}{Dt} + \vec{\nabla} \cdot \vec{u} = 0, \tag{2.2}$$

$$\frac{DT}{Dt} = \kappa_T \nabla^2 T, \tag{2.3}$$

$$\frac{DS}{Dt} = \kappa_S \nabla^2 S, \tag{2.4}$$

$$\rho = \rho(S, T), \tag{2.5}$$

where $\vec{u}(x, y, z, t) = (u, v, w)$ is the velocity field, $\rho = \rho(x, y, z, t)$ is the density field, $p = p(x, y, z, t)$ is the pressure field, $S = S(x, y, z, t)$ is the salinity field, $T = T(x, y, z, t)$ is the temperature field, $\vec{\Omega} = (0, \Omega \cos\theta, \Omega \sin\theta)$ where θ is latitude, $\vec{g} = (0, 0, -g)$ is the gravitational acceleration constant, μ is the coefficient of

dynamic viscosity, κ_T is the thermal diffusivity, κ_S is the coefficient of salt diffusion, $\nabla = \frac{\partial}{\partial x} + \frac{\partial}{\partial y} + \frac{\partial}{\partial z}$ is the vector differentiation operator and $\frac{D}{Dt} = \frac{\partial}{\partial t} + \vec{u} \cdot \vec{\nabla}$ is the material derivative.

The first equation (2.1) is the momentum equation. On the left hand side, the first term is the rate of change of velocity of a fluid particle. The second term is the Coriolis force that accounts for the effects of rotation. On the earth,

$$\Omega = \frac{2\pi}{24 \times 60 \times 60} \approx 0.727 \times 10^{-4} \, \text{rad} \, s^{-1}, \tag{2.6}$$

which corresponds to one rotation every 24 hours.

On the right hand side, the first term is the pressure gradient, a vector field resulting from the gradient operator acting on the scalar pressure field. The second term is gravitational acceleration and only acts in the vertical direction. The third term accounts for viscosity that acts to dissipate small scale motion at molecular length scales.

The second equation (2.2) is the continuity equation which states that mass is conserved. A net flow of fluid into or out of a fixed volume must be associated with a corresponding change in density, in the absence of any mass sources or sinks.

The third equation (2.3) is the energy equation. All sources of thermal energy are ignored in this form; heat is conserved following the flow with the exception of diffusivity. The coefficient κ_T is assumed to be spatially constant.

The fourth equation (2.4) states that salt is conserved. Any change in salt concentration is balanced by molecular diffusion of salt. Again we assume the coefficient κ_S is spatially constant.

The fifth equation (2.5) is the equation of state that relates density ρ to the active tracers T and S. In this thesis we use the linear equation of state,

$$\rho(T, S) = \rho_0(1 - \alpha(T - T_0) + \beta(S - S_0)), \tag{2.7}$$

where $\rho_0 = 1028$ kg m^{-3}, $T_0 = 10\,^oC$ and $S_0 = 35$ psu are values for reference density, temperature, and salinity; T is the temperature, S is the salinity, $\alpha = 1.7 \times 10^{-4}\,^oC^{-1}$ is the thermal expansion coefficient and $\beta = 7.6 \times 10^{-4}$ psu^{-1} is the haline contraction coefficient. The linear equation of state is suitable for this thesis because perturbations of T and S from their reference values are small, although it is less suitable for use in a global ocean model where variations are much larger.

2.1.1   f-plane approximation

When studying regions much smaller than the sphere it is typical to make the f-plane approximation. This approximation states that the rate of rotation is constant over the domain rather than varying as sine of latitude as is the case on a sphere. Further, the meridional component of $\vec{\Omega}$ (also called the non-traditional

component) is dropped and only the vertical component (the traditional component) is retained. The definition $f = 2\Omega \sin\theta$ is made and the second term in (2.1) is reduced to $\vec{f} \times \vec{u}$, where $\vec{f} = (0, 0, f)$.

2.1.2   Oceanic approximations

In the ocean we can use the Boussinesq approximation to simplify the equations of motion. The approximation states that variations in density are quite small and can be neglected everywhere except in the momentum equation's gravitational acceleration term (buoyancy term) containing $\vec{g}$. We rewrite the density as $\rho = \rho_0 + \rho'(x, y, z, t)$ asserting that $|\rho'| \ll \rho$. Substituting this into the continuity equation (2.2) yields

$$\frac{D\rho'}{Dt} + \rho_0(\vec{\nabla} \cdot \vec{u}) + \rho'(\vec{\nabla} \cdot \vec{u}) = 0. \tag{2.8}$$

We notice that the third term is much smaller than the second and neglect it due to the assumption $|\rho'| \ll \rho$. The two remaining terms must make up the dominant balance. Expanding the second term yields

$$\frac{D\rho'}{Dt} + \rho_0 \left(\frac{\partial u}{\partial x} + \frac{\partial v}{\partial y} + \frac{\partial w}{\partial z} \right) = 0. \tag{2.9}$$

Making the incompressibility approximation states that the dominant balance in the continuity equation is achieved by the three terms that make up the divergence term,

$$\vec{\nabla} \cdot \vec{u} = 0, \tag{2.10}$$

which is called the incompressible form of the continuity equation.

Similarly we substitute $\rho = \rho_0 + \rho'(x, y, z, t)$ into the momentum equation, yielding

$$(\rho_0 + \rho')\frac{D\vec{u}}{Dt} + (\rho_0 + \rho')2\vec{\Omega} \times \vec{u} = -\nabla p + (\rho_0 + \rho')\vec{g} + \mu\nabla^2\vec{u}. \tag{2.11}$$

As mentioned before, in every term except the gravitational acceleration term we remove the perturbation part which simplifies to

$$\rho_0\frac{D\vec{u}}{Dt} + \rho_0 2\vec{\Omega} \times \vec{u} = -\nabla p + (\rho_0 + \rho')\vec{g} + \mu\nabla^2\vec{u}. \tag{2.12}$$

Now we write the pressure as $p = p_0 + p'$ where p_0 is in hydrostatic balance with $\rho_0 g$, i.e.

$$\frac{\partial p_0(z)}{\partial z} = \rho_0\vec{g}, \tag{2.13}$$

4

and subtract this from the momentum equation. Dividing by ρ_0 we get

$$\frac{D\vec{u}}{Dt} + 2\vec{\Omega} \times \vec{u} = -\frac{1}{\rho_0}\nabla p' + \frac{\rho'}{\rho_0}\vec{g} + \nu\nabla^2\vec{u}. \tag{2.14}$$

where we have defined $\nu = \frac{\mu}{\rho_0}$ as the coefficient of kinematic viscosity. Applying the f-plane approximation leaves us with the viscous diffusive incompressible Boussinesq equations,

$$\frac{D\vec{u}}{Dt} + \vec{f} \times \vec{u} = -\frac{1}{\rho_0}\nabla p' + \frac{\rho'}{\rho_0}\vec{g} + \nu\nabla^2\vec{u}, \tag{2.15}$$

$$\vec{\nabla} \cdot \vec{u} = 0, \tag{2.16}$$

$$\frac{DT}{Dt} = \kappa_T\nabla^2 T, \tag{2.17}$$

$$\frac{DS}{Dt} = \kappa_S\nabla^2 S, \tag{2.18}$$

$$\rho = \rho(S, T). \tag{2.19}$$

We can further simplify by assuming that the flow is inviscid ($\nu = 0$) and non-diffusive ($\kappa_T = \kappa_S = 0$). Taking the material derivative of (2.19) and substituting (2.17) and (2.18) yields a familiar form of the incompressible Boussinesq equations:

$$\frac{D\vec{u}}{Dt} + \vec{f} \times \vec{u} = -\frac{1}{\rho_0}\nabla p' + \frac{\rho'}{\rho_0}\vec{g}, \tag{2.20}$$

$$\vec{\nabla} \cdot \vec{u} = 0, \tag{2.21}$$

$$\frac{D\rho}{Dt} = 0. \tag{2.22}$$

$$\tag{2.23}$$

2.1.3 Hydrostatic approximation

The hydrostatic approximation is concerned with the non-viscous linearised vertical momentum equation,

$$\rho_0\frac{\partial w}{\partial t} = -\frac{\partial p'}{\partial z} + \rho'g. \tag{2.24}$$

The hydrostatic approximation consists of assuming that the acceleration of vertical velocity on the left hand side is much smaller in magnitude than both the vertical pressure gradient and gravitational acceleration on the right. A scaling analysis provides insight as to when this approximation is valid. Let L and H be vertical length scales and T be a time scale. The horizontal velocity scales by

$V \approx L/T$ and vertical velocity by $W \approx H/T$ or $W \approx HV/L$. By the horizontal momentum equation (neglecting the Coriolis term) we have a scaling for the pressure perturbation, $\Delta P \approx \rho_0 V^2$. Finally by assuming that the two terms on the left hand side of the vertical momentum equation are similar in magnitude we have a scaling for the density perturbation, $\Delta \rho \approx V^2 \rho_0 / gH$. Substituting these scalings and eliminating T on the right hand side yields

$$\rho_0 \frac{HV^2}{L^2} \ll \frac{V^2 \rho_0}{H} \approx \frac{V^2 \rho_0}{H}, \tag{2.25}$$

and dividing by the left hand side leaves the requirement that

$$\frac{H^2}{L^2} \ll 1. \tag{2.26}$$

Thus, the hydrostatic approximation holds for "thin" flows where the aspect ratio H/L is small. By dominant balance we can neglect the left hand side term and the pressure is determined from the remaining terms:

$$\frac{1}{\rho_0} \frac{\partial p'}{\partial z} \approx \frac{\rho'}{\rho_0} g, \tag{2.27}$$

$$p'(z) = \int_z^\eta \rho' g \, dz, \tag{2.28}$$

where η is the sea surface height. This pressure is the hydrostatic pressure. This approximation is widely used in numerical models because it is a computationally cheap way to compute the pressure field. The hydrostatic method requires the vertical integration of (2.28) and the inversion of a 2-D Laplacian, whereas the non-hydrostatic method requires inverting a 3-D Laplacian. Models that use the non-hydrostatic method typically require about one order of magnitude in increased computing time to solve a given problem.

2.1.4 Brunt-Väisälä frequency

Consider a linearly stratified fluid at rest. Now imagine that one were to raise a parcel of water by a small amount. The parcel of water is now surrounded by less dense water than itself and experiences a gravitational restoring force acting on it downwards. Assume now that the parcel is released; it will accelerate downwards. The parcel will move downwards, overshooting its original position, at which point it will be surrounded by denser water. The restoring force reverses, now directed upward and works to stop the parcel's downward motion and induce upward motion. The parcel will oscillate indefinitely (or until dissipative effects stop it) at a fixed rate; a rate dependant on the strength of the restoring force. This rate is known as the Brunt-Väisälä frequency (also called buoyancy frequency). Under

the Boussinesq approximation the Brunt-Väisälä frequency $N(z)$ is related to the density by

$$N^2(z) = -\frac{g}{\rho_0}\frac{\partial \bar{\rho}(z)}{\partial z}.$$ (2.29)

where $\bar{\rho}(z)$ is the undisturbed density profile.

2.2 Internal gravity waves

Internal gravity waves are phenomena that exist in stratified fluids when density surfaces are displaced. Such a wave can exist due to the gravitational restoring force acting on the vertically displaced fluid. Fluid with non-constant density is needed to support these waves.

There are numerous types of internal waves; some are oscillatory with a characteristic frequency such as internal tides, others exist as dispersive wave packets that separate as they propagate. One interesting type of internal wave is called a solitary wave - a nonlinear wave that does not change its shape as it propagates. All of these waves exist in the interior of the ocean, unlike surface waves that exist at the boundary between the ocean and the atmosphere. (Technically the atmosphere-ocean boundary is an infinitesimally thin pycnocline with a large density jump across it. Surface waves are different enough from internal waves to be their own variety).

Although internal waves exist within the interior of the ocean they are sometimes large enough to be observed in the sea surface elevation. The relative density of air compared to water is order 10^{-3} so it requires roughly 1000 times as much energy to raise the sea surface than it does to raise an internal isopycnal by the same distance (Ray, 1997). Hence many internal waves produce very small sea surface signatures and are unobservable due to noise. However exceptionally large internal waves may produce a 10 cm or larger sea-surface signal. This signal modulates the sea-surface and changes the way light/radar is reflected. It is these changes that are detectable from a satellite. An example of such surface visible internal waves was imaged by NASAs Terra satellite and is shown in Figure 2.1.

2.2.1 Generation

Energy may be imparted into internal waves in the interior of the ocean through many mechanisms. Thorpe (1975) looks at generation mechanisms and finds that travelling pressure and wind stress fields (such as atmospheric storm systems), and interacting surface waves are among surface sources. At the bottom, tidal flow over bottom topography produces the internal tide and constant flow over topography can produce lee waves. For example, Ray (1997) finds that at the Hawaiian Ridge 15 GW of energy is converted from the barotropic M_2 tide to the mode 1 internal tide of the same frequency. Other mesoscale processes existing in the interior of the

7
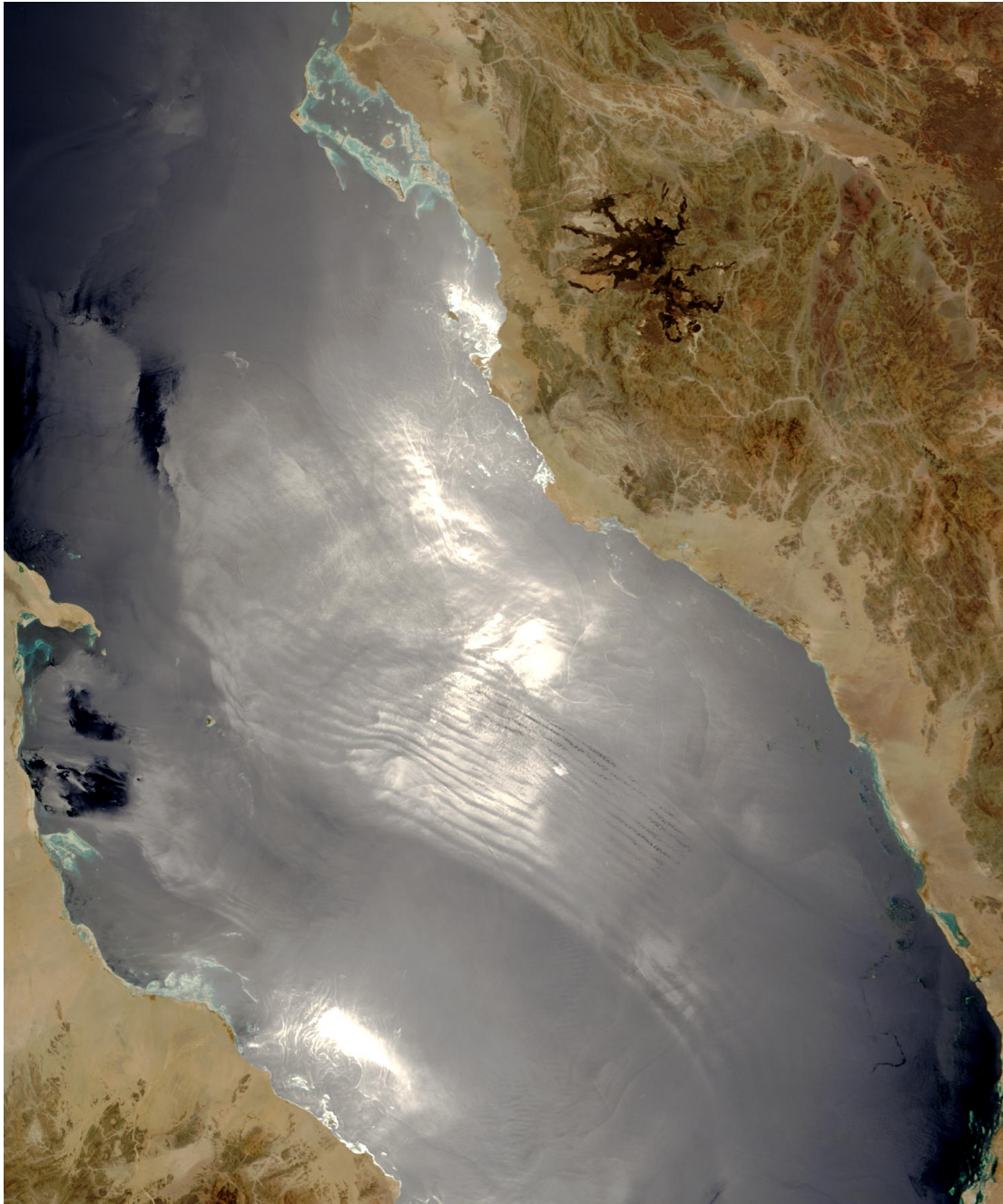
Figure 2.1: Internal waves observed in the Red Sea by the MODIS sensor on NASA's Terra satellite on 26 July 2003. Egypt is on the west and Saudi Arabia is on the east. Figure reproduced from `http://visibleearth.nasa.gov/view_rec.php?id=5805`
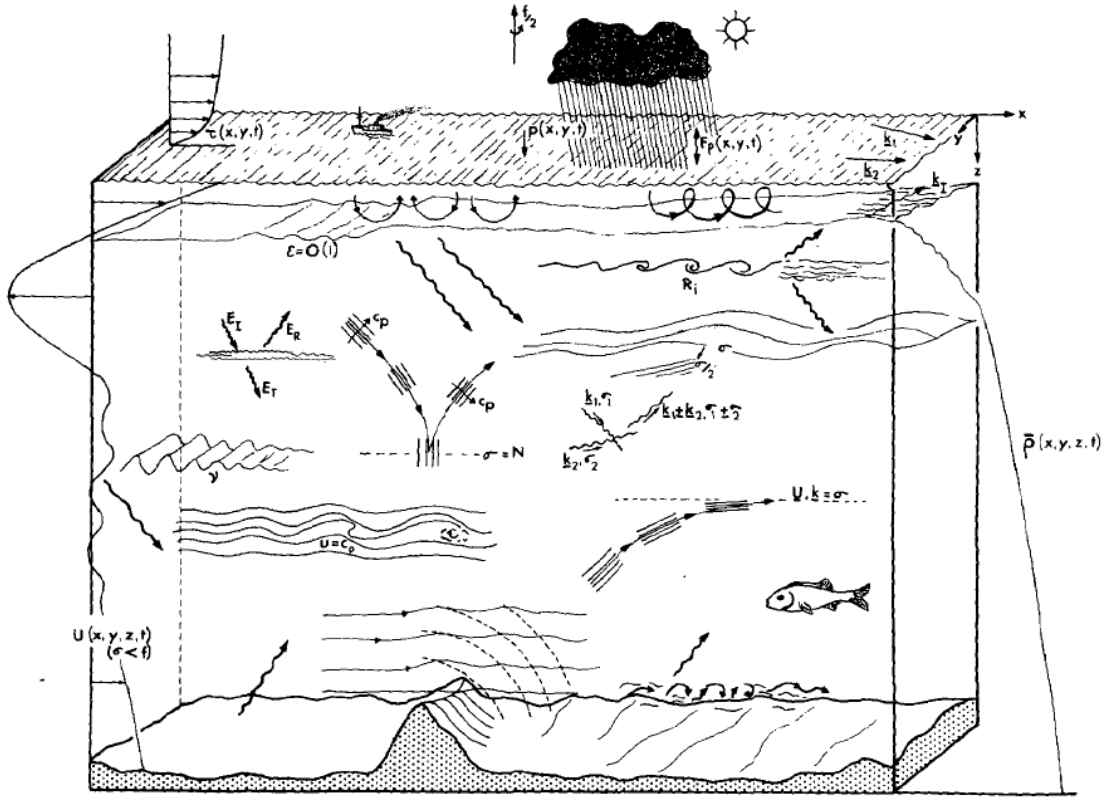
Figure 2.2: Generating mechanisms for internal gravity waves. Illustration reproduced from Thorpe (1975).

ocean are candidates for producing internal waves including eddies which generate internal waves as they adjust. Figure 2.2 illustrates many of the mechanisms for producing internal waves.

Energy is continually injected into the internal wave field, and nonlinear interactions between waves cause energy to be transferred between length scales and frequencies. This is believed to at least partly explain the Garrett-Munk internal wave spectrum that describes the distribution of energy over wavenumber and frequency space.

2.2.2 Garrett-Munk spectrum

The GM79 spectrum (Garrett and Munk, 1979) is a model designed to describe the distribution of energy in the ocean's internal wave field in wavenumber-frequency space. The model is based on observations collected from a variety of sources such as moored sensors, towed sensors and lowered sensors. The objective of the model is to describe the "typical" internal wave conditions that one would expect at a random location in the open ocean.
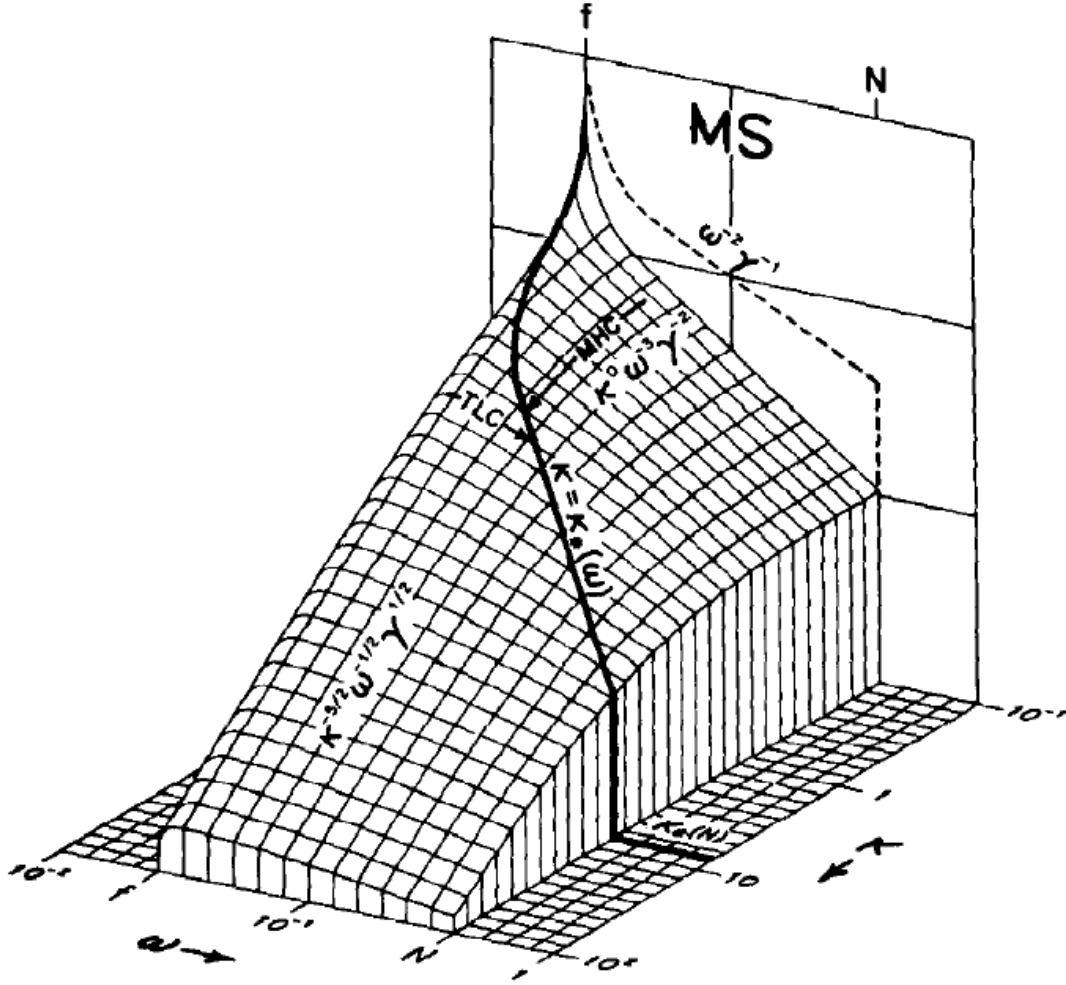
Figure 2.3: The frequency-horizontal wavenumber spectrum from GM79. Note that energy is constrained to be above the inertial frequency f and below the buoyancy frequency N. Reproduced from Garrett and Munk (1979).

The GM79 model makes the assumption that the internal wave spectrum is isotropic with respect to horizontal wavenumber. The distribution of vertical displacement, horizontal velocity and energy per unit mass are described in Munk (1981). A summary of the internal wave energy spectrum is shown in Figures 2.3 and 2.4. The relative energy density is shown as a function of frequency and (vertical or horizontal) wavenumber. Note that there is no energy above N (the buoyancy frequency) or below f (the inertial frequency). This is consistent with the expectation from the dispersion relation for internal waves - more on this later. The figures show that the highest energy is in the low wavenumbers and near the inertial frequency and the lowest energy at large wavenumbers near the buoyancy frequency.
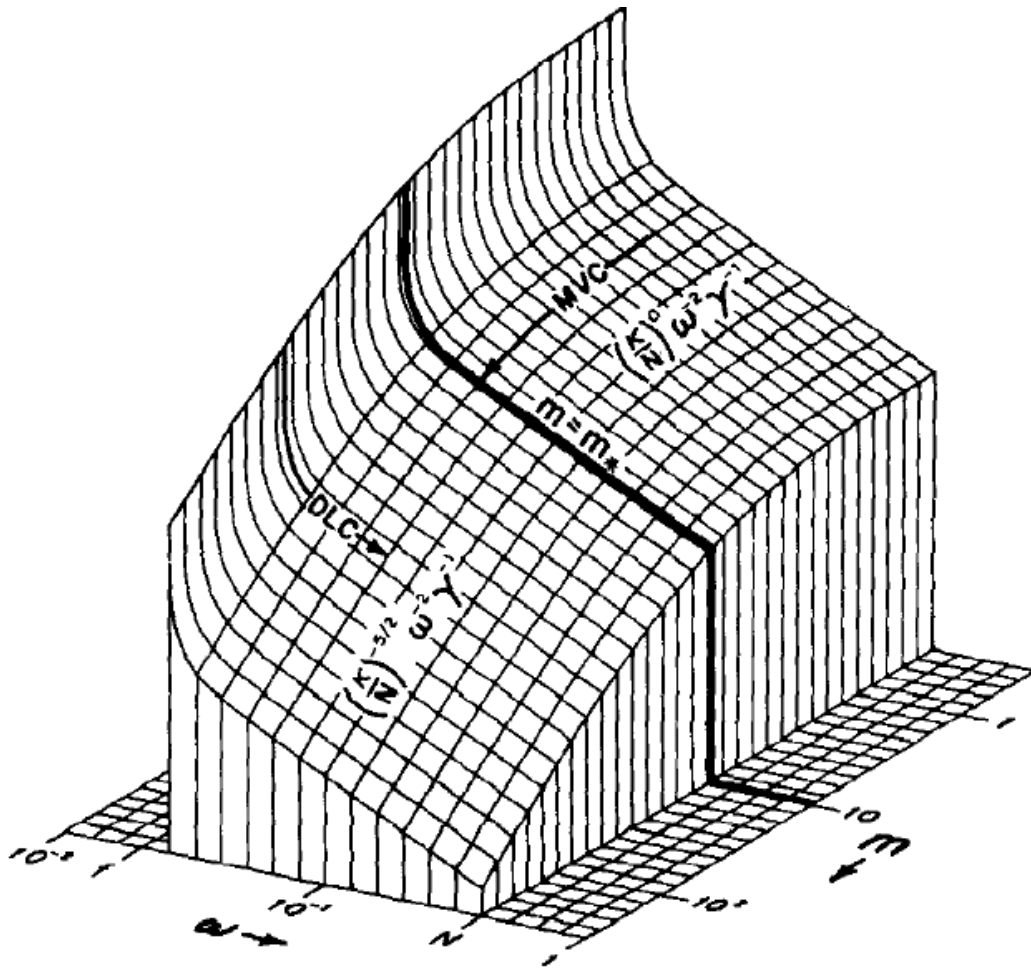
Figure 2.4: The frequency-vertical wavenumber spectrum from GM79. Reproduced from Garrett and Munk (1979).

2.2.3 Linearised equations

The equations described in section 2.1.2 can be simplified in order to find linear solutions describing small amplitude internal waves. We assert that we are interested in small amplitude signals and linearise about $(u, v, w, \rho, p) = (0, 0, 0, \bar{\rho}, \bar{p})$ where $d\bar{p}/dz = -g\bar{\rho}$, by adding $O(\epsilon)$ perturbations and retaining the $O(\epsilon)$ terms. This leaves us with a simplified set of equations

$$\frac{\partial u}{\partial t} - fv = -\frac{1}{\rho_0}\frac{\partial p'}{\partial x}, \tag{2.30}$$

$$\frac{\partial v}{\partial t} + fu = -\frac{1}{\rho_0}\frac{\partial p'}{\partial y}, \tag{2.31}$$

$$\frac{\partial w}{\partial t} = -\frac{1}{\rho_0}\frac{\partial p'}{\partial z} - \frac{g}{\rho_0}\rho', \tag{2.32}$$

$$\frac{\partial u}{\partial x} + \frac{\partial v}{\partial y} + \frac{\partial w}{\partial z} = 0, \tag{2.33}$$

$$\frac{\partial \rho'}{\partial t} + w\frac{\partial \bar{\rho}}{\partial z} = 0. \tag{2.34}$$

We are interested in wave solutions so we wish to derive a wave equation describing internal waves. The first step is to take the horizontal divergence $(\nabla_H = (\frac{\partial}{\partial x}, \frac{\partial}{\partial y}))$ of the horizontal momentum equations, yielding

$$\frac{\partial}{\partial t}\left(\frac{\partial u}{\partial x} + \frac{\partial v}{\partial y}\right) + f\left(\frac{\partial u}{\partial y} - \frac{\partial v}{\partial x}\right) = -\frac{1}{\rho_0}\left(\frac{\partial^2 p'}{\partial x^2} + \frac{\partial^2 p'}{\partial y^2}\right). \tag{2.35}$$

Next we take the curl of the horizontal momentum equations

$$\frac{\partial}{\partial t}\left(\frac{\partial v}{\partial x} - \frac{\partial u}{\partial y}\right) + f\left(\frac{\partial u}{\partial x} + \frac{\partial v}{\partial y}\right) = -\frac{1}{\rho_0}\left(\frac{\partial^2 p'}{\partial x \partial y} - \frac{\partial^2 p'}{\partial y \partial x}\right) = 0. \tag{2.36}$$

Solving (2.35) for $(\frac{\partial v}{\partial x} - \frac{\partial u}{\partial y})$ and substituting into (2.36) as well as using (2.33) gives

$$\frac{\partial}{\partial z}\left(\frac{\partial^2 w}{\partial t^2} + f^2 w\right) = -\frac{1}{\rho_0}\frac{\partial}{\partial t}\left(\frac{\partial^2 p'}{\partial x^2} + \frac{\partial^2 p'}{\partial y^2}\right). \tag{2.37}$$

Taking $\frac{\partial}{\partial t}$ of the vertical momentum equation and substituting into the density equation produces

$$\frac{\partial^2 w}{\partial t^2} - \frac{g}{\rho_0}w\frac{\partial \bar{\rho}}{\partial z} = -\frac{1}{\rho_0}\frac{\partial^2 p'}{\partial z \partial t}. \tag{2.38}$$

Noticing that the second term contains the buoyancy frequency allows us to simplify

$$\frac{\partial^2 w}{\partial t^2} + N^2(z)w = -\frac{1}{\rho_0}\frac{\partial^2 p'}{\partial z \partial t}. \tag{2.39}$$

Taking $\frac{\partial}{\partial z}$ of (2.37) and taking both $\frac{\partial^2}{\partial x}$ and $\frac{\partial^2}{\partial y}$ of (2.39) and then adding the result gives

$$\frac{\partial^2}{\partial t^2}\left(\frac{\partial^2}{\partial x^2} + \frac{\partial^2}{\partial y^2} + \frac{\partial^2}{\partial z^2}\right)w + N^2(z)\left(\frac{\partial^2}{\partial x^2} + \frac{\partial^2}{\partial y^2}\right)w + f^2\frac{\partial^2}{\partial z^2}w = 0, \tag{2.40}$$

which is the non-hydrostatic wave equation for the vertical velocity of internal waves in a continuously stratified fluid on an f-plane. Making the hydrostatic approximation reduces this equation to

$$\frac{\partial^2}{\partial t^2}\left(\frac{\partial^2}{\partial z^2}\right)w + N^2(z)\left(\frac{\partial^2}{\partial x^2} + \frac{\partial^2}{\partial y^2}\right)w + f^2\frac{\partial^2}{\partial z^2}w = 0. \tag{2.41}$$

2.2.4 Internal wave energy

The energy equation for linear internal waves can be obtained (following Gill (1981)) as follows. First, multiply the momentum equations by $\rho_0 u$, $\rho_0 v$ and $\rho_0 w$ and multiply the continuity equation by $\frac{g^2\rho'}{\rho_0 N^2}$,

$$\rho_0 u(\frac{\partial u}{\partial t} - fv) = u(-\frac{\partial p'}{\partial x}), \tag{2.42}$$

$$\rho_0 v(\frac{\partial v}{\partial t} + fu) = v(-\frac{\partial p'}{\partial y}), \tag{2.43}$$

$$\rho_0 w(\frac{\partial w}{\partial t}) = w(-\frac{\partial p'}{\partial z} - g\rho'), \tag{2.44}$$

$$\frac{g^2\rho'}{\rho_0 N^2}(\frac{\partial \rho'}{\partial t} + w\frac{\partial \bar{\rho}}{\partial z}) = 0. \tag{2.45}$$

Now sum the equations to get

$$\rho_0\left(u\frac{\partial u}{\partial t} + v\frac{\partial v}{\partial t} + w\frac{\partial w}{\partial t}\right) + \frac{g^2\rho'}{\rho_0 N^2}\frac{\partial \rho'}{\partial t} + \frac{g^2\rho'}{\rho_0 N^2}w\frac{\partial \bar{\rho}}{\partial z} = -u\frac{\partial p'}{\partial x} - v\frac{\partial p'}{\partial y} - w\frac{\partial p'}{\partial z} - wg\rho'. \tag{2.46}$$

The last term on both sides are equal with use of the Brunt-Väisälä frequency equation (2.29). This simplifies to

$$\frac{\partial}{\partial t}\left(\frac{1}{2}\rho_0(u^2 + v^2 + w^2) + \frac{g^2\rho'^2}{\rho_0 N^2}\right) = p'\left(\frac{\partial u}{\partial x} + \frac{\partial v}{\partial y} + \frac{\partial w}{\partial z}\right) - \vec{\nabla}\cdot(p'\vec{u}). \qquad (2.47)$$

Using the incompressibility condition and moving the last term to the left hand side we get

$$\frac{\partial}{\partial t}\left(\frac{1}{2}\rho_0(u^2 + v^2 + w^2) + \frac{1}{2}\frac{g^2\rho'^2}{\rho_0 N^2}\right) + \vec{\nabla}\cdot(p'\vec{u}) = 0. \qquad (2.48)$$

The first three terms are identified with the kinetic energy and the fourth term with the available potential energy. The remaining three terms are energy flux terms. Thus the energy equation can be interpreted as a conservation equation; the rate of change of kinetic plus potential energy added to the rate that work is done by the pressure perturbation sums to zero.

2.2.5 Dispersion relation

If N is constant we can seek plane wave solutions of the form $w = e^{i(k_x x + k_y y + k_z z - \omega t)}$ and substitute this into the non-hydrostatic wave equation (2.40), yielding the dispersion relation

$$\omega^2 = \frac{N^2(k_x^2 + k_y^2) + f^2(k_z^2)}{k_x^2 + k_y^2 + k_z^2}. \qquad (2.49)$$

We observe from this dispersion relation that waves are horizontally isotropic. Further we notice that for a perfectly horizontal wave the frequency ω is N and for a perfectly vertical wave the frequency is f. Frequencies below f or above N cannot exist and hence N and f bound the oscillation rate of internal waves.

If we make the hydrostatic approximation and substitute instead into (2.41) we get the hydrostatic dispersion relation,

$$\omega^2 = \frac{N^2(k_x^2 + k_y^2) + f^2(k_z^2)}{k_z^2}. \qquad (2.50)$$

2.2.6 Vertically trapped solutions

Consider a horizontally unbounded ocean of constant depth with a rigid lid on top. The corresponding boundary conditions at the top and bottom will be no normal flow, or $w(0) = w(-H) = 0$. Internal waves in such an ocean will be vertically trapped in that they can only propagate horizontally. We seek horizontally propagating waves with vertical velocity of the form

$$w = W(z)e^{i(k_x x + k_y y - \omega t)}, \qquad (2.51)$$

and substitute this into the wave equation (2.40) yielding an eigenvalue problem for $W(z)$

$$\frac{\mathrm{d}W(z)}{\mathrm{d}z^2} + (k_x^2 + k_y^2)\left(\frac{N^2(z) - \omega^2}{\omega^2 - f^2}\right)W(z) = 0. \tag{2.52}$$

This eigenvalue problem describes the vertical structure of the horizontally propagating trapped waves. There are an infinite number of eigenfunctions that satisfy the eigenvalue problem and they are referred to as modes. The $N(z)$ need not be a constant and this means that the vertical structure depends on the ocean stratification.

The eigenvalue problem is modified under the hydrostatic approximation,

$$\frac{\mathrm{d}W(z)}{\mathrm{d}z^2} + (k_x^2 + k_y^2)\left(\frac{N^2(z)}{\omega^2 - f^2}\right)W(z) = 0. \tag{2.53}$$

2.2.7 Vertical eigenvalue problem

The vertical structure of the vertical velocity is thus described by the solution of the eigenvalue problem

$$\frac{\mathrm{d}\phi_n(z)}{\mathrm{d}z^2} + \kappa_n^2 Q^2(z)\phi_n(z) = 0, \tag{2.54}$$

$$\phi_n(0) = \phi_n(-H) = 0. \tag{2.55}$$

Here we assume that the frequency ω is a fixed parameter such that the eigenvalue is the horizontal wavenumber $\kappa_n^2 = k_x^2 + k_y^2$ and the eigenfunction $\phi_n(z)$ is the associated vertical structure. The dimensionless weighting function $Q^2(z)$ is

$$Q^2(z) = \begin{cases} \dfrac{N^2(z) - \omega^2}{\omega^2 - f^2} & \text{for non-hydrostatic,} \\ \dfrac{N^2(z)}{\omega^2 - f^2} & \text{for hydrostatic.} \end{cases} \tag{2.56}$$

The eigenvalue problem 2.54 can be easily solved for the case of constant N; by inspection we find solutions of the form $\phi_n = \sin(n\pi z/H), n = 0, 1, 2, ...$ However the variable $N(z)$ case will require a numerical approach and the method we choose follows (Talbot and Crampton, 2005) and is described in Section 2.2.12.

To obtain the orthogonality condition for pairs of $\phi_n(z)$, we multiply (2.54) by $\phi_m(z)$ and integrate over z

$$\int_{-H}^{0} \phi_n'' \phi_m + \kappa_n^2 Q^2 \phi_n \phi_m \, dz = 0. \tag{2.57}$$

15

Integrating the first term by parts yields

$$\phi_m \phi'_n \Big|_{-H}^{0} - \int_{-H}^{0} \phi'_n \phi'_m \, dz + \int_{-H}^{0} \kappa_n^2 Q^2 \phi_n \phi_m \, dz = 0. \tag{2.58}$$

The first term is zero by use of the boundary conditions. Integrating the middle term by parts yields

$$- \phi'_m \phi_n \Big|_{-H}^{0} + \int_{-H}^{0} \phi_n \phi''_m \, dz + \int_{-H}^{0} \kappa_n^2 Q^2 \phi_n \phi_m \, dz = 0. \tag{2.59}$$

As before the boundary conditions eliminate the first term. Switching n and m in (2.57) allows us to replace the second term resulting in

$$- \int_{-H}^{0} \kappa_m^2 Q^2 \phi_m \phi_n \, dz + \int_{-H}^{0} \kappa_n^2 Q^2 \phi_n \phi_m \, dz = (\kappa_n^2 - \kappa_m^2) \int_{-H}^{0} Q^2 \phi_n \phi_m \, dz = 0. \tag{2.60}$$

For the case of $m \neq n$ the integral must be zero as $(\kappa_n^2 - \kappa_m^2)$ is nonzero. For the $n = m$ case we rescale the eigenfunction such that the integral is unity. Thus we have the orthogonality condition

$$\int_{-H}^{0} Q^2 \phi_n \phi_m \, dz = \delta_{nm}. \tag{2.61}$$

Incidentally, we notice that equation (2.58) contains the orthogonality condition for the derivative of ϕ,

$$\int_{-H}^{0} \phi'_n \phi'_m \, dz = \int_{-H}^{0} \kappa_n^2 Q^2 \phi_n \phi_m \, dz = \kappa_n^2 \delta_{nm}. \tag{2.62}$$

2.2.8 Vertical modes

If we consider the constant N case, the vertical modes described above have vertical wavenumbers of the form

$$k_z = \frac{n\pi}{H}. \tag{2.63}$$

Substituting this into the dispersion relations (2.49) and (2.50) yields a new dispersion relation,

$$\omega^2 = \begin{cases} \dfrac{N^2 \kappa_h^2 H^2 + f^2 n^2 \pi^2}{\kappa_h^2 H^2 + n^2 \pi^2} & \text{for non-hydrostatic,} \\[4mm] \dfrac{N^2 \kappa_h^2 H^2 + f^2 n^2 \pi^2}{n^2 \pi^2} & \text{for hydrostatic,} \end{cases} \tag{2.64}$$

2.2.9 Phase speed

With constant N, the phase speed is found by dividing the frequency ω by the horizontal wavenumber κ_h yielding

$$c = \frac{\omega}{\kappa_h} = \begin{cases} \dfrac{H\omega}{n\pi}\sqrt{\dfrac{N^2-\omega^2}{\omega^2-f^2}} & \text{for non-hydrostatic,} \\[4mm] \dfrac{H\omega}{n\pi}\sqrt{\dfrac{N^2}{\omega^2-f^2}} & \text{for hydrostatic.} \end{cases} \tag{2.65}$$

where n is the wave's vertical mode and H is the water depth.

2.2.10 Group velocity

With constant N, we find the group velocity by differentiating the frequency ω with respect to wavenumber in the dispersion relation and yields

$$\vec{c_g} = \frac{\partial \omega}{\partial \vec{k}} = \begin{cases} \dfrac{H}{n\pi}\dfrac{(N^2-\omega^2)^{\frac{3}{2}}(\omega^2-f^2)^{\frac{1}{2}}}{\kappa_h\omega(N^2-f^2)}(k_x,k_y) & \text{for non-hydrostatic.} \\[4mm] \dfrac{H}{n\pi}\dfrac{N^3(\omega^2-f^2)^{\frac{1}{2}}}{\kappa_h\omega(N^2-f^2)}(k_x,k_y) & \text{for hydrostatic,} \end{cases} \tag{2.66}$$

2.2.11 Chebyshev pseudo spectral method

Chebyshev polynomials are a set of orthogonal polynomials defined over the region $[-1,1]$. These orthogonal functions can be used as basis functions much like the Fourier basis functions. A function can be approximated by a unique polynomial of degree N by the coefficients c_k in

$$f(x) = \sum_{k=0}^{N} c_k \phi_k(x). \tag{2.67}$$

However, the same function can be uniquely represented by its value at $N+1$ collocation points rather than the coefficients resulting from the projection onto the basis functions. The Chebyshev collocation points are defined over the interval $[-1,1]$ and are given by

$$x_i = \cos(i\pi/N) \quad i = 0, 1, ..., N. \tag{2.68}$$

The spacing of these points gives a resolution of $O(N^{-2})$ near the endpoints and $O(N^{-1})$ near the centre. The derivative at the same points is determined by

a linear combination of the function values which we can write as a matrix-vector product

$$f'(x_i) = \sum_{k=0}^{N} d_{i,k} f(x_k), \quad i = 0, ...N, \tag{2.69}$$

and we define

$$D = \begin{bmatrix} d_{0,0} & \cdots & d_{0,n} \\ \vdots & \ddots & \vdots \\ d_{n,0} & \cdots & d_{n,n} \end{bmatrix}. \tag{2.70}$$

as the Chebyshev differentiation matrix (Mason and Handscomb, 2003). The matrix is a full matrix (unlike for example a tri-diagonal matrix that arises from 2nd order finite differences) and its entries, following (Trefethen, 2000), are

$$d_{00} = \frac{2N^2 + 1}{6}, \tag{2.71}$$

$$d_{NN} = -\frac{2N^2 + 1}{6}, \tag{2.72}$$

$$d_{jj} = \frac{-x_j}{2(1 - x_j^2)} \quad j = 1...N - 1, \tag{2.73}$$

$$d_{ij} = \frac{c_i}{c_j} \frac{(-1)^{i+j}}{(x_i - x_j)} \quad i \neq j \quad i, j = 1...N - 1, \tag{2.74}$$

$$\text{where} \quad c_i = \begin{cases} 2 & \text{for } i = 0 \text{ or } N, \\ 1 & \text{otherwise.} \end{cases} \tag{2.75}$$

For further information regarding Chebyshev methods see Trefethen (2000) or Mason and Handscomb (2003).

2.2.12 Solving the eigenvalue problem

The discretisation points are chosen to be the Chebyshev collocation points as described previously. The Chebyshev polynomials approach is chosen as it maintains high accuracy ("spectral" accuracy). The non constant $N(z)$ is now discretised at the $N + 1$ collocation points and the derivative operators $\frac{\partial}{\partial z}$ are discretised by replacing them with $(N+1) \times (N+1)$ Chebyshev differentiation matrices produced by the DMSUITE package (Weideman and Reddy, 2000). The eigenvalue problem is then rewritten as

$$D^2 \phi_n + \kappa_n^2 Q^2(z) \phi_n = A\phi_n + (k_x^2 + k_y^2)B\phi_n = 0, \tag{2.76}$$

where

$$A = D^2, \tag{2.77}$$
$$B = Q^2(z). \tag{2.78}$$

However before proceeding we enforce the Dirichlet boundary conditions by removing the first and last row and column from the matrices A and B. The problem has now been reduced to a generalised matrix eigenvalue problem, and we use MATLAB's `eig` function to solve it. The Dirichlet endpoints are then appended to the resulting eigenfunctions yielding the desired ϕ_n solutions.

The Chebyshev differentiation matrix is also used to compute ϕ_n' which is needed for the decomposition of the horizontal flow fields. Finally the resulting eigenfunctions are interpolated from the Chebyshev points onto model grid points as needed by the Chebyshev interpolation function included in the `DMSUITE` package. The MATLAB code used to solve this problem is shown in Appendix A.1.

2.2.13   Vertical mode projection

The goal is to express the velocity and density fields as a sum of contributions from each vertical mode. This will be useful later when analysing model results to identify the presence of each internal wave mode.

We make the assumption that all waves present are of the same (tidal) frequency. If we separate the horizontal and vertical dependence as follows

$$u = U(x,y)\phi_n'(z)e^{-i\omega t}, \tag{2.79}$$
$$v = V(x,y)\phi_n'(z)e^{-i\omega t}, \tag{2.80}$$
$$w = W(x,y)\phi_n(z)e^{-i\omega t}, \tag{2.81}$$
$$\rho' = R(x,y)\phi_n(z)e^{-i\omega t}, \tag{2.82}$$

then we can express the field at each (x,y) as a sum over vertical mode contributions

$$u = \frac{1}{\kappa_n}\sum_1^\infty u_n\phi_n'(z), \tag{2.83}$$

$$v = \frac{1}{\kappa_n}\sum_1^\infty v_n\phi_n'(z), \tag{2.84}$$

$$w = \sum_1^\infty w_n\phi_n(z), \tag{2.85}$$

$$\rho' = \sum_1^\infty r_n N^2(z)\phi_n(z). \tag{2.86}$$

19

To find the u_n, v_n, w_n, and r_n we project by taking inner products

$$u_n = \frac{1}{\kappa_n} \int_{-H}^{\eta} u \phi_n'(z) \, dz, \tag{2.87}$$

$$v_n = \frac{1}{\kappa_n} \int_{-H}^{\eta} v \phi_n'(z) \, dz, \tag{2.88}$$

$$w_n = \int_{-H}^{\eta} w Q^2(z) \phi_n(z) \, dz, \tag{2.89}$$

$$r_n = \int_{-H}^{\eta} \rho' N^2(z) Q^2(z) \phi_n(z) \, dz. \tag{2.90}$$

In discrete coordinates (such as when analysing numerical model results) the integrals become sums over model levels. The horizontal kinetic energy in each vertical mode for the horizontal flow fields is computed as a vertical integral

$$E_{uv} = \int_{-H}^{\eta} \frac{1}{2}(u^2 + v^2) \, dz = \frac{1}{2} \int_{-H}^{\eta} \left(\sum_{1}^{N} u_n \phi_n'(z) \right)^2 + \left(\sum_{1}^{N} v_n \phi_n'(z) \right)^2 \, dz. \tag{2.91}$$

Due to the orthogonality condition between ϕ_n' and ϕ_m' we immediately notice all of the cross terms are zero and the horizontal kinetic energy is simply

$$E_{uv} = \int_{-H}^{\eta} \frac{1}{2}(u^2 + v^2) \, dz = \frac{1}{2} \sum_{1}^{N} u_n^2 + \frac{1}{2} \sum_{1}^{N} v_n^2. \tag{2.92}$$

This expression states that the vertically integrated energy in the horizontal velocity fields is equal to the sum of the vertically integrated energy in each mode.

The vertically integrated energy in the vertical velocity is a bit more complex due to the weighting function in the orthogonality condition. For the vertical velocity,

$$E_w = \int_{-H}^{\eta} \frac{1}{2} w^2 \, dz = \frac{1}{2} \int_{-H}^{\eta} \left(\sum_{1}^{N} w_n \phi_n(z) \right)^2 \, dz, \tag{2.93}$$

and for the available potential energy,

$$E_\rho = \int_{-H}^{\eta} \frac{1}{2} \frac{g^2 \rho'^2}{\rho_0 N^2(z)} \, dz = \frac{1}{2} \int_{-H}^{\eta} \left(\sum_{1}^{N} \frac{g^2 r_n^2}{\rho_0} \phi_n(z) \right)^2 \, dz. \tag{2.94}$$

In general the cross terms in the expressions for E_w and E_ρ are nonzero when integrated vertically and thus cannot be written as a sum of contributions from each mode. However, in the case of constant N they are zero and the energy can be expressed in terms of the projection coefficients w_n and r_n.

20

2.3 Mesoscale eddies

Eddies are one of the predominant mesoscale phenomena observed in the world's oceans. Mesoscale features are defined to have length scales on the order of the first baroclinic Rossby radius of deformation, $R_d = NH/f$ away from the equator, or $R_d = \sqrt{NH/\beta}$ near the equator (McWilliams, 2008). Here N is the buoyancy (Brunt-Väisälä) frequency of the main pycnocline, H is the water depth, f is the local Coriolis parameter, and β is the gradient of the Coriolis parameter. At the highest latitudes this deformation radius is order 10 km, and at mid-latitudes order 100 km. Observations analysed by (Krauss et al., 1990) and by (Eden, 2007) indicate that the length scale of ocean eddies does indeed vary roughly with the baroclinic Rossby radius of deformation, although they did not find a strong linear relationship.

Eddies are the ocean equivalent of atmospheric storm systems in that they have approximately circular rotation and are believed to have common generation mechanisms. One main difference, however, is the time scale; atmospheric storm systems evolve on time scales of hours to days while ocean eddies evolve on the order of weeks to months, and in some cases years.

The dynamics of ocean eddies are described by the quasi-geostrophic model. Quasigeostrophic motions are governed by

$$\frac{\partial q}{\partial t} + J(\psi, q) = 0, \tag{2.95}$$

$$q = \nabla^2 \psi + \frac{\partial}{\partial z}\left(\frac{f_0^2}{N^2(z)}\frac{\partial \psi}{\partial z}\right), \tag{2.96}$$

where q is the potential vorticity and ψ is the streamfunction. Once the streamfunction is determined the velocities and density and pressure perturbations are

recovered from

$$u = u_g + u_{ag}, \tag{2.97}$$

$$v = v_g + v_{ag}, \tag{2.98}$$

$$u_g = -\frac{\partial \psi}{\partial y}, \tag{2.99}$$

$$v_g = +\frac{\partial \psi}{\partial x}, \tag{2.100}$$

$$u_{ag} = -\frac{1}{\rho_0 f}\frac{\partial p'}{\partial y} - \frac{1}{\rho_0 f^2}\frac{\partial^2 p'}{\partial t \partial x} - \frac{1}{\rho_0{}^2 f^3}J\left(p', \frac{\partial p'}{\partial x}\right), \tag{2.101}$$

$$v_{ag} = +\frac{1}{\rho_0 f0}\frac{\partial p'}{\partial x} - \frac{1}{\rho_0 f^2}\frac{\partial^2 p'}{\partial t \partial y} - \frac{1}{\rho_0{}^2 f^3}J\left(p', \frac{\partial p'}{\partial y}\right), \tag{2.102}$$

$$w = -\frac{f}{N^2}\left[\frac{\partial^2 \psi}{\partial t \partial z} + J\left(\psi, \frac{\partial \psi}{\partial z}\right)\right] \tag{2.103}$$

$$\rho' = -\frac{\rho_0 f}{g}\frac{\partial \psi}{\partial z}, \tag{2.104}$$

$$p' = \rho_0 f \psi, \tag{2.105}$$

where $J(a, b) = \left(\frac{\partial a}{\partial x}\frac{\partial b}{\partial y} - \frac{\partial a}{\partial y}\frac{\partial b}{\partial x}\right)$ is the Jacobian operator and the "g" and "ag" subscripts indicate the geostrophic and ageostrophic, respectively.

The solutions for u and v are broken into geostrophic and ageostrophic parts to emphasise that quasigeostrophy is a correction to geostrophy. The ageostrophic parts are small compared to the geostrophic terms. However, the small terms are needed to explain the evolution of quasigeostrophic features from their static geostrophic counterparts.

Vertically trapped solutions

As in the internal wave case we consider a flat bottomed ocean with a rigid lid. The boundary conditions are the same, $w(0) = w(-H) = 0$, and we need to convert them to conditions on ψ. Using the linearised form of (2.103) gives us

$$\frac{\partial \psi}{\partial z}(z) = 0 \qquad z = 0, -H. \tag{2.106}$$

We linearise (2.95) and substitute (2.96) for q to obtain

$$\frac{\partial q}{\partial t} = \frac{\partial}{\partial t}\left(\nabla^2 \psi + \frac{\partial}{\partial z}\left(\frac{f^2}{N^2(z)}\frac{\partial \psi}{\partial z}\right)\right) = 0. \tag{2.107}$$

We seek vertically trapped solutions of the form

$$\psi = \hat{\psi}(z)e^{i(kx+ly-\omega t)}, \tag{2.108}$$

22

and substitute into (2.107). This yields an eigenvalue problem describing the vertical structure of quasigeostrophic motions

$$\frac{\mathrm{d}}{\mathrm{d}z}\frac{f^2}{N^2(z)}\frac{\mathrm{d}\hat{\psi}_n}{\mathrm{d}z} = -(k^2 + l^2)\hat{\psi}_n \equiv -\lambda_n^2\hat{\psi}_n \tag{2.109}$$

subject to the boundary conditions

$$\frac{\mathrm{d}\hat{\psi}_n}{\mathrm{d}z}(z) = 0 \quad z = 0, -H. \tag{2.110}$$

To derive the orthogonality condition we define $A(z) = \frac{f^2}{N^2(z)}$, multiply (2.109) by ψ_m and integrate over z,

$$-\lambda_n^2\int_{-H}^0 \hat{\psi}_n\hat{\psi}_m\,dz = \int_{-H}^0 \hat{\psi}_m(A\hat{\psi}_n')'\,dz. \tag{2.111}$$

Integrating by parts produces

$$-\lambda_n^2\int_{-H}^0 \hat{\psi}_n\hat{\psi}_m\,dz = \hat{\psi}_m A\hat{\psi}_n'\Big|_{-H}^0 - \int_{-H}^0 A\hat{\psi}_m'\hat{\psi}_n'\,dz. \tag{2.112}$$

The first term on the right is zero via the boundary conditions. Integrating by parts again produces

$$-\lambda_n^2\int_{-H}^0 \hat{\psi}_n\hat{\psi}_m\,dz = -\hat{\psi}_m' A\hat{\psi}_n\Big|_{-H}^0 + \int_{-H}^0 \hat{\psi}_n(A\hat{\psi}_m')'\,dz. \tag{2.113}$$

Again by the boundary conditions the first term on the right is zero. We now switch n and m in (2.111) and substitute, yielding

$$-\lambda_n^2\int_{-H}^0 \hat{\psi}_n\hat{\psi}_m\,dz = -\lambda_m^2\int_{-H}^0 \hat{\psi}_n\hat{\psi}_m\,dz, \tag{2.114}$$

which reduces to

$$(\lambda_m^2 - \lambda_n^2)\int_{-H}^0 \hat{\psi}_n\hat{\psi}_m\,dz = 0. \tag{2.115}$$

For the $n \neq m$ case the integral is zero. For the case of $n = m$ we rescale the eigenfunction such that the integral is unity. Thus the orthogonality condition is

$$\int_{-H}^0 \hat{\psi}_n\hat{\psi}_m\,dz = \delta_{nm}. \tag{2.116}$$

There are an infinite number of solutions (modes), where the eigenvalue λ_n is the inverse of the radius of deformation (Carton, 2001). Mode 0 is the barotropic mode,

and the higher modes are baroclinic modes. Observations show that the vertical structure of oceanic eddies is dominated by the first baroclinic mode (Krauss et al., 1990). This means that the first vertical mode explains most of the deflection of isopycnal surfaces from equilibrium.

The solutions for u and v are dominated by the pressure gradient (geostrophic) terms and hence mesoscale eddies are often referred to as geostrophic eddies. The pressure gradient has two primary contributors; the gradient of the sea-surface elevation, and the gradient of isopycnal surfaces. At the surface, the horizontal gradient of the sea-surface balances the velocity and the density surfaces do not contribute. In other words, without a sea-surface gradient there can be no geostrophic flow at the surface. However, as one moves downward in the water column, horizontal gradients in density contribute to the horizontal pressure gradient, either increasing or decreasing the magnitude of the flow depending on the sign.

The eigenvalue problem (2.109) is easily solved for the constant N case; by inspection we find solutions of the form $\hat{\psi}_n = \cos(n\pi z/H), n = 0, 1, 2, ...,$ however the non constant $N(z)$ case requires a numerical method to find $\hat{\psi}(z)$. The method used closely follows (Talbot and Crampton, 2005) but is modified to include the Neumann conditions at both the top the bottom.

2.3.1 Solving the eigenvalue problem

The non constant $N^2(z)$ is now discretised at the $N + 1$ Chebyshev collocation points and the derivative operators $\frac{\partial}{\partial z}$ are discretised by replacing them with $(N + 1) \times (N + 1)$ Chebyshev differentiation matrices. The eigenvalue problem is then rewritten as

$$D\frac{f^2}{N^2(z)}Dp \equiv Mp = -\lambda p. \tag{2.117}$$

Next we remove the top and bottom entries of M such that

$$M = \begin{bmatrix} . & \cdots & . \\ E_0 & E & E_N \\ . & \cdots & . \end{bmatrix}, \tag{2.118}$$

and we can rewrite (2.117) as

$$Ep = -\lambda p - E_0 p_n(x_0) - E_N p_n(x_n). \tag{2.119}$$

Here, $p_n(x_0)$ and $p_n(x_n)$ are unknowns. By writing the boundary conditions in the form

$$\sum_{k=0}^{n} d_{0,k} p_n(x_k) = d_{0,0} p_n(x_0) + \sum_{i=1}^{n-1} d_{0,i} p_n(x_i) + d_{0,n} p_n(x_n) = 0, \qquad (2.120)$$

$$\sum_{k=0}^{n} d_{n,k} p_n(x_k) = d_{n,0} p_n(x_0) + \sum_{i=1}^{n-1} d_{n,i} p_n(x_i) + d_{n,n} p_n(x_n) = 0, \qquad (2.121)$$

we get a matrix problem for $p_n(x_0)$ and $p_n(x_n)$:

$$\begin{bmatrix} d_{0,0} & d_{0,n} \\ d_{n,0} & d_{n,n} \end{bmatrix} \begin{bmatrix} p_n(x_0) \\ p_n(x_n) \end{bmatrix} = - \begin{bmatrix} d_{0,1} & d_{0,2} & \cdots & d_{0,n-1} \\ d_{n,1} & d_{n,2} & \cdots & d_{n,n-1} \end{bmatrix} \begin{bmatrix} p_n(x_1) \\ p_n(x_2) \\ \vdots \\ p_n(x_{n-1}) \end{bmatrix}. \qquad (2.122)$$

Labelling the matrices in (2.122) as B_0 and B_1, and substituting into (2.119) yields

$$(E - [E_0 \ E_N] B_0^{-1} B_1) p = -\lambda p. \qquad (2.123)$$

The problem has now been reduced to a matrix eigenvalue problem, and we use MATLAB's `eig` function to solve it. The MATLAB code used to solve this problem is shown in Appendix A.2.

2.3.2 Observations

In the case of an eddy we can assume that it is perfectly circular and work in polar coordinates such that horizontal pressure gradient is radial, and the velocities (u, v) are replaced by the azimuthal velocity. The azimuthal velocities may switch sign with depth depending on how the density surfaces are deflected in the vertical. However, as mentioned above, the first mode is most commonly observed. For example, a hydrographic section of density across the Agulhas current system (Gladyshev et al., 2008) is shown in Figure 2.5. The authors have labelled three regions as E1, E2 and E3 to indicate eddies. Note that in each case the isopycnals are deflected; in E1 and E2 downward and in E3 first upward and then downward. The stronger the deflection the stronger the contribution to the radial pressure gradient and hence the azimuthal velocity. E1 and E2 appear to be mode 1 and E3 mode 2. A barotropic eddy would not be visible in the density field as the velocity is vertically uniform and driven by the pressure gradient at the surface.

Some of the most eddy-rich regions of the ocean are found in the vicinity of western boundary currents. One famous region is the Gulf Stream (North Atlantic Current) system found off the east coast of North America. Meanders that occur in
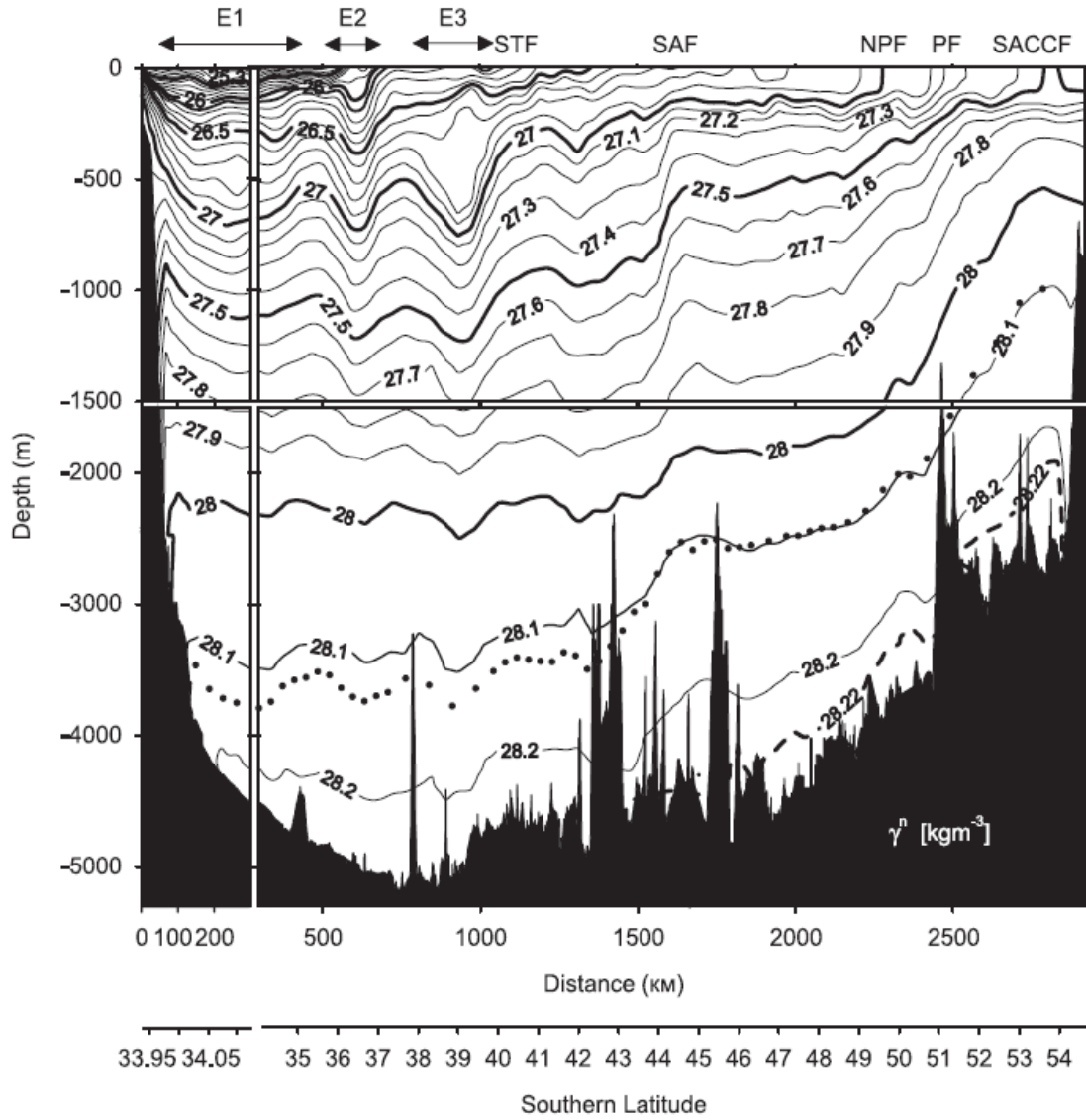
Figure 2.5: Hydrographic data section across the Agulhas current system collected in November, 2004. Three eddies labelled E1, E2 and E3 are indicated on the plot. Note the deflections of the isopycnal surfaces associated with each. Figure reproduced from Gladyshev et al. (2008)
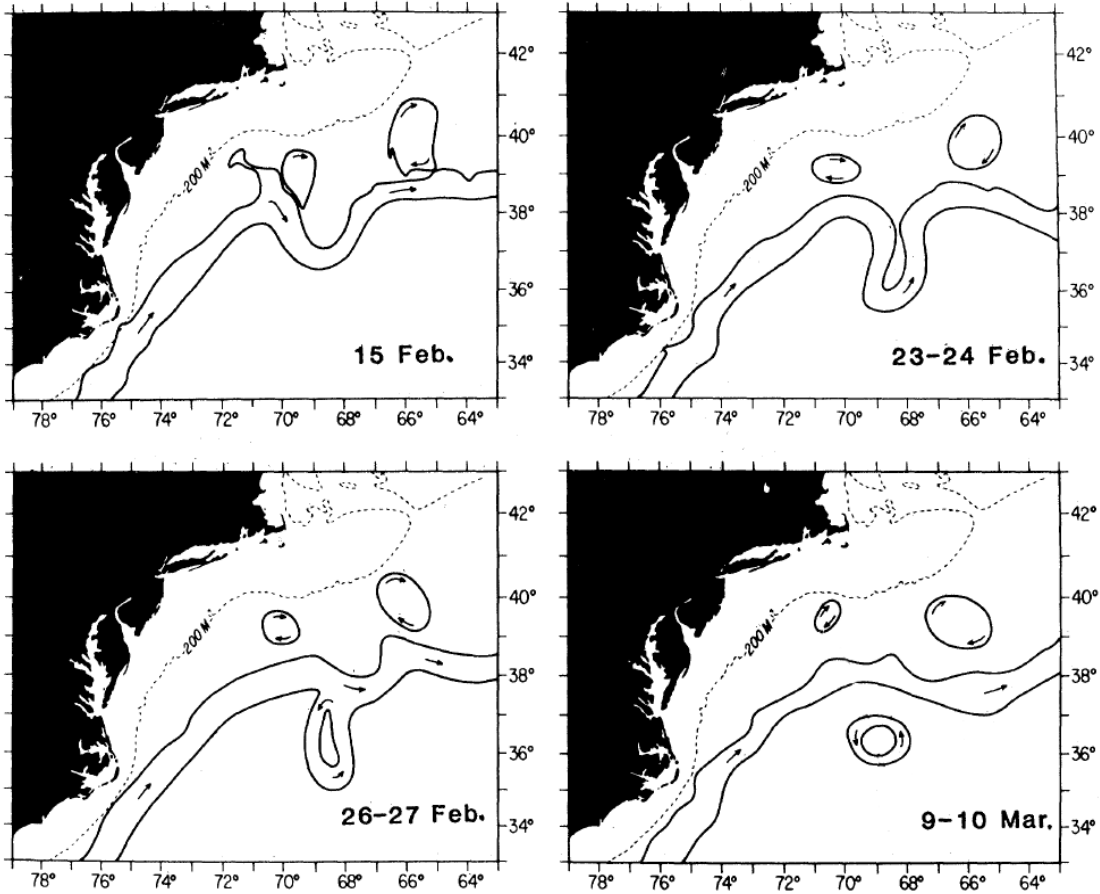
Figure 2.6: Time evolution of the Gulf Stream during the production of a cold core eddy observed during February-March of 1977. Figure adapted from The Ring Group (1981).

the jet as it leaves the coast results in the formation of numerous mesoscale eddies often called Gulf Stream rings. Gulf stream rings have been studied extensively over the last several decades. One of the main features of such rings is that they are produced in two varieties: warm core and cold core. The warm core rings are produced when current loops detach on the north side of the current, encasing Sargasso Sea water in their core. A similar mechanism is responsible for the cold core eddies on the south side of the current. Figure 2.6 shows the time evolution of the jet during the production of a cold core eddy.

A hydrographic section of temperature across the Gulf Stream, shown in Figure 2.7. The isotherms (roughly isopycnals) are deflected upwards, indicating cyclonic rotation. This eddy is a cold-core ring as its core is colder than the surrounding water and it is found to the south of the Gulf Stream.

The Gulf Stream is also responsible for producing eddies in the Gulf of Mexico. One to two are produced each year by meanders in the stream as it loops through
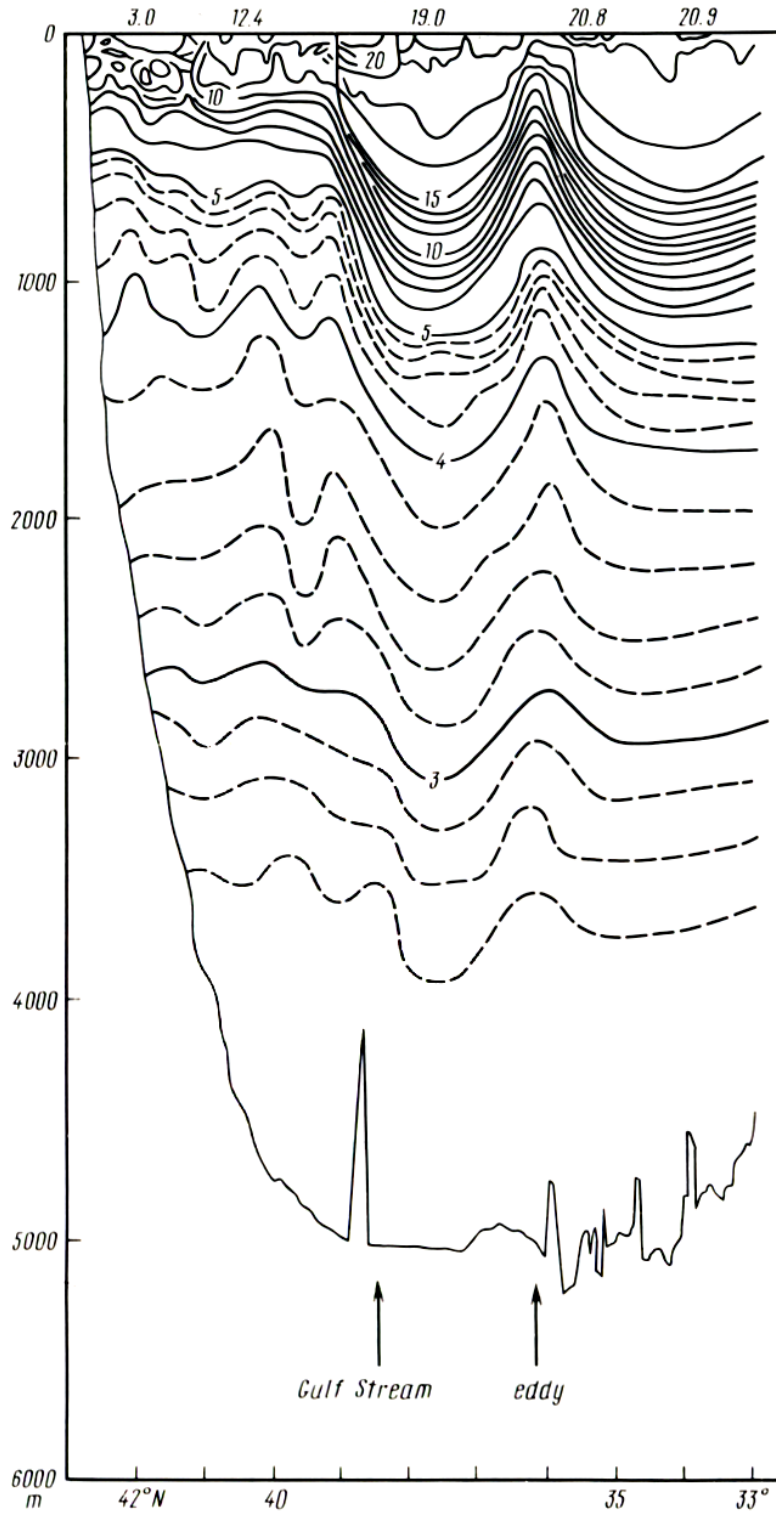
Figure 2.7: Hydrographic data section across the Gulf Stream from April 1960. The isotherms are deflected upwards strongly, indicating cyclonic rotation. Figure reproduced from Kamenkovich et al. (1986).

the southeast corner of the Gulf. These loop current eddies then propagate slowly west and break on the coast of Mexico or Texas.

Other Western boundary currents that produce eddies include the Kuroshio system off the coast of Japan and the Brazil current on the east coast of South America. Also the Agulhas Current, which exists south of Africa is also responsible for producing eddies.

Eddies have also been discovered beneath the ice in Canada Basin (Timmermans et al., 2008). Tethered profilers have recorded measurements indicative of eddies with a radius of approximately 10 km radius. This is somewhat smaller than the typical 50-200 km observed in the ice-free ocean and is consistent with other observations of decreasing radius with increasing latitude.

2.3.3 Meddies

Meddies are unique subsurface eddies found in the East North Atlantic ocean. The origin of such eddies is attributed to the Mediterranean Sea hence the name meddies (Mediterranean eddies). Warm salty Mediterranean Sea water overflows from the Straight of Gibraltar and flows down the continental slope to a depth of 500-1500 m. At this depth the influence of local currents causes this water to detach from the slope in the form of 40-100 km diameter lenses. The lenses propagate Westward into the Atlantic while rotating anticyclonically (clockwise) at velocities up to 30 cm s $^{-1}$. Due to the large deviation in temperature (up to 4ºC) and salinity (up to 1 psu), meddies are easily identified in hydrographic sections in the North East Atlantic. It is estimated that 17 meddies are generated each year and have mean lifespans of 1.7 years and that approximately 30 meddies exist at any given time. One of the primary fates for meddies is collision with seamount. For more details on meddies see Richardson (2000).

2.3.4 Sea surface signature

A drop in sea-surface height is associated with the cold core eddies and an increase with the warm cores. Maps of sea-surface variability can be used to identify eddy-rich regions because eddies almost always have a sea-surface height signature. Geostrophic eddies can only have nonzero surface currents if they have a sea-surface height gradient. Such a map of sea-surface variability is shown in Figure 2.8. Regions of high sea surface variation correspond to known locations of high eddy activity, particularly in the vicinity of the Gulf Stream, the Kuroshio Current, the Brazil current and the Algulhas current.

Further, one can identify regions dominated by cold-core and by warm-core type eddies by looking at the skewness of the sea-surface variability. The variability is skewed negative if there are primarily cold core eddies (sea surface is depressed), and positive for warm core eddies (sea surface is elevated). A map of the skewness
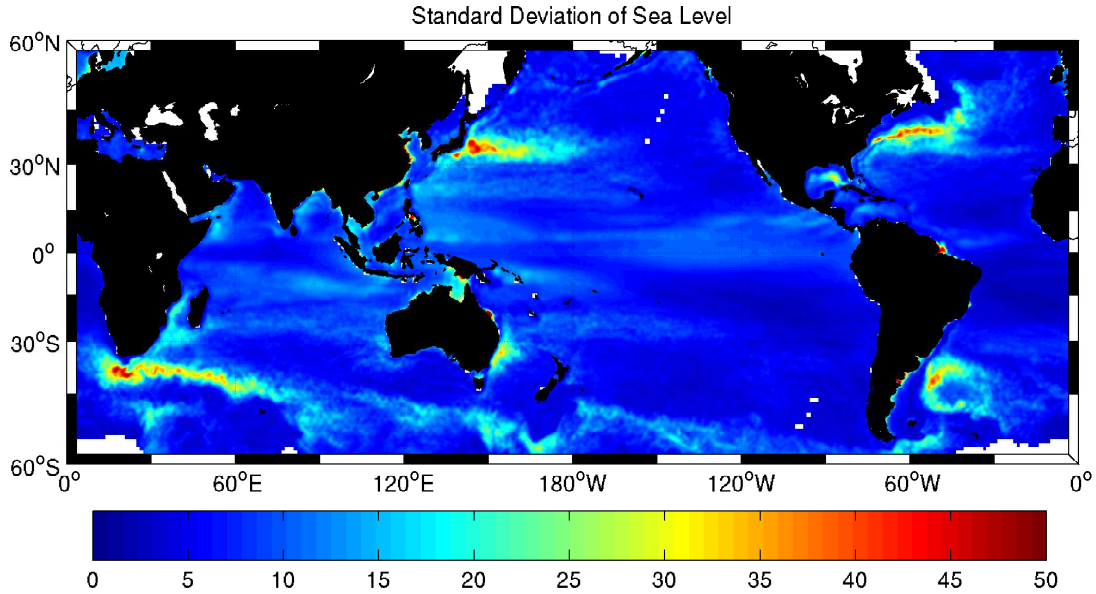
Figure 2.8: Standard deviation of sea-surface height of the world's ocean computed from ten years of altimeter data. Regions of high sea surface activity correspond to locations of increased eddy activity. Figure reproduced from Thompson and Demirov (2006).

is shown in Figure 2.9. The statistic is most meaningful in regions of high eddy activity and is not very useful otherwise. For example, the large red patch just west of South America is not indicative of the world's largest warm core eddy field because the eddy activity there is low.

Detecting eddies by altimeter is limited to eddies with a sea-surface signature and hence subsurface eddies such as meddies and eddies existing below ice cover will not be observed.

2.3.5 Generation mechanisms

Eddies are believed to be generated by means of baroclinic instability. Such an instability exists when a steady state system exists in unstable equilibrium. A small perturbation to such an unstable equilibrium will move the system from its steady state and exponential growth results until other considerations prevent it from continuing. A classic example of baroclinic instability was formulated by Eady (1949). The problem consists of zonal flow on an f-plane in geostrophic balance with a meridional density gradient. A rigid lid is also prescribed for simplicity. Eady showed that perturbations to this system are unstable below a critical wavelength. Since perturbations are ubiquitous in nature they will inevitably occur and such perturbations grow exponentially via nonlinear effects until they are limited by other physical means. Boundary currents resemble this problem. Perturbations to

30
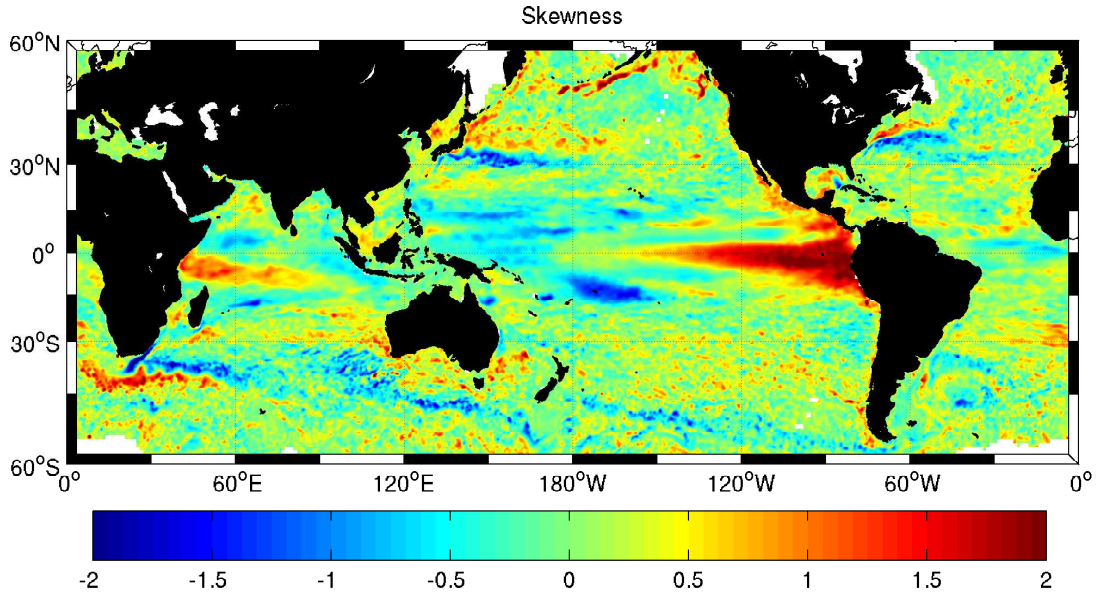
Figure 2.9: Skewness of sea-surface height of the world's ocean computed from ten years of altimeter data. Red (blue) regions correspond to a preference for warm (cold) core eddies. Figure reproduced from Thompson and Demirov (2006).

such currents grow into meanders which eventually lead to the shedding of eddies. Figure 2.6 shows an example of such a meander producing a Gulf Stream ring.

2.4 MITgcm

The model used in this thesis to carry out numerical simulations is the MITgcm, the general circulation model developed at MIT. The model is very flexible as it can be used for both atmospheric and ocean modelling, can scale from running on a single PC to running on hundreds of processors on a large scale computing cluster, and has a wide variety of packages available to use in experimental setups. This section will describe some features of the model and summarise the equations that it solves prognostically.

2.4.1 Computational features

The MITgcm is written in FORTRAN-77, a language widely used in the field of computational fluid dynamics. It can be compiled and operated on a wide variety of platforms, although it is typically operated on UNIX/LINUX based systems. Running as a single thread (one processor) it can run on a PC for small to medium size simulations. Running with numerous threads (spanning multiple processors and/or nodes such as in a cluster) the model can scale to very large simulations.

Parallelism is achieved via horizontal domain decomposition. Since the model does not need global access to the domain (as for example a Fourier based spectral model would), each thread can operate on its fraction of the global domain. Each subdomain has a copy of its neighbour's boundary cells (called ghost cells) such that the spatial operators can work locally and are updated by boundary exchanges after each time step. The MITgcm scales well until the ghost cell exchanges become significant with respect to the rest of the computation.

2.4.2   Numerical features

The MITgcm uses an Arakawa C-grid for placement of the model's physical arrays. The tracers (here, temperature and salinity) are located at the centre of each grid cell. The velocity vector $\vec{u} = (u, v, w)$ is split into its components, u specified on the east/west side of each cell, v on the north/south, and w at the top/bottom. The sea surface height η is located at top and centre of the top cell in each column of cells.

Other noteworthy features are

1. The horizontal grid may use spherical coordinates or Cartesian coordinates with both f- and β- plane options available.

2. The vertical grid uses fixed z-levels.

3. Time stepping is either leap-frog or Adams-Bashforth 3.

4. The surface may be rigid-lid, linear free surface, or nonlinear free surface.

5. Partial cells are available for improved representation of bottom topography (also called lopped-cells).

6. Non-hydrostatic formulation is available as well as hydrostatic.

2.4.3   Equations solved

The MITgcm solves the non-hydrostatic incompressible Boussinesq equations,

$$\frac{D\vec{u}_h}{Dt} + f\hat{k} \times \vec{u}_h + \frac{1}{\rho_c}\nabla_h p' \;=\; \vec{F}_h, \tag{2.124}$$

$$\epsilon_{nh}\frac{Dw}{Dt} + \frac{g\rho'}{\rho_c} + \frac{1}{\rho_c}\frac{\partial p'}{\partial z} \;=\; \epsilon_{nh}F_v, \tag{2.125}$$

$$\vec{\nabla}_h \cdot \vec{u}_h + \frac{\partial w}{\partial z} \;=\; 0, \tag{2.126}$$

$$\rho' \;=\; \rho(\theta, S, p_0(z)) - p_c, \tag{2.127}$$

$$\frac{D\theta}{Dt} \;=\; Q_\theta, \tag{2.128}$$

$$\frac{DS}{Dt} \;=\; Q_S, \tag{2.129}$$

where $\vec{u}_h$ is the horizontal velocity vector, f is the Coriolis parameter, $\hat{k}$ is the vertical unit vector, ρ_c is a constant reference density, ∇_h is the horizontal gradient operator, p' is the pressure perturbation, $\vec{F}_h$ is the horizontal momentum forcing, ϵ_{nh} is a non hydrostatic parameter, w is the vertical velocity, g is the gravitational acceleration constant, ρ' is the density perturbation, $\rho_0(z)$ is a reference density profile, θ is the temperature, Q_θ is the temperature forcing, S is the salinity, and Q_S is the salinity forcing.

When operating in non-hydrostatic mode ϵ_{nh} is set to one. However, when the model is switched to hydrostatic mode ϵ_{nh} is set to zero and the equations become the hydrostatic incompressible Boussinesq equations. These hydrostatic equations are often referred to as the hydrostatic primitive equations (HPE) within the ocean modelling community.

Chapter 3

Methods

This chapter describes the setup of the numerical model MITgcm and three configurations that are used to investigate eddy-internal wave interactions. Background stratification profiles are defined and modifications are made to the MITgcm to facilitate the experiments. Following this are three configurations, one for internal waves, one for an eddy, and one including both phenomena.

3.1 Stratification

Two functions are designed for use as the reference density profile, a linear density profile ($\bar{\rho}_1$) and a profile containing a pycnocline ($\bar{\rho}_2$):

$$\bar{\rho}_1(z) \quad = \quad \rho_0(1 - N_0^2 z/g), \tag{3.1}$$
$$\bar{\rho}_2(z) \quad = \quad \rho_0(1 - N_0^2 z/g) + 0.5\Delta\rho(1 - \tanh(A(z+B)/H)), \tag{3.2}$$

where $N_0 = 1.0 \times 10^{-3}$ s^{-1}, $\rho_0 = 1028$ kg m^{-3}, $\Delta\rho = 1$ kg m^{-3}, $A = 50$ m, $B = 400$ m and $H = 5000$ m.

Figure 3.1 shows a plot of each of these functions as well as their associated buoyancy frequency frequency $N(z)$. The first three internal wave modes and their derivatives are shown for $\bar{\rho}_1$ in Figure 3.2 and for $\bar{\rho}_2$ in Figure 3.3. The first quasigeostrophic mode and its derivative are shown in Figure 3.4 for both $\bar{\rho}_1$ and $\bar{\rho}_2$.

3.2 Modifications to the MITgcm model

Energy flux computation

Calculations to find the energy flux due to baroclinic disturbances are added to the MITgcm model. Included with MITgcm is a prototype package called `mypackage`
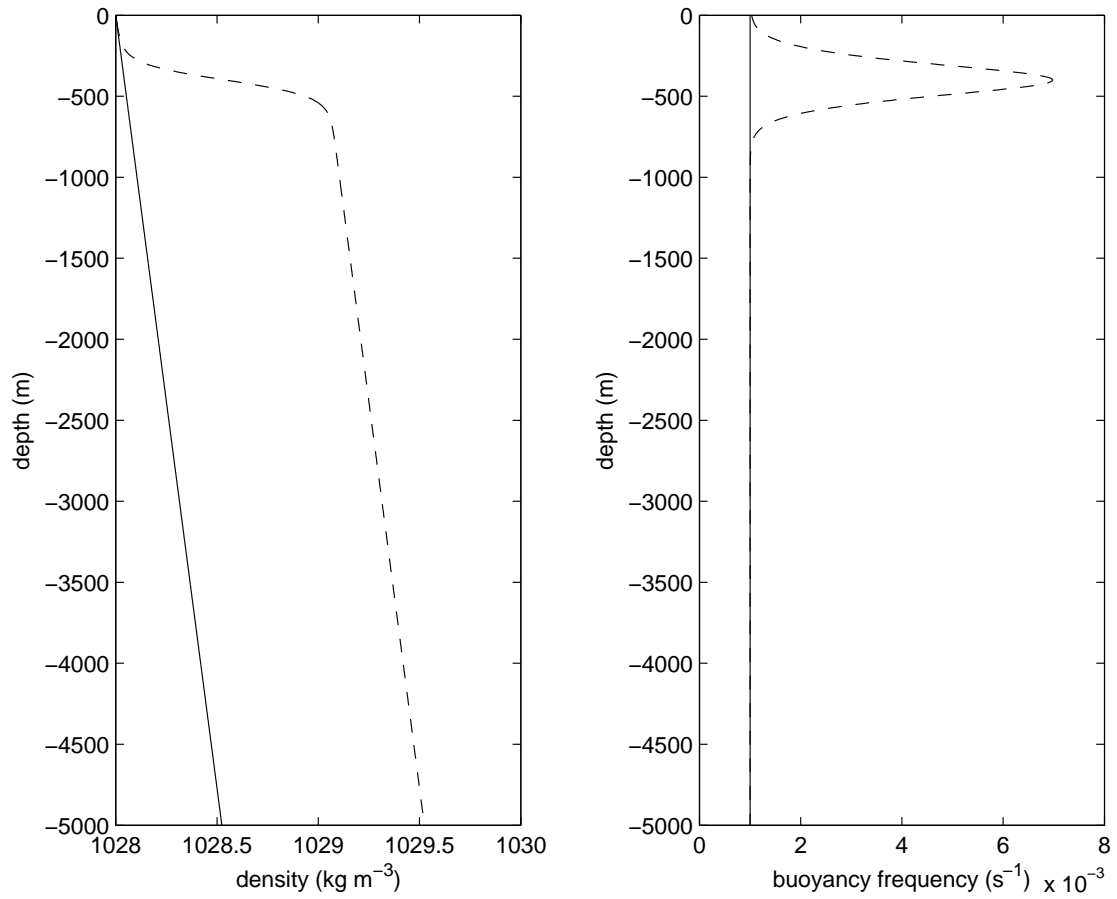
Figure 3.1: The reference density profiles used in this thesis. The solid lines show $\bar{\rho}_1(z)$ and $N_1(z)$, and the dashed lines show $\bar{\rho}_2(z)$ and $N_2(z)$. The left panel shows density and the right panel buoyancy frequency.
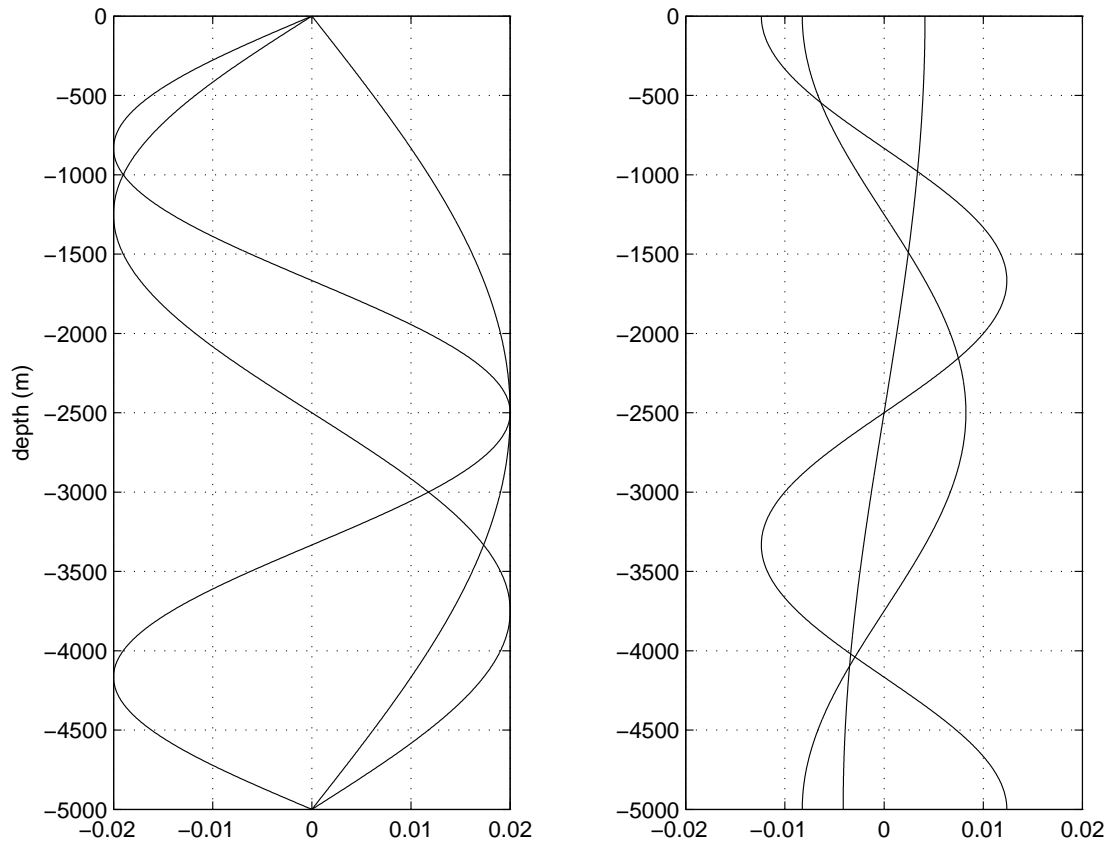
Figure 3.2: The first three internal wave modes (left) and their derivatives (right) for the linear density case ($\bar{\rho}_1$). The modes are sinusoidal as expected.
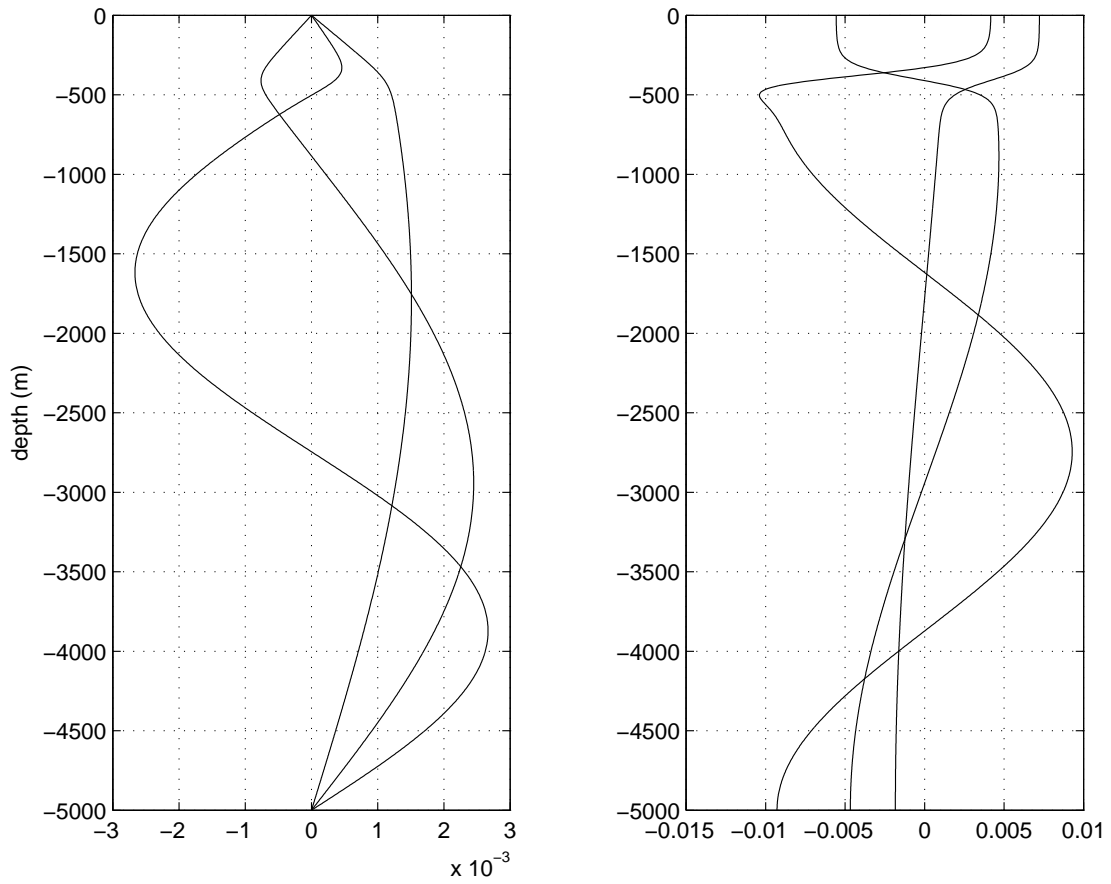
Figure 3.3: The first three internal wave modes (left) and their derivatives (right) for the nonlinear density case ($\bar{\rho}_2$). The curves deviate substantially near the pycnocline from their otherwise sinusoidal shape.
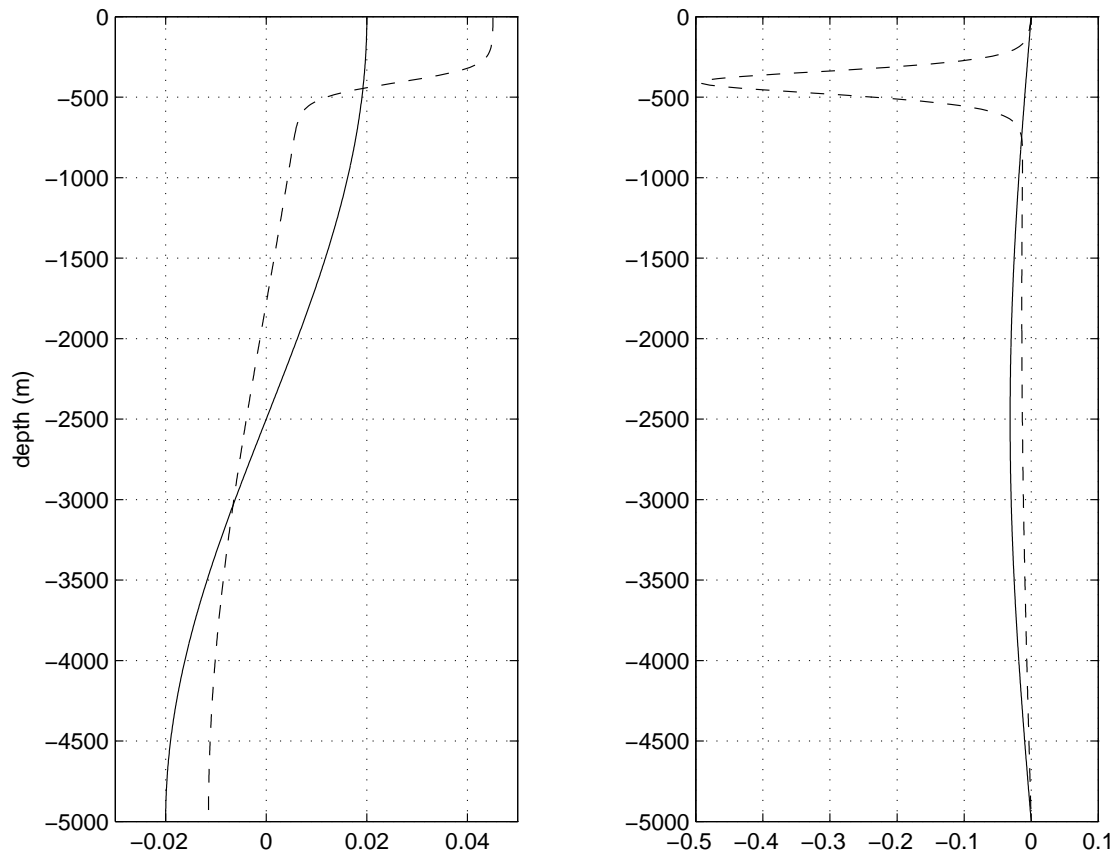
Figure 3.4: Mode 1 eigenfunctions obtained by solving the eigenvalue problem for the vertical structure of quasigeostrophic eddies. The left curves are the mode 1 functions and the right curves are the derivatives. Solid indicates the linear density profile ($\bar{\rho}_1$) and dashed indicates the pycnocline profile ($\bar{\rho}_2$).

for the purpose of adding customisations without needing to modify the rest of the model's source code files. This package is enabled, and the code to compute energy flux was added. The benefit of performing this computation online is that it is much faster than computing it offline from saved snapshot data. Further the time resolution of energy flux calculations can be as high as the time step duration; this would be very costly to achieve offline as fields would need to be saved at each time step. Output of the energy fluxes is done using the `diagnostics` package and allows the user to output averages, snapshots and statistics for both the entire domain and for subdomains.

The baroclinic energy flux is the product of baroclinic velocity u_{bc} and the pressure due to the baroclinic velocity p_{bc}. Following Munroe (2003), we compute these quantities and vertically integrate the energy flux as follows

$$\vec{u}_{bc} \;=\; \vec{u} - \vec{u}_{bt} = \vec{u} - \frac{1}{\eta + H} \int_{-H}^{\eta} \vec{u}\, dz, \tag{3.3}$$

$$p_{bc} \;=\; \int_{z}^{\eta} g\rho'\, dz, \tag{3.4}$$

$$\vec{E}_f \;=\; \vec{u}_{bc} p_{bc}, \tag{3.5}$$

$$\vec{E}_{f,2D} \;=\; \int_{-H}^{\eta} \vec{E}_f\, dz, \tag{3.6}$$

where $\vec{u} = \vec{u}(x,y)$ is the horizontal model velocity, η is the sea-surface elevation, H is the undisturbed water depth, g is the gravitational acceleration constant and ρ' is the density perturbation. The subscripts "bt" and "bc" indicate barotropic and baroclinic, respectively.

Barotropic tide forcing

The `obcs_calc` routine included in the `OBCS` package is modified to prescribe a barotropic tide at the west side of the domain and a radiation condition at the east for the tidally forced model configurations. At the west boundary,

$$u_{west} = -\frac{c}{H}(\eta - \eta_0 \sin(\omega t)), \tag{3.7}$$

where $\omega = 2\pi/44712$ rad s^{-1} is the frequency of the M$_2$ tide, $c = \sqrt{\frac{gHw^2}{w^2 - f^2}}$ is the linear long wave speed, H is the deep water depth, η is the sea-surface elevation and η_0 is computed from the desired barotropic tide magnitude $u_0 = 5.0$ cm s^{-1} via $\eta_0 = u_0 \frac{H}{c}$. At the east boundary,

$$u_{east} = \frac{c}{H}\eta, \tag{3.8}$$

is a radiation condition that allows the barotropic mode exit the domain.

Finally, the reference density profiles described previously are are coded into MITgcm with the modified `mypackage` to facilitate the online energy flux computations. The FORTRAN 77 source code files that implement these computations are included in Appendices C.1, C.2 and C.3.

3.3 Model choices

There are a very large number of options and parameters in the MITgcm model and it is not feasible to do an exhaustive study of all of them. However, for the simplicity of the test problem considered in this thesis, it is possible to narrow down the options to test a much more manageable subset.

Leap-frog vs. Adams-Bashforth-3

Adams-Bashforth-3 (AB3) is a higher order time-marching scheme than leap frog and is expected to produce better results. A time-step convergence test was performed, comparing leap frog and AB3 at a nominal time step and at several reductions down to 1 percent of the nominal time step. Using the smallest time step and AB3 as the reference the AB3 consistently showed smaller errors than leap frog. Thus we choose AB3 for the time stepping scheme in all simulations.

Linear vs. Nonlinear Free Surface

Nonlinear free surface would be the preferred choice by default as it is the most accurate. However, some MITgcm options are unavailable when the nonlinear free surface is selected; for example the Orlanski radiation condition. To determine if the non-linear free surface is important, the 2D internal wave setup (see later section) was simulated with and without the nonlinear free surface. Comparisons of the zonal velocity field after 15 tidal periods showed differences smaller than 0.1 percent of the size of the velocities. Since the free surface displacements are small in these simulations (0.1-1 cm) it is not surprising that the linear approximation holds. Thus the linear free surface is chosen as it opens up more model options.

Momentum viscosity

A Shapiro filter is chosen to take the place of horizontal viscosity. The Shapiro filter is linear and it removes completely the smallest resolvable scales (two grid cell signals). The drawback is that it partly removes larger scales (such as four grid cell signals) but scales larger than this are essentially unaffected. For more on this filter see Shapiro (1970). The end result is that we control the accumulation of energy at small scales by removing it with the Shapiro filter, effectively dissipating

it. The time scale used for the Shapiro filter is one half of a tidal period (22356 s). For vertical viscosity we set the coefficient A_v to zero.

Tracer options

In this thesis we set temperature to a constant value and allow variations in salinity to control the density. Consequently, it is not necessary to time-step the temperature. A modest model speed-up is achieved by setting the option `tempStepping=.FALSE.` in the MITgcm input file `data` which disables time stepping of the temperature field.

Several advection schemes for tracers are available (see the MITgcm manual for details). The centred fourth order scheme is chosen as it is higher order than centred second order, the default. The diffusion coefficients for both temperature and salinity are set to zero.

Grid spacing

The open boundaries in the configurations considered here are somewhat problematic. As designed, the condition on the left prescribes a barotropic tide and the condition on the right permits it to exit the domain. However, baroclinic modes are reflected at each boundary and will propagate back toward the topography. This would complicate analysis as they will interact with the baroclinic modes leaving the topography. A sponge layer was experimented with at the open boundaries to linearly relax to the barotropic mode over several grid cells. The result was good with the exception of the spurious emission of very low amplitude baroclinic waves from the inner edge of the sponging region. Although smaller in magnitude than the internal waves generated by the tide, it was decided to abandon the sponge layer approach.

To avoid the unwanted internal wave-wave interactions we propose a grid-stretching method that moves the boundaries far away from the vicinity of the ridge. We consider relatively short simulations (order 20 tidal periods) and moving the boundaries far enough away avoids the reflection issue.

The horizontal grid spacing is set by a constant plus a difference in shifted hyperbolic tangent functions of the form

$$dx[n] = C + \frac{D}{2}(2 + \tanh(A(x[n]/L - 1/2 - B/2)) - \tanh(A(x[n]/L - 1/2 + B/2))),$$
(3.9)

where C is the inner grid spacing, $C + D$ is the outer grid spacing, L is the domain length, A is a parameter controlling how quickly the spacing transitions from inner to outer resolution, B specifies the fraction of the inner domain to have inner

resolution, and n is the grid cell index ranging from 1 to N, the number of grid points. The grid cell centres are then specified by

$$x[n] = \begin{cases} \frac{1}{2}dx[1] & \text{for } n = 1, \\ x[n-1] + \frac{1}{2}(dx[n-1] + dx[n]) & \text{for } n > 1. \end{cases} \quad (3.10)$$

Typically A and B are fixed with values of 20 and 0.5, respectively. However there is flexibility in choosing the remaining variables C, D, L and N. Choosing C, D and L leads to a requirement on N, however this is not desirable as the resulting N may not be easily divisible for multi-processor domain decomposition. Choosing L and N, and defining D in terms of C is an option as it allows us to control how the outer resolution is related to the inner; however this is also not desirable as the exact value of the inner spacing is not controlled. The most favourable approach is to specify C, L and N, and then determine the required value of D. The value of D is the least important variable to control; it's value does not matter other than it should be a few times larger than C. To proceed one specifies a domain length L, a number of grid points N, and a desired inner resolution C which is less than L/N. D is then iteratively determined as follows

1. Estimate an initial $x[n]$ (ex: equal grid spacing)

2. Estimate an initial D (ex: $(L/N - C)/(1 - B)$)

3. Compute $dx[n]$ by (3.9)

4. Compute $x[n]$ by (3.10)

5. Compute the length of this grid spacing by $L^* = \sum_{n=1}^{N} dx[n]$

6. Compute a new D by $D = D\dfrac{L}{L^*}$

7. Repeat 3-6 until L^* is sufficiently close to L

The ratio C/D gives a rough estimate of the fraction of computational time spent working on the "far fields". Typically we choose N (and thus D) such that 90 percent of the grid points (and thus 90 percent of the computation time) is allocated for the interior domain and the remaining 10 percent for the outer domain. Solving for D typically takes less than a second using MATLAB R2008b on the LINUX system `thelon` and the M-file used is shown in Appendix A.3. Figure 3.5 shows an example grid spacing obtained from this method.
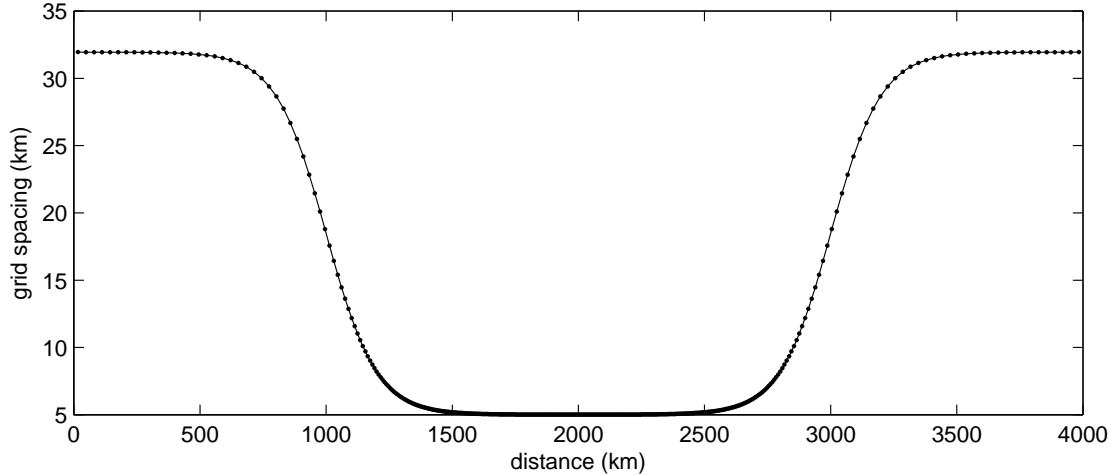
Figure 3.5: A sample grid spacing obtained with N=400, L=4000 km, A=20, B=0.5, C = 5km. Notice that the majority of the points (the dots) are clustered in the high resolution centre of the domain and relatively few are stationed near the edges. The transition between the low and high resolution is smooth to avoid reflection of signals.

3.4 Internal wave configuration

The internal wave configuration is a 2-D model setup designed for the sole purpose of generating internal waves by forcing barotropic tidal flow over topography. Waves generated by this mechanism will be used later to interact with mesoscale eddies. This configuration is used to tune up the model and to verify that the generation of waves and energy flux computations are correct.

Despite the ubiquity of internal waves in the open ocean at a wide variety of wavenumbers and frequencies (see GM79 spectrum) we choose to focus on only the internal tide. The M_2 tide with a period of 12.42 hours is chosen as the tide of interest.

A Gaussian ridge of the form $h(x) = H - h_0 e^{-\frac{x^2}{a^2}}$ is centred in the domain where H is the nominal depth of 5 km, h_0 is the ridge height of 1.5 km, and a is a parameter controlling the width of the ridge. A small enough value of a will produce super critical topography, however, we choose a such that the maximum slope is 75 percent of critical. The east and west boundary conditions are as described in Section 3.2. Finally, energy flux lines are prescribed every 250 km along the domain in the x direction and at each line a time series of energy flux is saved. Table 3.1 lists the rest of the parameters used in this configuration.
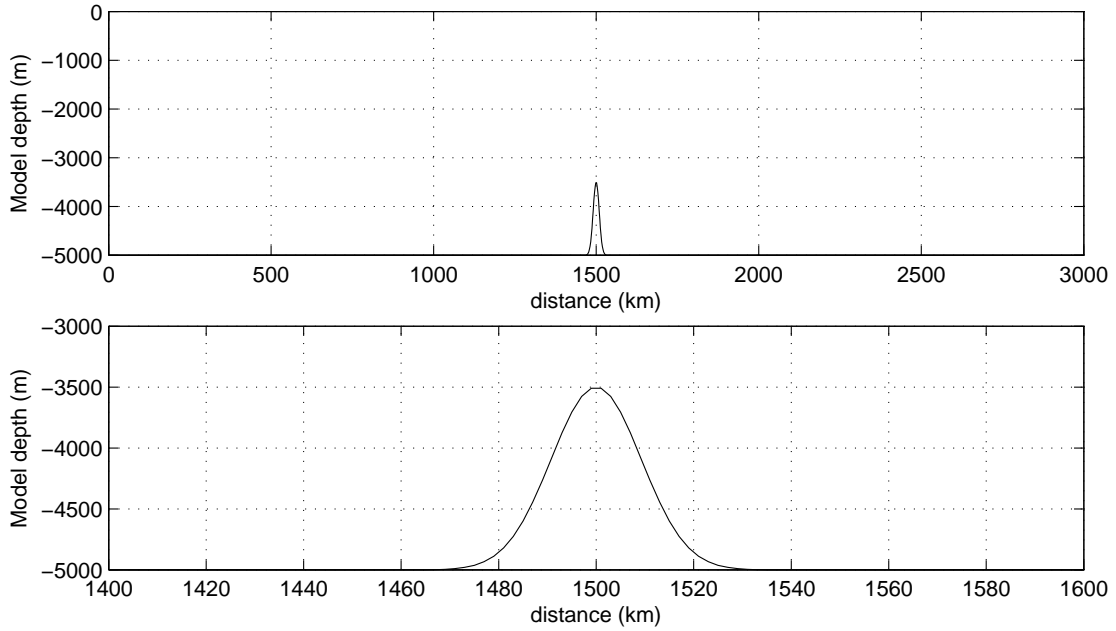
Figure 3.6: The model topography used for generating internal waves (top) and a zoomed in look at just the ridge (bottom).

Table 3.1: Parameters used for the 2D internal wave configuration.

Parameter	Value
Coriolis parameter f	0.5×10^{-4} rad s^{-1}
Reference buoyancy frequency N_0	1.0×10^{-3} rad s^{-1}
Density profile	both (ρ_1 and ρ_2)
Barotropic tide u_0	$5.0\,cm\,s^{-1}$
Domain size	$3000 \times 1000 \times 5$ km
Grid cells	$1500 \times 1 \times 100$
Horizontal grid spacing (fixed)	2 km
Vertical grid spacing (fixed)	50 m
Time step	103.5 s
Duration (tidal periods)	15

3.5 Eddy configuration

Initialising a model with a steady state analytical solution can lead to adjustment. Differences in numerics are one of the reasons that the fields are not balanced in the model. The adjustments are typically small as the model simulates and the adjustments manifest themselves as emitted gravity waves.

We wish to initialise a model with an eddy for the purposes of looking at its interaction with internal waves but spurious gravity wave emissions can complicate the analysis. Hence we design an eddy-only configuration for the sole purpose of adjusting an eddy to be consistent with the model fields. An eddy is designed from quasigeostrophic theory and then adjusted in the MITgcm. The end result is that we have fields consistent with the discretisation in the MITgcm and need not be concerned with any substantial adjustment.

3.5.1 Initialisation of a baroclinic eddy

The eddy is analytically initialised and is prescribed by specifying isopycnal displacements and consistent velocity and sea-surface elevation fields. The density is specified in terms of a reference density profile with shifted isopycnals

$$\rho(x, y, z) = \bar{\rho}(z - \eta(x, y, z)), \tag{3.11}$$

where $\bar{\rho}(z)$ is either (3.1) or (3.2). Asserting that η is small we expand (3.11) in a Taylor series about z and retain only the first two terms to get the the expression

$$\bar{\rho}(x, y, z - \eta) = \bar{\rho}(z) + \frac{N^2(z)\rho_0}{g}\eta(x, y, z) = \bar{\rho} + \rho'. \tag{3.12}$$

Note that for the case of linear density (constant N), this Taylor series is exact because all of the higher derivatives of $\bar{\rho}(z)$ are zero. However, this is not true in general, and the omission of the rest of the terms contributes a small error. Following Carton (2001) we let the vertical structure of the streamfunction be $F_m(z)$, the solution obtained by solving the eigenvalue problem (2.109). Switching to polar coordinates for the horizontal part we write the streamfunction in the form

$$\psi = \psi_h(r)\psi_v(z) = \psi_h(r)F_m(z). \tag{3.13}$$

Noticing that ρ' is related to the streamfunction by (2.104) and to the isopycnal displacement by (3.12) we relate the streamfunction to the isopycnal displacement by

$$\psi_h F'_m(z) = \frac{-N^2(z)}{f}\eta. \tag{3.14}$$

45

We can now choose a function for the horizontal structure of the stream function,

$$\psi_h = M\text{sech}^2(r/L_E), \tag{3.15}$$

where L_E is an eddy length scale, giving an expression for η

$$\eta = -fM\text{sech}^2(r/L_E)\frac{F'_m(z)}{N^2(z)}, \tag{3.16}$$

and we can complete the expression for the streamfunction,

$$\psi = M\text{sech}^2(r/L_E)F_m(z). \tag{3.17}$$

Using the streamfunction we compute u and v by equations (2.99) and (2.100). A barotropic mode is added such that the velocity is zero at $z = -H$ by subtracting the bottom level's velocity field. A sea-surface elevation is computed to be consistent with the surface flow. Finally, the linear equation of state (2.7) is inverted to find a salinity field (recall temperature is constant). These are the fields used to initialise the model.

These fields are a good approximation of a quasigeostrophic eddy however the fields are not in perfect balance and the imbalances are due to several mechanisms. One of the first to stand out is that we omit the ageostrophic terms in the solutions for (u, v). A second problem is the difference in numerics between the computation of the initial fields and the MITgcm model. For the initialisation we use analytical derivatives (for example, taking radial derivative of ψ_h) but in the MITgcm a numerical finite difference scheme is used. Thus some imbalance is expected in the fields due to the differences in taking numerical derivatives.

3.5.2   Geostrophic adjustment

The model adjustment is performed by initialising the MITgcm with an above-described eddy and then integrating the model forward for ten days. The idea here is that the fields are very close to steady state and need small changes to achieve this balance. Indeed this is the case; time stepping the model as described produces some small amplitude surface gravity waves that are emitted as the sea-surface height adjusts. The magnitude of these waves is small (order 1 percent of the maximum elevation) which is consistent with our expectation that the fields were very close to balanced. It is desirable to have this adjustment completed before using such an eddy in the internal-wave-eddy setup because the energy fluxes due to the adjustment waves may contaminate the signals of interest.

Table 3.2: Parameters used for the eddy adjustment configuration.

Parameter	Value
Coriolis parameter f	0.5×10^{-4} rad s^{-1}
Reference buoyancy frequency N_0	1.0×10^{-3} rad s^{-1}
Density profile	both (ρ_1 and ρ_2)
Domain size	$500 \times 500 \times 5$ km
Grid cells	$256 \times 256 \times 64$
Horizontal grid spacing (fixed)	1.95 km
Vertical grid spacing (fixed)	78.125 m
Time step	90 s
Duration (days)	10

Table 3.3: Parameters used for the eddy-internal wave configuration.

Parameter	Value
Coriolis parameter f	0.5×10^{-4} rad s^{-1}
Reference buoyancy frequency N_0	1.0×10^{-3} rad s^{-1}
Domain size	$3000 \times 2000 \times 5$ km
Grid cells	$900 \times 540 \times 64$
Grid spacing	2×2 km
Time step	138 s

3.6   Eddy-internal wave configuration

This section describes the primary purpose of this thesis which is to investigate the transfer of energy between eddies and the internal wave field. The domain from the internal wave configuration is extended in the meridional (y) direction to span 2000 km. Periodicity is chosen for the north and south boundaries. Periodicity is chosen because the alternative, solid walls, results in coastally trapped Kelvin waves propagating west along the north boundary and east along the south boundary. This setup provides the reference run referred to later as the no eddy case.

Next the geostrophically adjusted eddies - one clockwise rotating and one counterclockwise rotating are inserted into the domain's initialisation fields. The clockwise (counterclockwise) eddy is stationed 250 km to the west (east) of the ridge, a distance far enough away that it will not impinge upon the ridge. This describes the single eddy case (although there are two eddies), single refers to number of eddies "per side" of the ridge.

The eddy's azimuthal velocity and length scale as well as the barotropic tide velocity are the parameters that we adjust to better understand the effect of each. The fixed parameters are tabulated in Table 3.3.

Chapter 4

Results

The results from the numerical experiments are shown in this chapter. First, the waves generated from the internal wave configuration and second an adjusted eddy from the eddy configuration. Following these are the results from the internal wave-eddy interaction experiments.

4.1 Internal wave configuration

Two model runs are done for the internal wave configuration, one for each of the reference density profiles. The model is initialised from rest ($\vec{u} = 0$) and integrated forward for 15 tidal periods. Snapshots of the model flow variables and time series of energy flux are saved. The barotropic tide of 5 cm s^{-1} starts immediately. However, no shock is introduced because the tide is modelled as a $\sin(t)$ function which takes on a value of zero at $t = 0$.

4.1.1 Linear density profile

First we look at the results from the linear density case after 10.5 tidal periods have elapsed. The baroclinic part of the zonal velocity and the vertical velocity are of interest. Figure 4.1 shows these velocities and the characteristic internal wave patterns expected from tidal flow over topography are clearly visible. Near the ridge, persistent beams have formed and their existence is due to the superposition of many vertical modes. The maximum zonal velocity is 5 cm s^{-1}. The vertical velocities are about one order of magnitude lower at 5 mm s^{-1}.

4.1.2 Nonlinear density profile

Now we look at the nonlinear density case. The same velocity fields as before are shown in Figure 4.2. Notice this time that the beams are still present, however, there
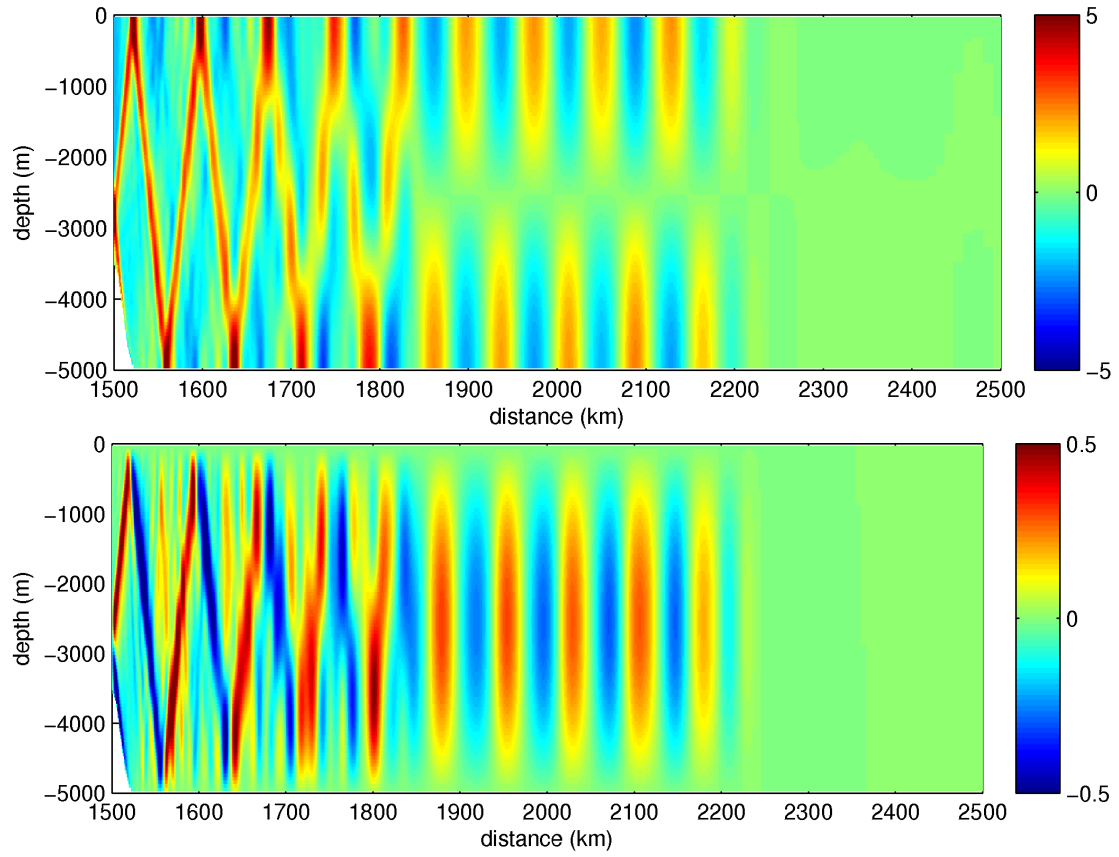
Figure 4.1: Zonal baroclinic velocity in cm s^{-1} (top) and vertical velocity in cm s^{-1} (bottom) from the MITgcm configuration after 10.5 tidal periods have elapsed using the linear density profile. Only the east half of the domain is shown and only up to 2500 km.
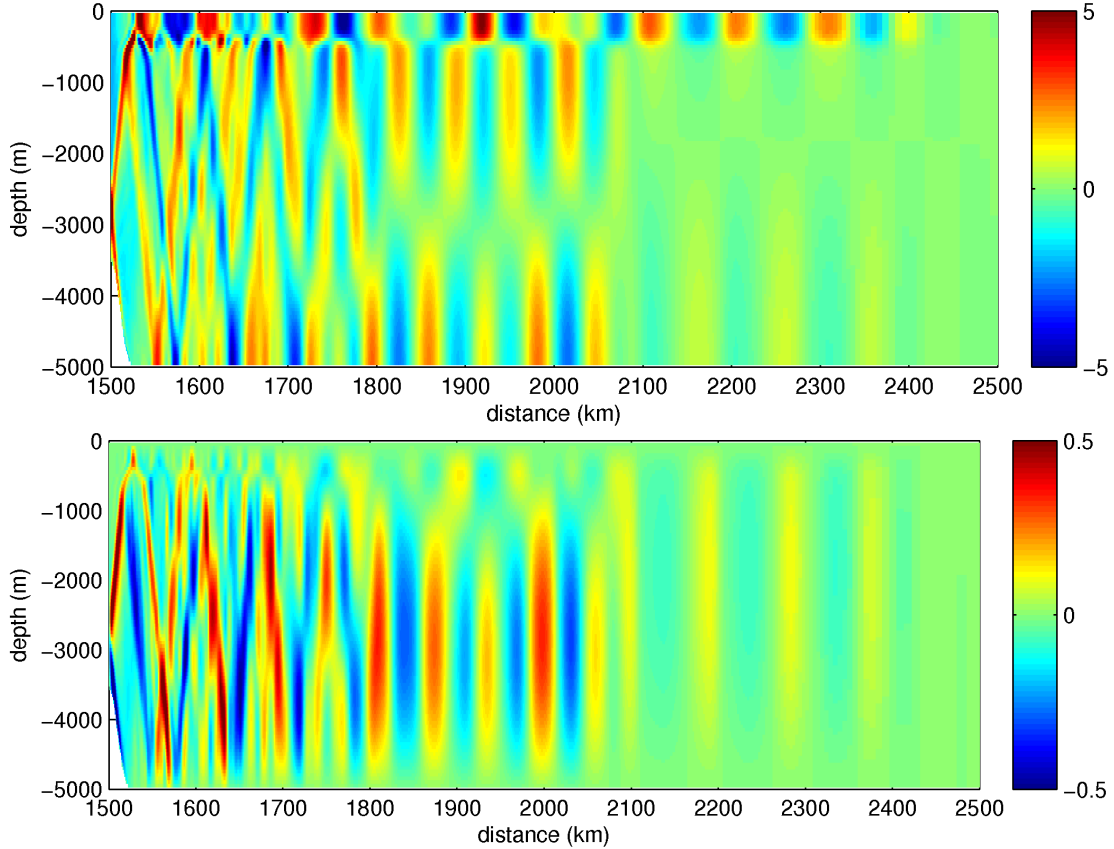
Figure 4.2: Zonal baroclinic velocity in cm s^{-1} (top) and vertical velocity in cm s^{-1} (bottom) from the MITgcm configuration after 10.5 tidal periods have elapsed using the pycnocline density profile. Only the east half of the domain is shown and only up to 2500km.

are some interesting features occurring in and above the pycnocline. Wave energy is concentrated in the pycnocline as well as above and this can be attributed to the shape of the vertical modes obtained by solving the eigenvalue problem in Section 2.2.12. Looking to the east, the vertical structure matches the derivative of the first mode baroclinic eigenfunction. This is a confirmation that we have generated internal waves as the horizontal velocity is decomposed onto the derivatives of the eigenmodes. The maximum zonal velocity is 5 cm s^{-1}, much like the linear case.

4.1.3 Vertical mode decomposition

A vertical mode decomposition is applied to the MITgcm zonal velocity field after 10.5 tidal periods (the same field shown in the upper panel of Figure 4.1 and Figure 4.2). The decomposition onto modes uses the hydrostatic form of the eigenvalue problem for internal waves and ω is fixed at the M_2 tidal frequency. The decom-

position $u_n(x)$ for the first five modes is shown in Figure 4.3 for the linear density case and in Figure 4.4 for the non-linear density.

The first observation is that the distance propagated by each mode reflects the expectation: mode 1 has propagated the furthest, followed by mode 2, 3, etc. There is some difficulty in measuring the group velocity from the model results. Tracking peaks between time levels would be straightforward but would yield the phase velocity rather than group velocity. Instead we use the plots in Figures 4.3 and 4.4 and look for the leading edge of the wave packet to estimate the distance travelled by the wave after 10.5 tidal periods.

To compare this with expectations we also recognise that, due to the free surface method used, there will be a delay before the production of internal waves begins. The barotropic tide is prescribed at the boundary and must propagate along half of the domain before interacting with the topography and producing waves, hence the delay. We compute this delay by taking the distance to the ridge (1500 km) and dividing by the barotropic wave speed (237 m s^{-1}) yielding 1.76 hours (0.14 tidal periods). Taking this delay into account when looking at the leading edge of the $u_n(x)$ plots we can estimate a group velocity for each of the first five modes. Using the hydrostatic group velocity expression (2.66) we get the expected group velocity for the linear density case; an analytic formula for the group velocity in the non-linear density case is not available. The results of the measured and expected group velocities are tabulated in Table 4.1.

Table 4.1: Expected and estimated group velocities for the first five internal wave modes.

Stratification	Mode	Distance (km)	Measured c_g (m s^{-1})	Expected c_g (m s^{-1})
1	1	740	1.60	1.45
1	2	360	0.78	0.72
1	3	280	0.60	0.48
1	4	220	0.47	0.36
1	5	180	0.39	0.29
2	1	950	2.05	N/A
2	2	600	1.29	N/A
2	3	320	0.69	N/A
2	4	250	0.54	N/A
2	5	200	0.43	N/A

One observation we make is that the group velocity for each wave in the linear density case is larger than the expected value. The larger than expected group velocities was also noted by Liu (2009) when comparing model results from the MITgcm to IGW. Future investigation is needed to resolve this as it is currently unexplained.

Figure 4.3: Zonal velocity decomposition $u_n(x)$ for the first five modes for the linear density case. The data is unreliable near the ridge and is removed.

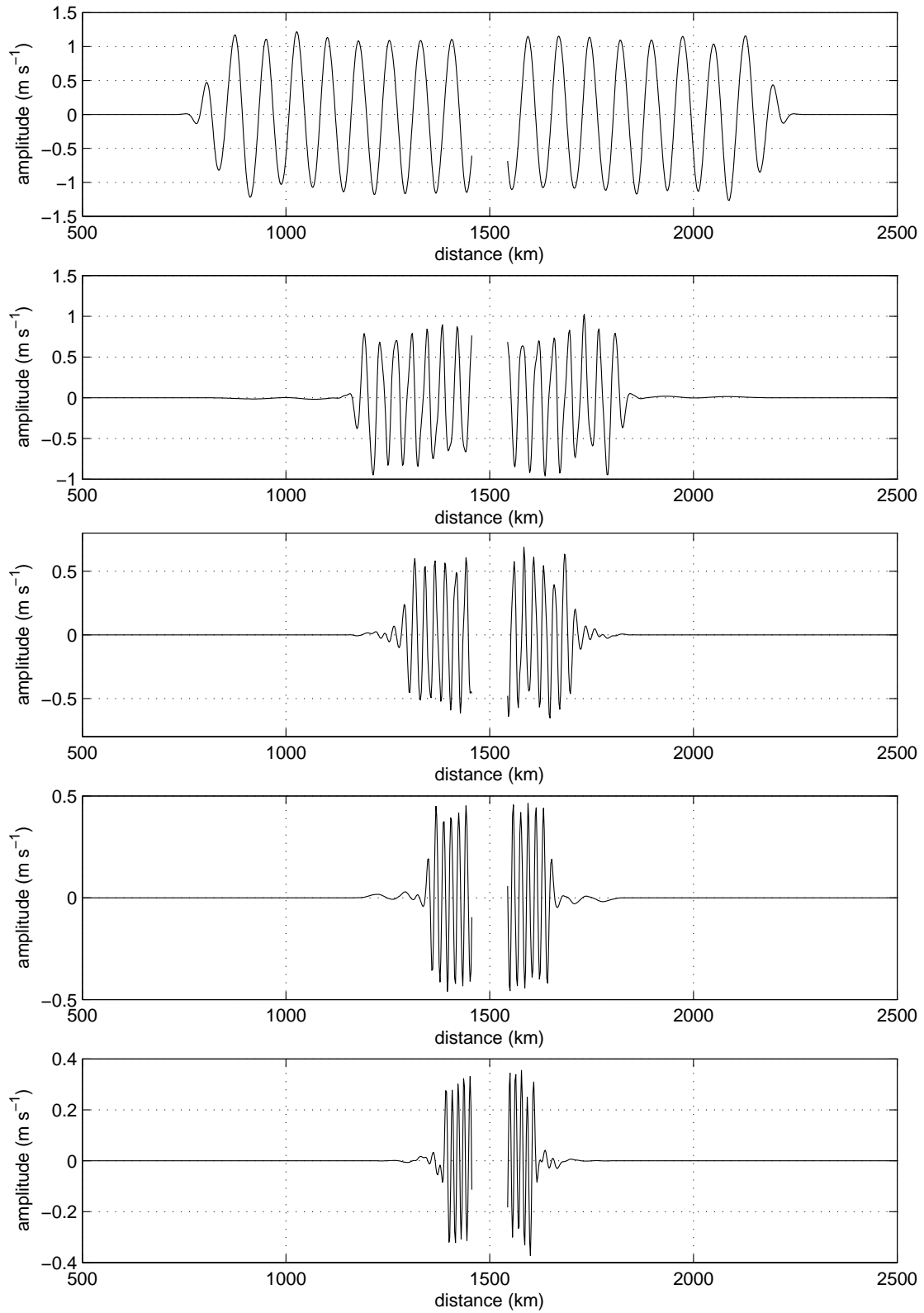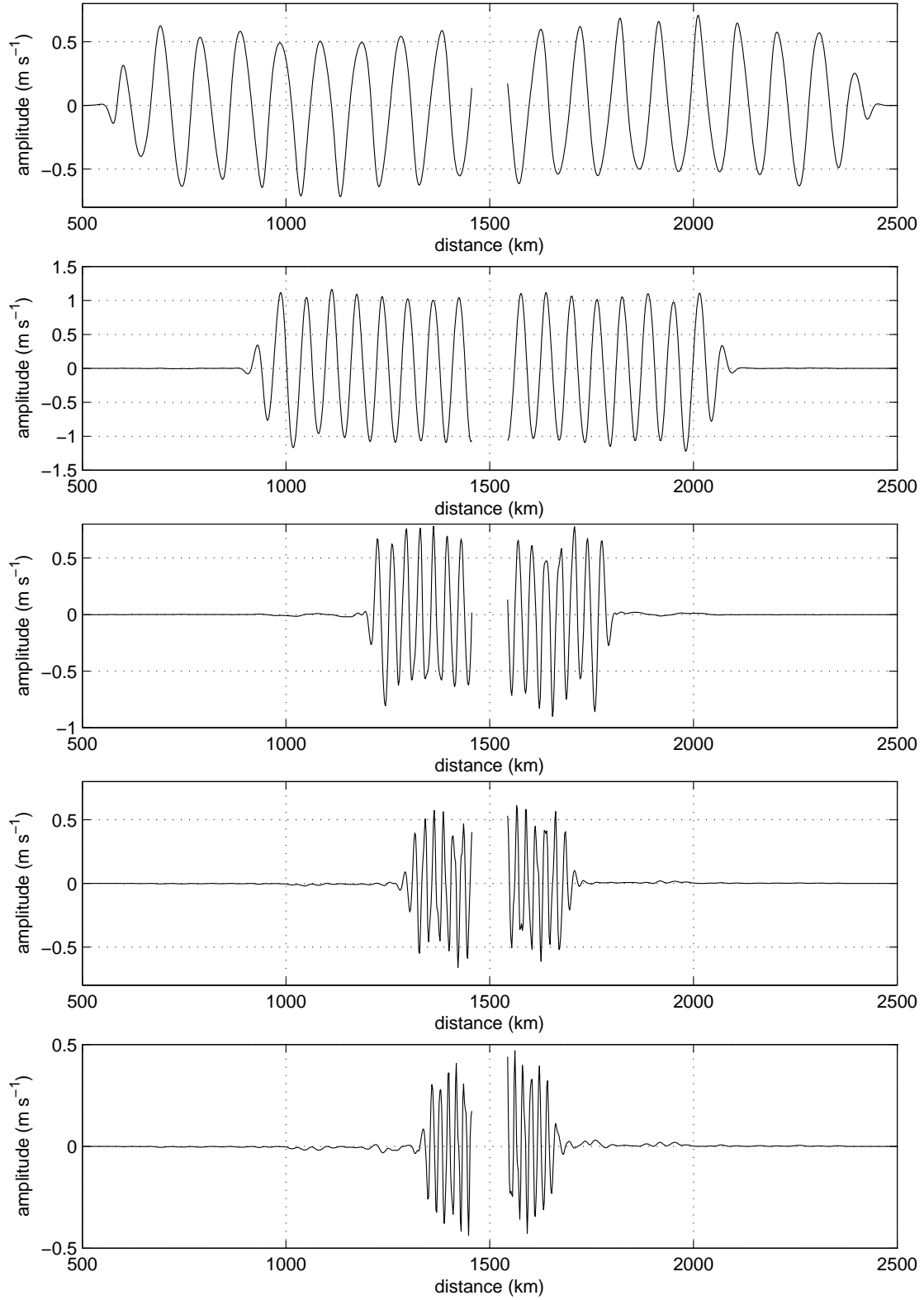Figure 4.4: Zonal velocity decomposition $u_n(x)$ for the first five modes for the non-linear density case. The data is unreliable near the ridge and is removed.

Looking at the equation for group velocity (2.66) we notice that it is proportional to N^3 for the linear stratification. Adding a pycnocline locally increases the value of N, and qualitatively we can expect an increase in group velocity as a result. Indeed this is the case as all of the group velocities measured are larger for the nonlinear case than in the linear case

The decomposition into modes also allows us to quantify the energy in each mode. In the linear stratification case this can be applied to u, v and w for the kinetic energy and to ρ for the potential energy. In the non-linear density case we are restricted to quantifying only the horizontal flow fields. Further, we assume that for a fixed frequency, the partitioning between modes for the vertical velocity and density perturbation roughly matches that of the horizontal velocities.

The fields are decomposed onto vertical modes and associated energies are computed over two regions. The first region is the area between the ridge (but not including the ridge) to the maximum distance that the mode 5 waves have propagated. This distance is 180 (200) km for the linear (non-linear) case. Energy partitioning over this limited area shows how much energy has been produced in each mode and only the first five modes are reported. The data is tabulated in Table 4.2. The second area is the entire domain, again excluding the ridge. The entire domain data shows how much energy is explained by internal waves of tidal frequency; the first eight modes are reported here. The data is tabulated in Table 4.3.

Looking at the first table we see that for the linear case about half of the energy is in the first mode, with roughly half as much in each mode moving down the table. However, in the second case, mode two has half of the energy and the remainder is divided among the other four modes. The main result of this table is that each mode is generated in substantial quantities and the first mode does not overwhelm the rest in amplitude.

The second table shows that the first eight modes explain the vast majority of the internal wave energy present. The residual is insignificant in the linear density case and only a fraction of a percent in the non-linear case. The remaining energy is explained by waves of higher modes, waves of other frequencies and other perturbations.

Table 4.2: Energy breakdown of the fields from the MITgcm after 10.5 tidal periods. The top (bottom) table summarises the linear (non-linear) case. The domain is limited to the first 180 (200) km from the ridge for the linear (non-linear) case and also excludes the area above the ridge. Units are J ρ^{-1}.

Mode	U Velocity	(%)	V Velocity	(%)	W Velocity	(%)	Potential	(%)	Total	(%)
1	1.88e+09	52.76%	4.33e+08	52.05%	3.04e+07	49.06%	1.59e+09	51.25%	3.93e+09	52.03%
2	9.14e+08	25.70%	2.03e+08	24.43%	1.70e+07	27.38%	8.25e+08	26.51%	1.96e+09	25.91%
3	4.20e+08	11.82%	1.11e+08	13.31%	8.63e+06	13.91%	3.76e+08	12.10%	9.16e+08	12.12%
4	2.11e+08	5.95%	4.94e+07	5.95%	3.68e+06	5.93%	1.88e+08	6.04%	4.52e+08	5.99%
5	8.01e+07	2.25%	2.07e+07	2.49%	1.44e+06	2.31%	7.11e+07	2.29%	1.73e+08	2.29%
Sum	3.50e+09	98.47%	8.17e+08	98.23%	6.12e+07	98.59%	3.05e+09	98.18%	7.43e+09	98.33%
Residual	5.42e+07	1.53%	1.47e+07	1.77%	8.72e+05	1.41%	5.67e+07	1.82%	1.27e+08	1.67%
Total	3.56e+09	47.03%	8.31e+08	11.00%	6.21e+07	0.82%	3.11e+09	41.15%	7.56e+09	100.00%

Mode	U Velocity	(%)	V Velocity	(%)	W Velocity	(%)	Potential	(%)	Total	(%)
1	5.13e+08	13.37%	1.44e+08	14.77%	N/A	N/A%	N/A	N/A%	N/A	N/A%
2	1.88e+09	49.10%	4.75e+08	48.70%	N/A	N/A%	N/A	N/A%	N/A	N/A%
3	7.24e+08	18.85%	1.82e+08	18.69%	N/A	N/A%	N/A	N/A%	N/A	N/A%
4	3.77e+08	9.82%	8.92e+07	9.14%	N/A	N/A%	N/A	N/A%	N/A	N/A%
5	1.42e+08	3.69%	3.30e+07	3.38%	N/A	N/A%	N/A	N/A%	N/A	N/A%
Sum	3.64e+09	94.84%	9.24e+08	94.68%	N/A	N/A%	N/A	N/A%	N/A	N/A%
Residual	1.98e+08	5.16%	5.20e+07	5.32%	N/A	N/A%	N/A	N/A%	N/A	N/A%
Total	3.84e+09	46.41%	9.76e+08	11.81%	5.20e+07	0.63%	3.40e+09	41.15%	8.27e+09	100.00%

55

Table 4.3: Energy breakdown of the fields from the MITgcm after 10.5 tidal periods. The top (bottom) table summarises the linear (non-linear) case. Only the area above the ridge is excluded. Units are J ρ^{-1}.

Mode	U Velocity	(%)	V Velocity	(%)	W Velocity	(%)	Potential	(%)	Total	(%)
1	8.12e+09	75.99%	1.03e+09	76.10%	1.39e+08	74.16%	7.05e+09	75.33%	1.63e+10	75.70%
2	1.75e+09	16.38%	2.22e+08	16.40%	3.37e+07	17.93%	1.55e+09	16.54%	3.55e+09	16.47%
3	5.01e+08	4.69%	6.12e+07	4.52%	9.21e+06	4.90%	4.46e+08	4.76%	1.02e+09	4.72%
4	1.95e+08	1.83%	2.42e+07	1.79%	3.57e+06	1.90%	1.75e+08	1.87%	3.98e+08	1.84%
5	7.24e+07	0.68%	9.60e+06	0.71%	1.30e+06	0.69%	6.61e+07	0.71%	1.49e+08	0.69%
6	3.19e+07	0.30%	4.27e+06	0.32%	5.22e+05	0.28%	2.97e+07	0.32%	6.64e+07	0.31%
7	9.42e+06	0.09%	1.17e+06	0.09%	1.61e+05	0.09%	9.45e+06	0.10%	2.02e+07	0.09%
8	2.73e+06	0.03%	6.56e+05	0.05%	3.95e+04	0.02%	2.56e+06	0.03%	5.99e+06	0.03%
Sum	1.07e+10	99.99%	1.35e+09	99.97%	1.88e+08	99.97%	9.33e+09	99.65%	2.16e+10	99.84%
Residual	1.25e+06	0.01%	4.38e+05	0.03%	5.19e+04	0.03%	3.23e+07	0.35%	3.41e+07	0.16%
Total	1.07e+10	49.48%	1.35e+09	6.27%	1.88e+08	0.87%	9.36e+09	43.38%	2.16e+10	100.00%

Mode	U Velocity	(%)	V Velocity	(%)	W Velocity	(%)	Potential	(%)	Total	(%)
1	2.82e+09	26.82%	3.66e+08	26.93%	N/A	N/A%	N/A	N/A%	N/A	N/A%
2	5.89e+09	55.92%	7.63e+08	56.14%	N/A	N/A%	N/A	N/A%	N/A	N/A%
3	1.14e+09	10.85%	1.48e+08	10.92%	N/A	N/A%	N/A	N/A%	N/A	N/A%
4	3.61e+08	3.43%	4.26e+07	3.13%	N/A	N/A%	N/A	N/A%	N/A	N/A%
5	1.36e+08	1.29%	1.56e+07	1.15%	N/A	N/A%	N/A	N/A%	N/A	N/A%
6	1.08e+08	1.02%	1.36e+07	1.00%	N/A	N/A%	N/A	N/A%	N/A	N/A%
7	3.73e+07	0.35%	5.06e+06	0.37%	N/A	N/A%	N/A	N/A%	N/A	N/A%
8	1.82e+07	0.17%	2.40e+06	0.18%	N/A	N/A%	N/A	N/A%	N/A	N/A%
Sum	1.05e+10	99.86%	1.36e+09	99.81%	N/A	N/A%	N/A	N/A%	N/A	N/A%
Residual	1.47e+07	0.14%	2.57e+06	0.19%	N/A	N/A%	N/A	N/A%	N/A	N/A%
Total	1.05e+10	49.06%	1.36e+09	6.34%	1.23e+08	0.58%	9.44e+09	44.02%	2.14e+10	100.00%

4.1.4 Comparison with Dr. Lamb's model

For further confirmation that the model is operating properly, the same configuration is setup using Dr. Lamb's model IGW. There are a few differences between IGW and the MITgcm configuration that make an exact comparison difficult, however a qualitative comparison is still possible. The differences are

1. In MITgcm the hydrostatic assumption is made; in IGW the non-hydrostatic equations are used.

2. In MITgcm z levels with partial steps are used; in IGW terrain-following coordinates (also called sigma levels) are used.

3. In MITgcm a free surface is used; in IGW a rigid lid is imposed.

The first two differences are not expected to be important except for a slight difference in propagation speeds, however the last difference will have impact on the comparison. With a rigid lid the barotropic tide has an infinite wavelength and with a free surface the tide has a finite wavelength. The consequence of this discrepancy is that upon initialisation in the rigid lid case the ridge will immediately be subject to the barotropic tide. In the free surface case the wave will need to propagate almost halfway across the domain before interacting with the ridge. Thus a phase shift is expected when comparing waves generated by MITgcm and IGW. In spite of this, the wave magnitudes, modes and energy fluxes are expected to be comparable.

4.1.4.1 Baroclinic velocities

Plots of the baroclinic zonal velocity and of the vertical velocity obtained from IGW are shown in Figure 4.5 for the linear density profile and in Figure 4.6 for the nonlinear density profile. These figures should be compared with Figures 4.1 and 4.2. The snapshots are taken after 10.39 tidal periods have elapsed. The earlier time used here for the IGW snapshots accounts for the expected phase shift of 0.14 tidal periods and was the closest saved snapshot to 10.36 tidal periods. A visual inspection of the plots reveals that the fields are very similar and thus we conclude that the MITgcm is working well in producing internal waves.

4.1.4.2 Energy flux

A time series depicting the energy flux passing a point 250 km to the east of the ridge is shown for the linear density case in Figure 4.7. Curves for MITgcm and IGW are shown in the top two panels. The dashed line shows the energy flux and the solid line shows a sliding time average one tidal period wide. The bottom panel overlays the curves for comparison, however two modifications are made. First, the expected phase shift of 1.76 hours (0.14 tidal periods) is applied to the MITgcm

Figure 4.5: Zonal baroclinic velocity (m/s) (top) and vertical velocity (bottom) from the IGW configuration after 10.39 tidal periods have elapsed using the linear density profile. Only the east half of the domain is shown and only up to 2500km.
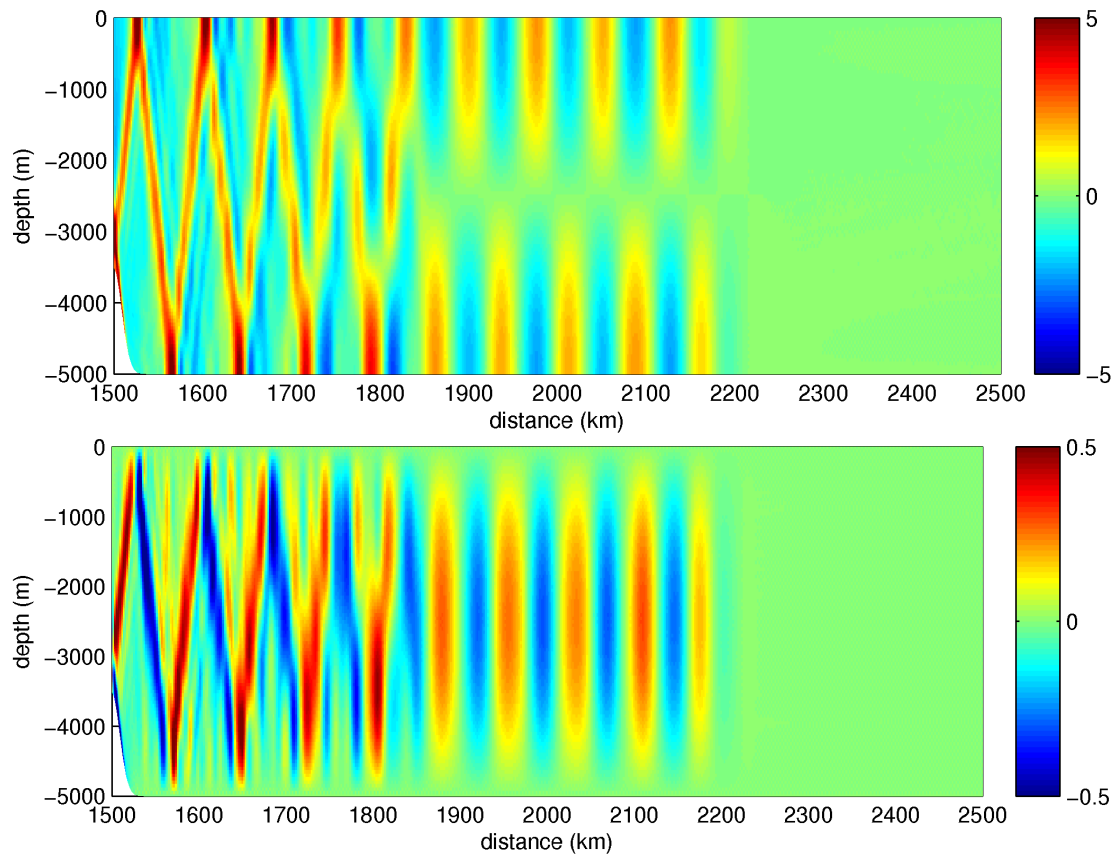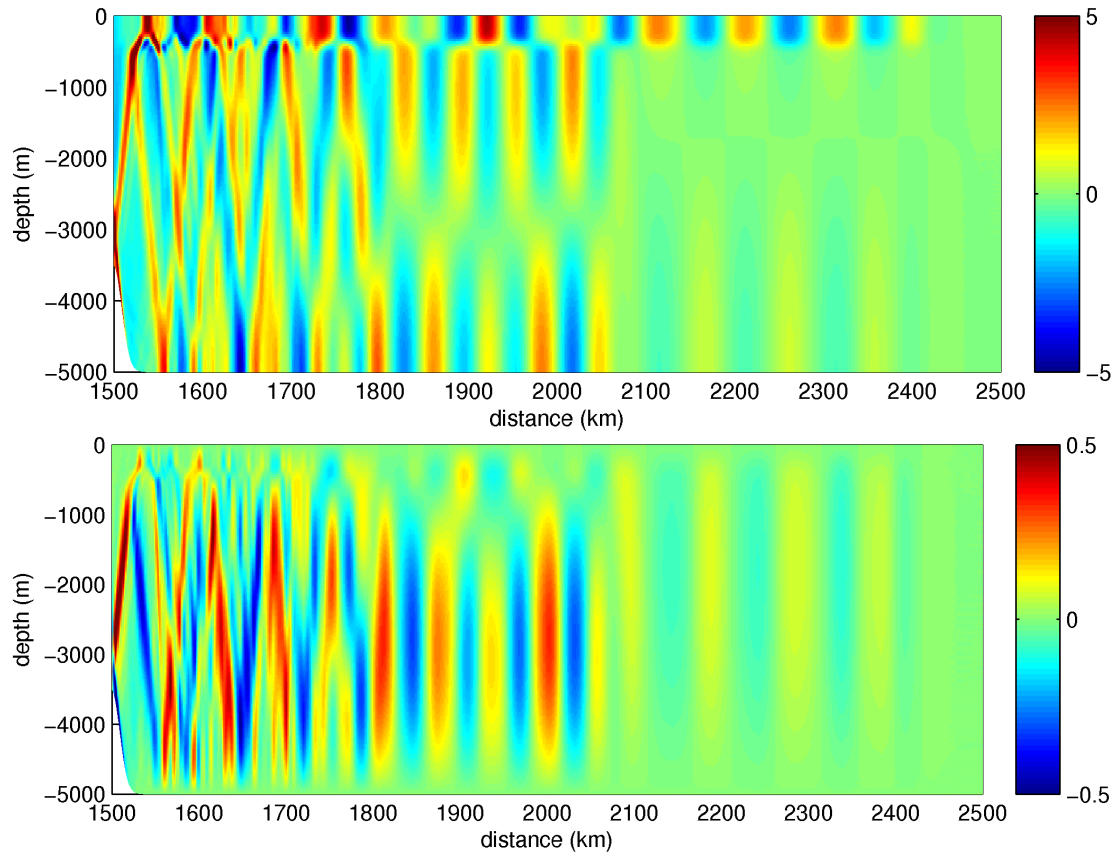
Figure 4.6: Zonal baroclinic velocity (m/s) (top) and vertical velocity (bottom) from the IGW configuration after 10.39 tidal periods have elapsed using the pycnocline density profile. Only the east half of the domain is shown and only up to 2500km.

data and, by inspection, we see that the arrival of the first waves matches well. Second, the MITgcm data has been reduced in magnitude by 10% and this brings the average level into good agreement.

The phase shift is expected and explained. The reason for the overestimate of the energy flux by the MITgcm is not immediately clear. One possibility is that the larger group velocity observed from MITgcm is responsible for the larger energy flux. Energy flux is energy density multiplied by group velocity, so an overestimated group velocity could explain the overestimate of energy flux.

The same curves are shown for the non-linear density case in Figure 4.8. The curves are similar to those in the linear density case. We notice that the first waves arrive about half a tidal period earlier; this is explained by the larger propagation speed observed for the mode 1 waves. The average energy flux level is similar between the density cases beyond 12 tidal periods.

4.2   Eddy configuration

The results of this section show the results of geostrophic adjustment of two baroclinic eddies. The adjustment is similar for the other eddies that are used in the next section.

4.2.1   Linear density profile

A clockwise eddy is initialised with a maximum surface velocity of U_{max}=25 cm s^{-1} and a length scale L_E of 50 km. The resulting cross section after ten days of adjustment is shown in Figure 4.9. We observe first that the sea-surface height has dropped 3.1 cm at the centre of the eddy. Second we notice that there is an increase in the eddy's azimuthal velocity of 3.7 cm s^{-1}. An increase in velocity after adjustment indicates that the sea surface gradient was too high upon initialisation and acted to accelerate the flow. This is consistent with the sea-surface dropping as it adjusts; the velocities were not strong enough to support the original elevation field and an equilibrium is reached.

The general shape of the eddy has not changed significantly with the adjustment. The density contours show isopycnal displacements of about 400 metres which is comparable to the displacements depicted in the hydrographic sections shown in Section 2.3.

4.2.2   Nonlinear density profile

A similar clockwise eddy is adjusted using the non-linear density profile and the cross section is shown in Figure 4.10. A 2.9 cm reduction in sea surface height is observed as well as a 5.7 cm s^{-1} increase in azimuthal velocity. The vertical

Figure 4.7: Energy flux for the linear stratification passing a point 250 km to the east of the ridge for MITgcm (top), IGW (middle), both (bottom). The dashed line shows the energy flux and the solid line shows a sliding average one tidal period wide. The MITgcm data on the bottom panel has been adjusted to best match IGW by (a) a phase shift of 0.14 tidal periods and (b) a reduction in magnitude of 10%.

61

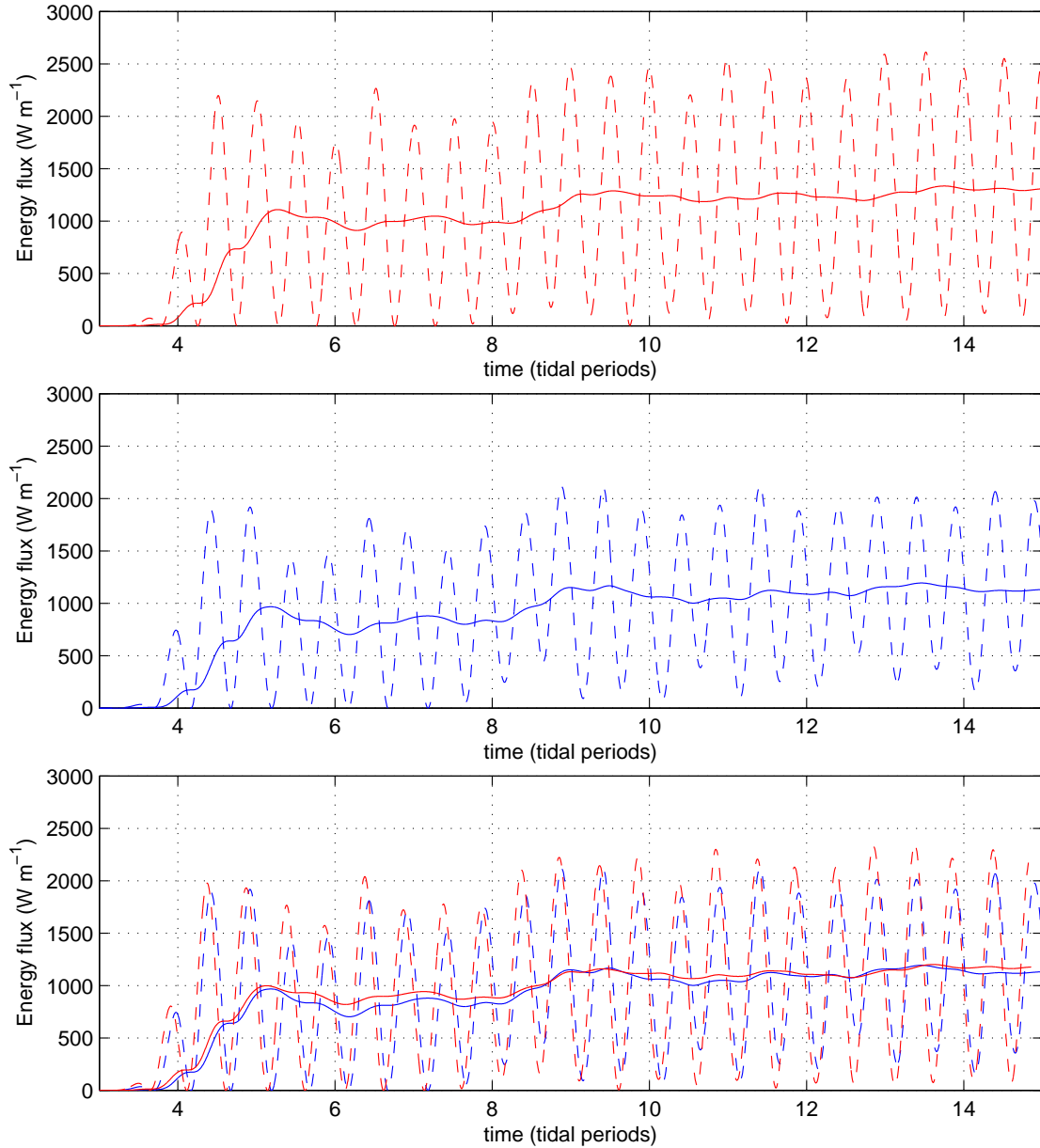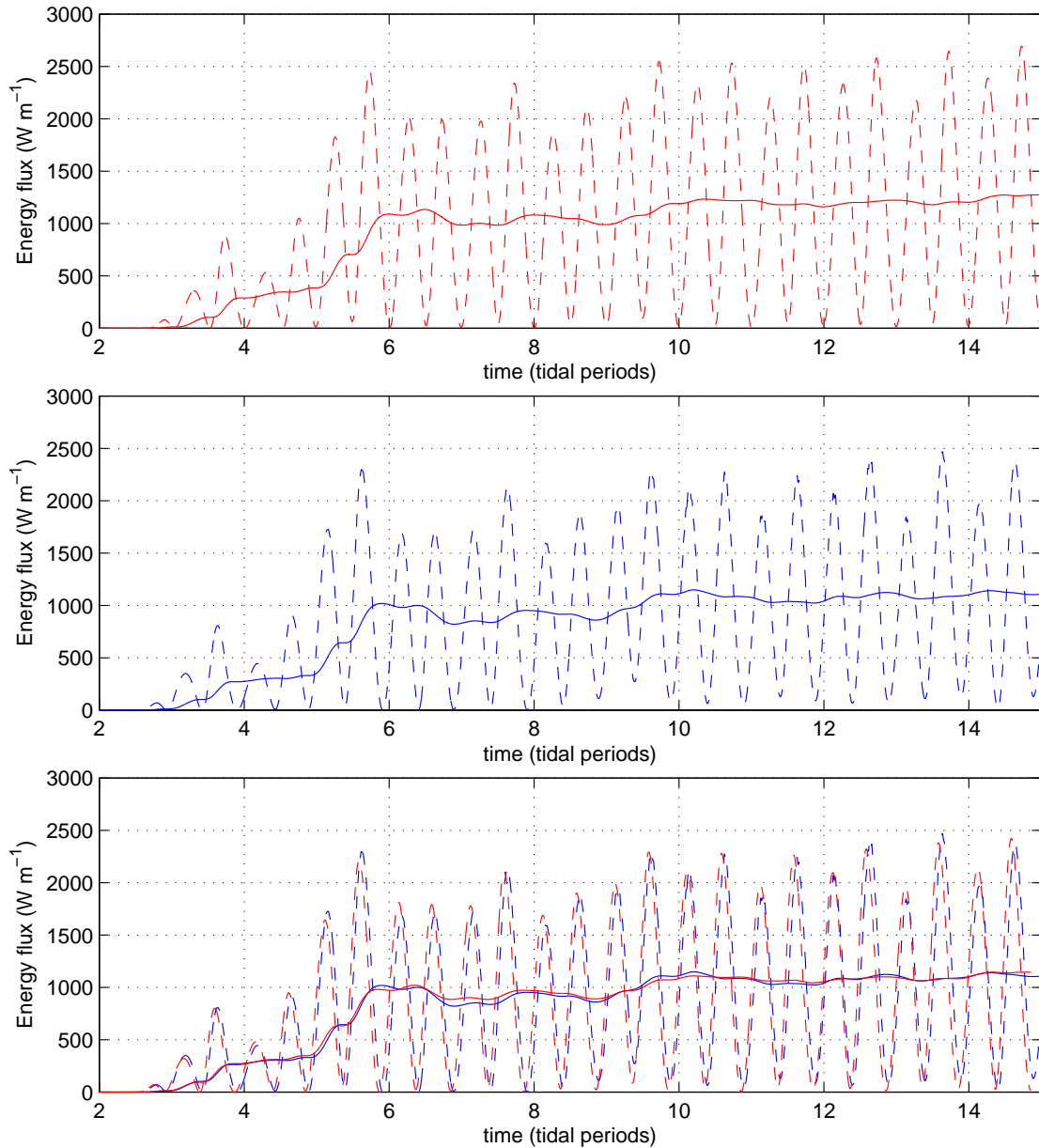Figure 4.8: Energy flux for the non-linear stratification passing a point 250 km to the east of the ridge for MITgcm (top), IGW (middle), both (bottom). The dashed line shows the energy flux and the solid line shows a sliding average one tidal period wide. The MITgcm data on the bottom panel has been adjusted to best match IGW by (a) a phase shift of 0.14 tidal periods and (b) a reduction in magnitude of 10%.

Figure 4.9: Cross section of a baroclinic eddy after it has been adjusted in MITgcm ($\bar{\rho}_1$ case). The panels show: (top) sea-surface elevation, initial is dashed and final is solid, (second) density contours in kg m^{-3}, (third) zonal cross section of meridional velocity in cm s^{-1}, (bottom) final minus initial zonal cross section of meridional velocity in cm s^{-1}. The eddy length scale is 50 km, the azimuthal velocity is 50 cm s^{-1}, although it increased slightly during adjustment.

structure is quite different from the constant N case in that the velocities are concentrated above the main pycnocline. The velocity is quite weak below the pycnocline, and this vertical structure is consistent with the eigenfunction shown in Figure 3.4.

4.3   Eddy-internal wave configuration

This section describes the results obtained from the eddy-internal wave interaction experiments.

The parameters we vary in the interaction experiments are the stratification ($\bar{\rho}(z)$), barotropic tide velocity (U_{BT}), eddy length scale (L_E) and maximum azimuthal eddy velocity (U_θ).

Ideally, we should run a large number of cases to fully explore the parameter space. For example, considering two density profiles and five values for each of U_{BT}, U_θ and L_E leads to a requirement of 250 runs. Considering multi-eddy runs would raise this even further. Limitations on time and computing resources make this difficult to achieve. Instead we present a subset of runs. The chosen runs and their parameters are listed in Table 4.4.

The table is partitioned into four parts. The first part varies only the azimuthal velocity and allows us to investigate the effects of eddy speed. The second part does the same except with the non-linear density profile. The third part repeats two of the first runs with a reduced eddy length scale. Finally, the fourth part returns to the original eddy length scale and increases the barotropic tidal velocity.

4.3.1   Effect of azimuthal velocity

First we look at the "A" series of runs that use the linear density profile. Energy flux plots averaged over one tidal period are drawn for each value of U_θ in Figures 4.11 through 4.15. The runs are 25 tidal periods in length and the average is taken over the last tidal period in the simulation. The masked out area removes the regions where the calculation of energy flux is not useful (the eddy and the ridge), as well as where the grid spacing becomes large. The black lines indicate the points used to estimate the beam angles.

From the group velocities measured in Section 4.1.3 we estimate the distance travelled by modes one through three at 1780, 860 and 670 km, respectively. From Figure 4.11 we see that the energy flux level shifts around 2000 km and again around 2300 km. These distances correspond to the wave front of the mode three and two waves, respectively. Each of these distances is large enough such that the corresponding modes will be well past the eddy location after 25 tidal periods. This ensures that the eddy has interacted with at least the first 3 modes.
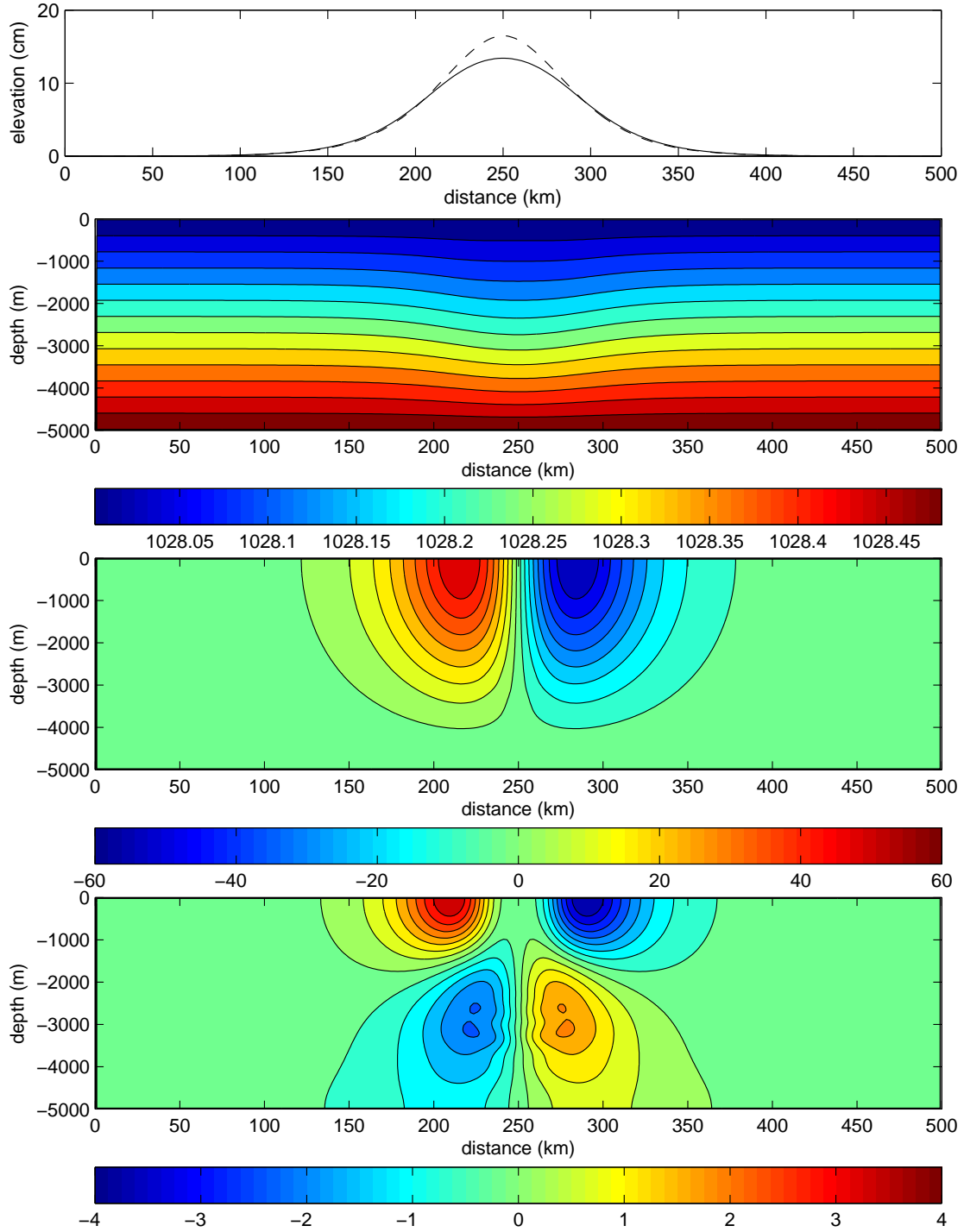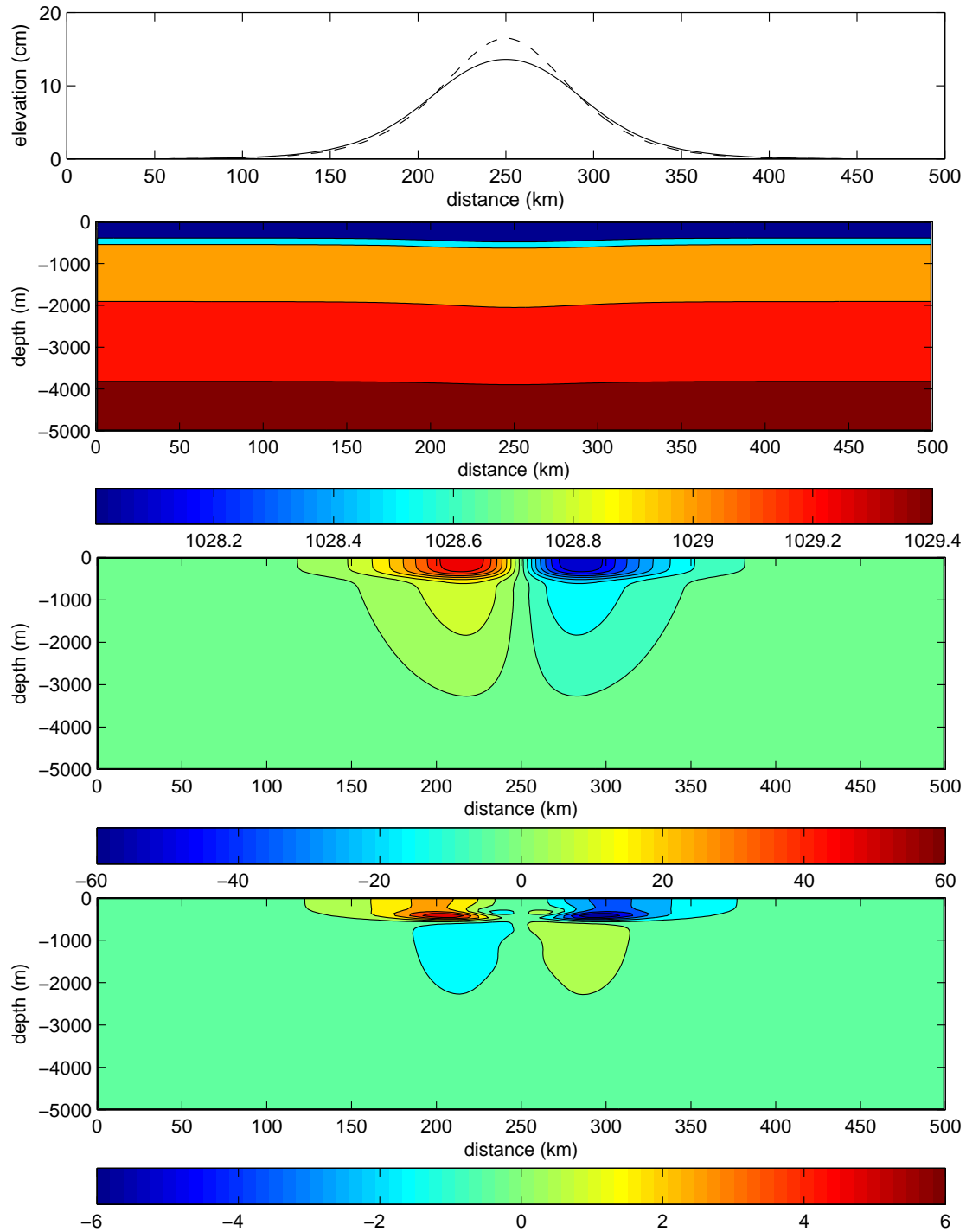
Figure 4.10: Cross section of a baroclinic eddy after it has been adjusted in MITgcm ($\bar{\rho}_2$ case). The panels show: (top) sea-surface elevation, initial is dashed and final is solid, (second) density contours in kg m^{-3}, (third) zonal cross section of meridional velocity in cm s^{-1}, (bottom) final minus initial zonal cross section of meridional velocity in cm s^{-1}. The eddy length scale is 50 km, the azimuthal velocity is 50 cm s^{-1}, although it increased slightly during adjustment.

Table 4.4: Summary of runs

Run Name	Stratification	U_{BT} (cm s^{-1})	L_E (km)	U_θ (cm s^{-1})
A1	$\bar{\rho}_1$	5	-	0
A2	$\bar{\rho}_1$	5	50	10
A3	$\bar{\rho}_1$	5	50	25
A4	$\bar{\rho}_1$	5	50	50
A5	$\bar{\rho}_1$	5	50	75
B1	$\bar{\rho}_2$	5	-	0
B2	$\bar{\rho}_2$	5	50	10
B3	$\bar{\rho}_2$	5	50	25
B4	$\bar{\rho}_2$	5	50	50
B5	$\bar{\rho}_2$	5	50	75
C3	$\bar{\rho}_1$	5	25	25
C4	$\bar{\rho}_1$	5	25	50
D1	$\bar{\rho}_1$	10	-	0
D2	$\bar{\rho}_1$	10	50	10
D3	$\bar{\rho}_1$	10	50	25
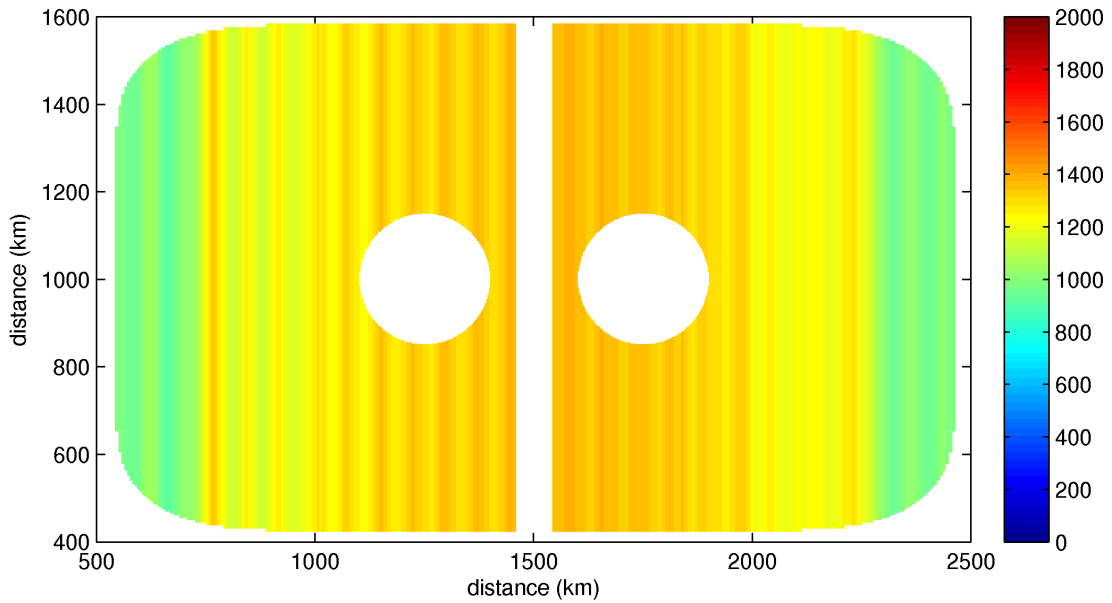
Figure 4.11: Baroclinic energy flux magnitude for the A1 run. This is the reference run with the linear density profile as no eddies are present. Units are W m^{-1}.
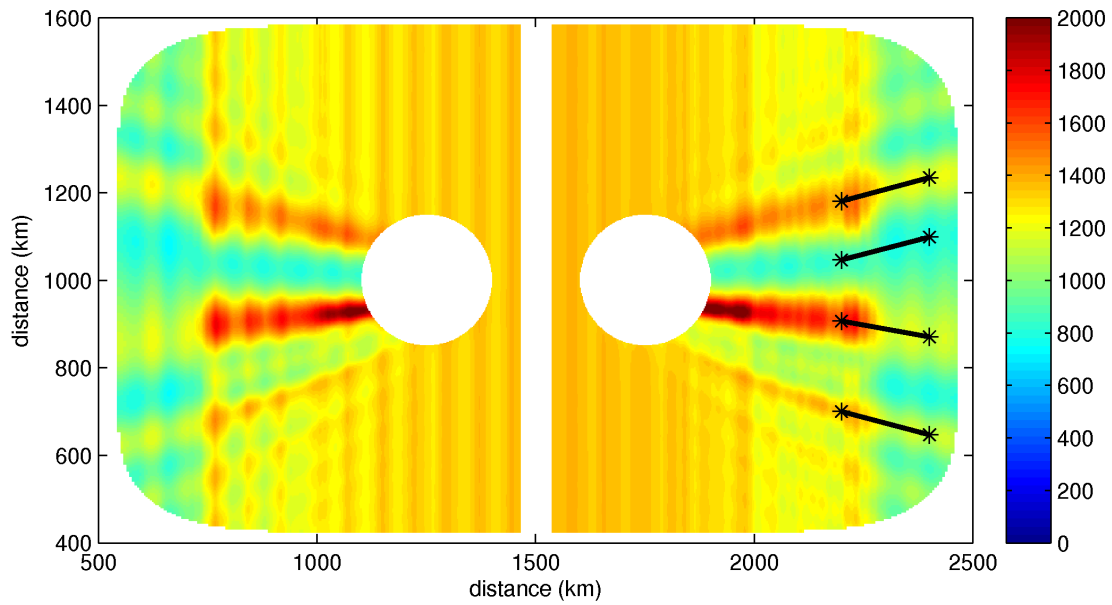
Figure 4.12: Baroclinic energy flux magnitude for the A2 run. L_E is 50 km and U_θ is 10 cm s^{-1}. Units are W m^{-1}.
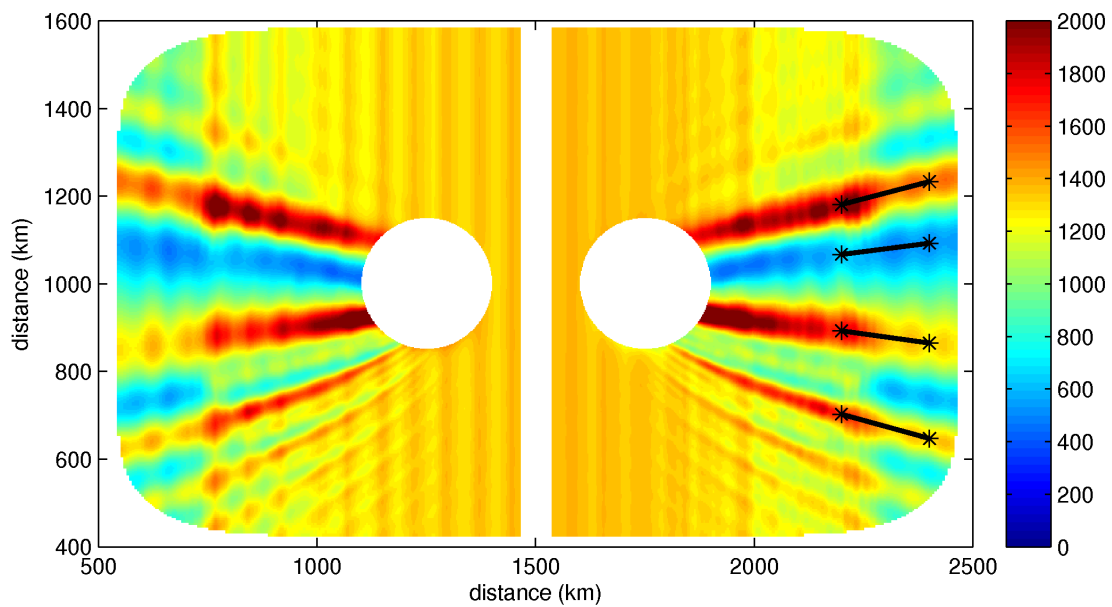
Figure 4.13: Baroclinic energy flux magnitude for the A3 run. L_E is 50 km and U_θ is 25 cm s^{-1}. Units are W m^{-1}.
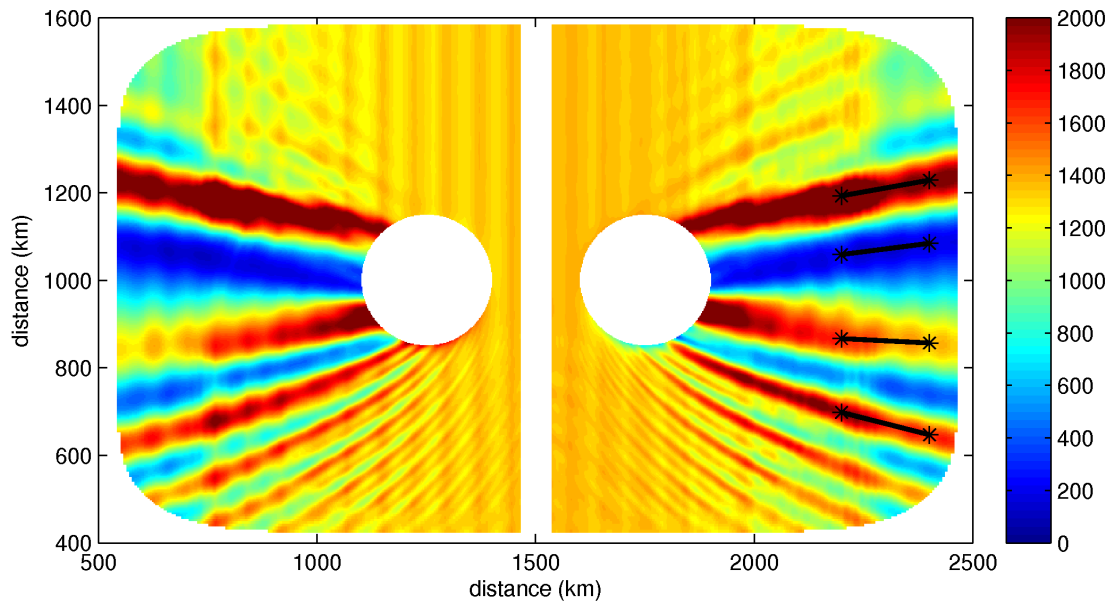
Figure 4.14: Baroclinic energy flux magnitude for the A4 run. L_E is 50 km and U_θ is 50 cm s^{-1}. Units are W m^{-1}.
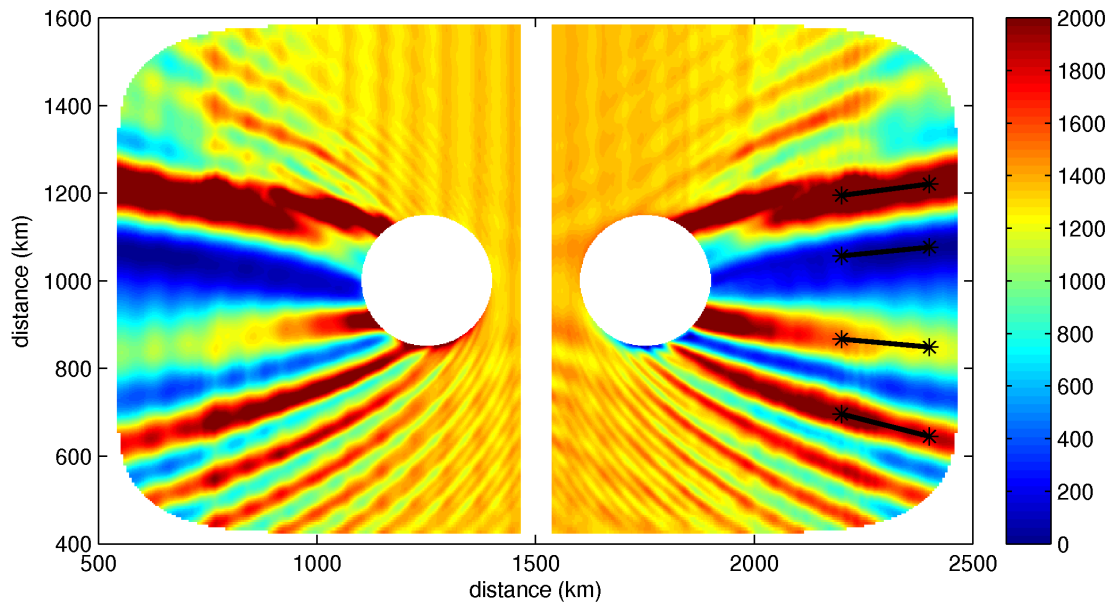
Figure 4.15: Baroclinic energy flux magnitude for the A5 run. L_E is 50 km and U_θ is 75 cm s^{-1}. Units are W m^{-1}.

For the eddy cases, the most visible effect is the production of focusing and shadow regions in the wake of the eddy. They are comparable for the anticyclonic (east) eddy and the cyclonic (west) eddy in the sense that they are reflected about the ridge. The plots with non-zero eddies are similar in that they all contain two main focusing beams, one tilted north and one tilted south. A single main shadow region is also prominent, and is tilted slightly north. There are a number of smaller and weaker beams that are much more evident in the stronger eddy cases.

The approximate angle of four primary beams is measured across the "A" runs to see how the velocity of the eddy affects the angle. We label the beams from north to south beginning with the most intense beam (Focus 1), followed by Shadow 1, Focus 2 and Focus 3. There is a shadow beam between Focus 2 and Focus 3 but it is weakly defined for the low eddy velocity cases. The angles are measured between two points with fixed x positions and y positions determined by seeking the local maximum/minimum in a beam. The eddy flux figures contain a black line along each beam, and the angle of this line is what is reported here. The results of the measurements are tabulated in Table 4.5

Table 4.5: Angle of focus/shadow beams for the A series of runs (in degrees)

U_θ (cm s^{-1})	Focus 1 (degrees)	Shadow 1 (degrees)	Focus 2 (degrees)	Focus 3 (degrees)
10	15.0	14.5	-10.1	-14.8
25	14.5	7.4	-7.9	-15.4
50	10.2	7.4	-2.8	-14.3
75	7.4	5.7	-5.1	-14.3

The main focusing beam "Focus 1" has a consistent angle at low velocities but at high velocities decreases somewhat. At higher velocities, particularly 75 cm s^{-1} the beam appears to be broken into two parts, a part near the eddy with a large angle and a part further from the eddy with reduced angle. The shadow region shows an almost consistent decreasing angle with increasing eddy velocity. The second data value may be an outlier due to the local minimum method of deciding the angle. The second focusing beam also shows a consistent decreasing trend, again with a single outlier. Finally, the third focusing beam is quite consistent in angle. Overall the trend shows that the angle of the focusing/shadow regions decreases as the eddy velocity increases.

At 2200 and 2400 km we take a meridional section of the energy flux magnitude and plot in for each value of U_θ in Figure 4.16. Reading the curves from left to right corresponds to north to south in the energy flux pseudo colour plots. The curves show that the intensity of the beams increases with eddy azimuthal velocity in the focusing regions and decreases in the shadow regions. The constant energy flux values from the no eddy case are also shown, 952 and 1200 W m^{-1} at 2200 and 2400 km, respectively. The magnitude of the intensification at 2400 km was unexpected; in the shadow region the intensity of energy flux almost reaches zero

and in the upper focusing region the intensity is almost doubled. The trend is quite clear: increasing eddy azimuthal velocity increases (decreases) the energy flux in the focusing (shadow) regions. The values from the peaks and troughs of Figure 4.16 are tabulated in Table 4.6.

Table 4.6: Intensification of energy flux in the focus/shadow beams for the "A" series of runs. The values here are the peaks/troughs of the curves in Figure 4.16. The reference values from the no eddy case are 952 and 1200 W m^{-1} at 2200 and 2400 km, respectively.

U_θ (cm s^{-1})	Distance (km)	Focus 1 (W m^{-1})	Shadow 1 (W m^{-1})	Focus 2 (W m^{-1})	Focus 3 (W m^{-1})
10	2200	1413	866	1612	1341
25	2200	1938	645	1740	1641
50	2200	2481	223	1663	1916
75	2200	2546	122	1564	2077
10	2400	1148	780	1108	1087
25	2400	1470	517	1278	1304
50	2400	1981	170	1349	1629
75	2400	2302	17	1189	1831

4.3.2   Effect of non-linear density profile

We look now at the "B" runs where the density profile has been modified to include a pycnocline. Figures 4.17 through 4.21 show the same magnitude of energy flux averaged over the last tidal period as before. The angles and intensifications are also measured as before and are tabulated in Table 4.7 and 4.8. The meridional sections are shown in Figure 4.22.

Table 4.7: Angle of focus/shadow beams for the "B" series of runs (in degrees)

U_θ (cm s^{-1})	Focus 1 (degrees)	Shadow 1 (degrees)	Focus 2 (degrees)	Focus 3 (degrees)
10	10.2	6.8	-7.4	-18.0
25	10.2	6.8	-7.4	-17.5
50	10.7	6.8	-6.8	-17.6
75	10.2	6.8	-6.2	-17.6

The energy flux figures reveal similar patterns as were observed in the linear density case. The beams intensify with increasing azimuthal velocity. We also notice that with the larger velocities the primary focusing beam again appears to be a superposition of two or more beams.
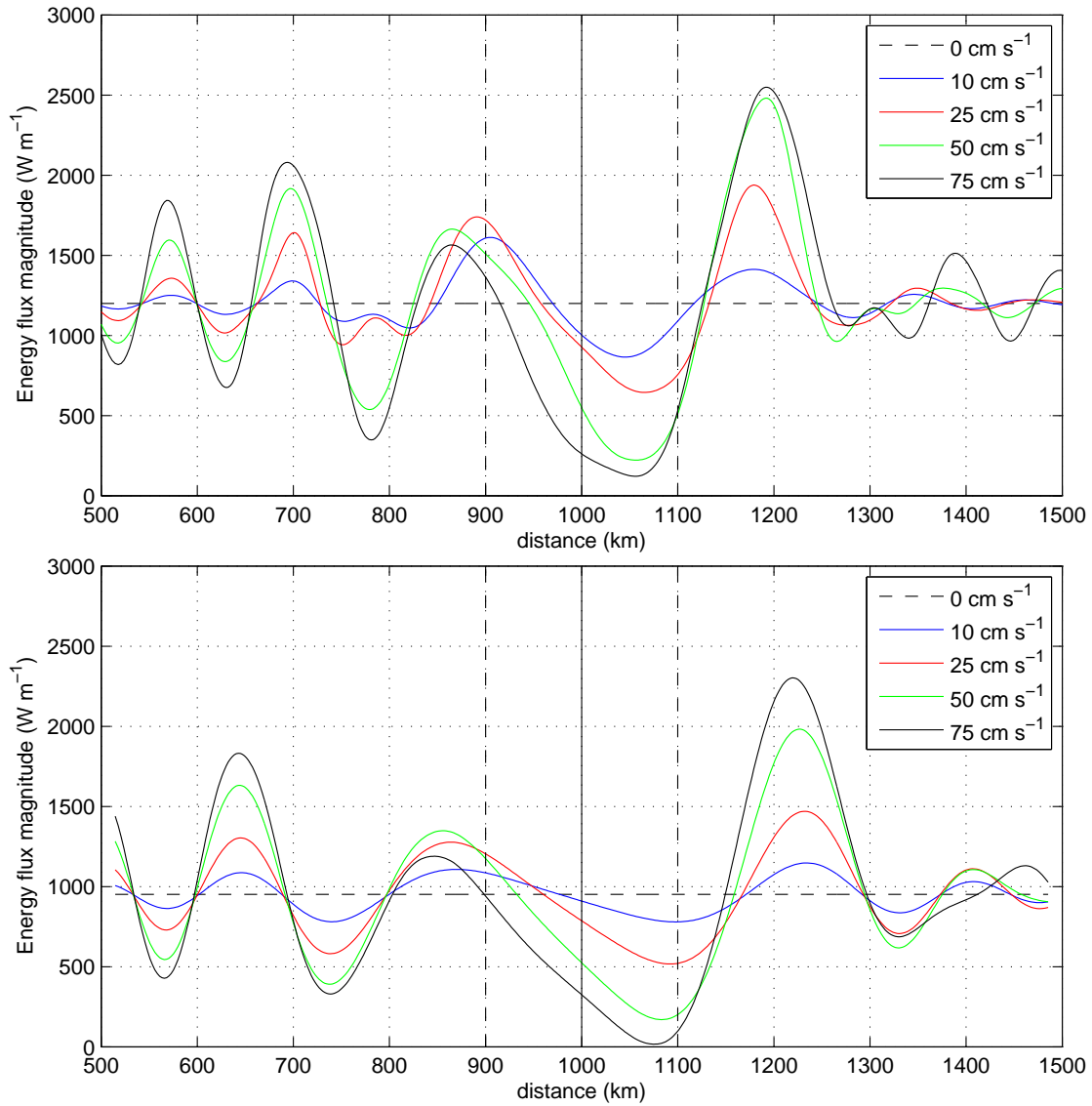
Figure 4.16: Magnitude of energy flux at 2200 km (top) and 2400 km (bottom) from the "A" series of runs. The solid vertical line indicates the centre of the eddy and the dashed vertical lines are drawn $2L_E$ away, roughly indicating the eddy size.
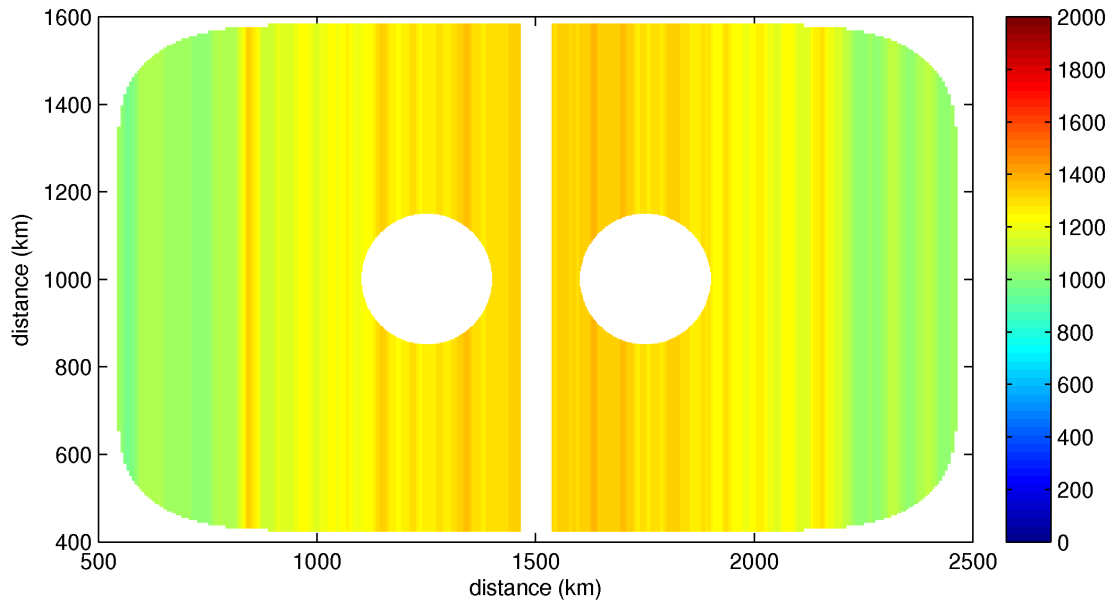
Figure 4.17: Baroclinic energy flux magnitude for the B1 run. This is the reference run with the linear density profile as no eddies are present. Units are W m^{-1}.
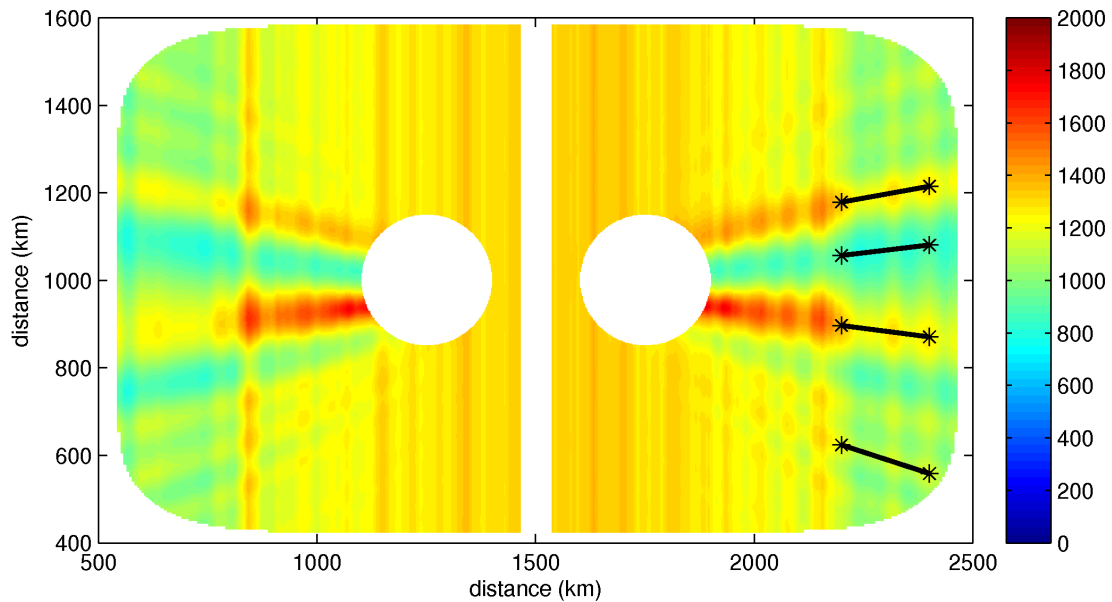
Figure 4.18: Baroclinic energy flux magnitude for the B2 run. L_E is 50 km and U_θ is 10 cm s^{-1}. Units are W m^{-1}.
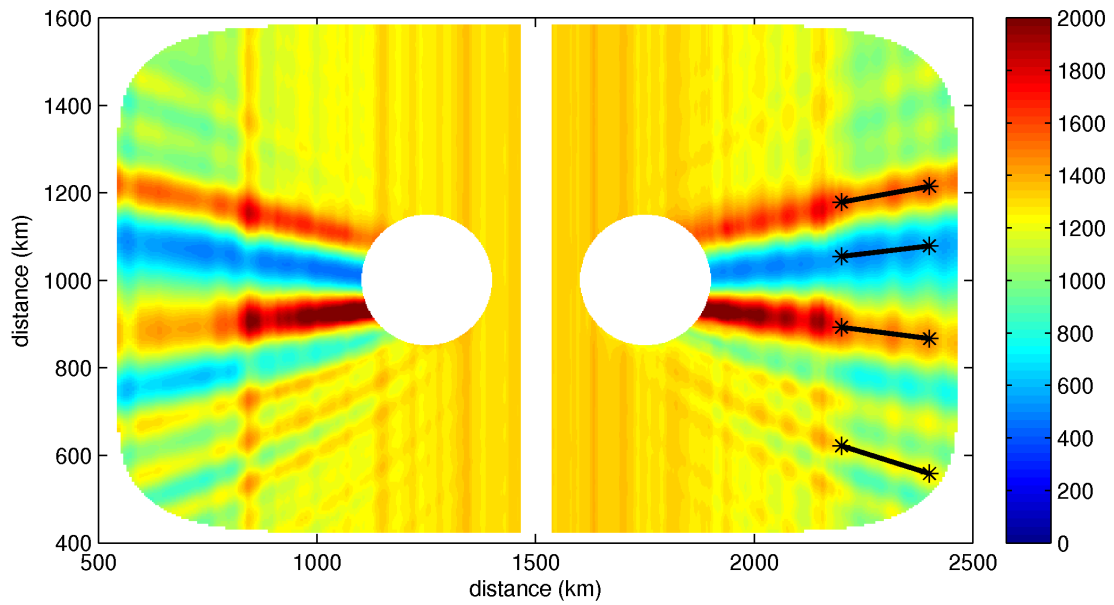
Figure 4.19: Baroclinic energy flux magnitude for the B3 run. L_E is 50 km and U_θ is 25 cm s^{-1}. Units are W m^{-1}.
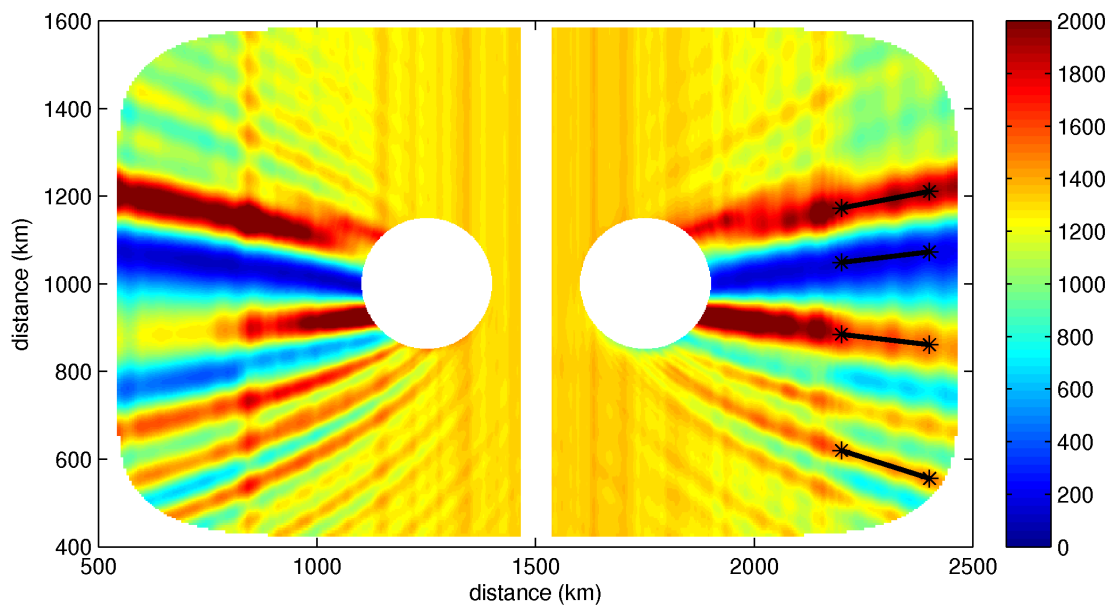
Figure 4.20: Baroclinic energy flux magnitude for the B4 run. L_E is 50 km and U_θ is 50 cm s^{-1}. Units are W m^{-1}.
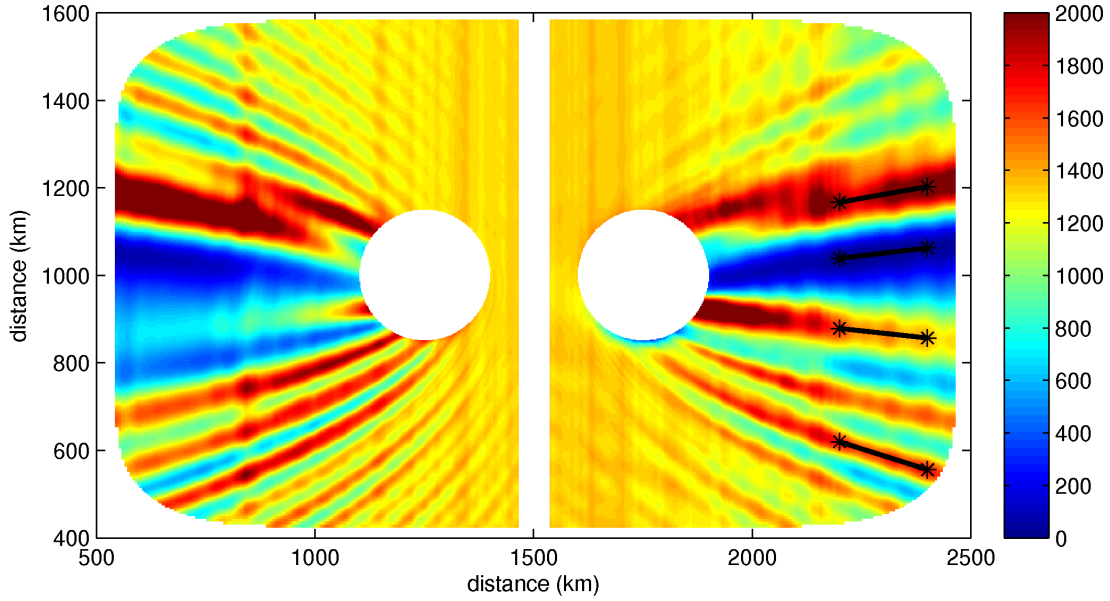
Figure 4.21: Baroclinic energy flux magnitude for the B5 run. L_E is 50 km and U_θ is 75 cm s^{-1}. Units are W m^{-1}.

Table 4.8: Intensification of energy flux in the focus/shadow beams for the "B" series of runs. The values here are the peaks/troughs of the curves in Figure 4.22. The reference values from the no eddy case are 1097 and 1149 W m^{-1} at 2200 and 2400 km, respectively.

| U_θ (cm s^{-1})	Distance (km)	Focus 1 (W m^{-1})	Shadow 1 (W m^{-1})	Focus 2 (W m^{-1})	Focus 3 (W m^{-1})
10	2200	1343	902	1361	1200
25	2200	1615	556	1600	1298
50	2200	1927	150	1757	1507
75	2200	1936	13	1627	1729
10	2400	1286	899	1268	1163
25	2400	1570	603	1450	1280
50	2400	1959	219	1535	1506
75	2400	2134	40	1383	1720

Figure 4.22: Magnitude of energy flux at 2200 km (top) and 2400 km (bottom) for the "B" series of runs. The solid vertical line indicates the centre of the eddy and the dashed vertical lines are drawn $2L_E$ away, roughly indicating the eddy size.

However, one of the effects of changing the density profile to contain a pycnocline is the beam angles have become almost invariant under varying azimuthal velocity. The maximum variation in the angles reported is 2.1 degrees, whereas in the linear case the angles varied almost 10 degrees. Looking at the intensification values we see that the shadow region drops almost to zero, similar to the linear case. However, the focusing regions do not double in intensity as they do in the linear case. This suggests that switching to the nonlinear density profile results in a smaller effect on the internal wave field.

Recall the cross section of the eddy velocity in Figures 4.9 and 4.10. In both cases the maximum velocity is at the surface and is zero at the bottom. The linear case has velocity that varies smoothly (cosine function) with depth and a substantial velocity is present halfway to the bottom and further. However, for the non-linear case, the interior the velocity is concentrated above the pycnocline (between 0 and 500 m depth). The relative quiescence of the eddy deeper than 500 m in the non-linear case may be responsible for reduced effect on the internal wave field when compared with the linear density profile.

4.3.3   Effect of eddy length scale

Comparing the "C" runs to the "A" runs with the same velocity shows a significant difference. The primary dissimilarity observed is that the eddies with the larger length scale had a much more dramatic effect on creating focusing and shadow regions; the smaller length scale had a much weaker effect. The eddy is smaller so a weaker effect results from the reduced area of internal waves that are subject to interaction. We again observe the emergence of a superposition of beams in the vicinity of the "primary" focusing beam.

4.3.4   Effect of barotropic tide

Comparing the "D" runs to the "A" runs shows that the effect of increasing the barotropic tide from 5 to 10 cm s^{-1} results in larger energy fluxes. This is attributed to the generation of stronger internal waves at the ridge. However, the interaction cases with the 10 and 25 cm s^{-1} eddies resulted in qualitatively the same result as the 5 cm s^{-1} barotropic tide in terms of beam angles and relative changes in energy flux intensity.

4.3.5   Effect of eddy direction

So far the analysis has been restricted to the anticyclonic eddies placed to the east of the ridge. A similar but cyclonic eddy has been placed to the west of the ridge for the purpose of comparing the effect of eddy spin direction. Qualitatively the effect of changing the effect of the eddy's direction of spin is only to change the

Figure 4.23: Baroclinic energy flux magnitude for the "C" runs. L_E is 25 km, U_θ is 25 cm s^{-1} (top) and 50 cm s^{-1} (bottom). Units are W m^{-1}.
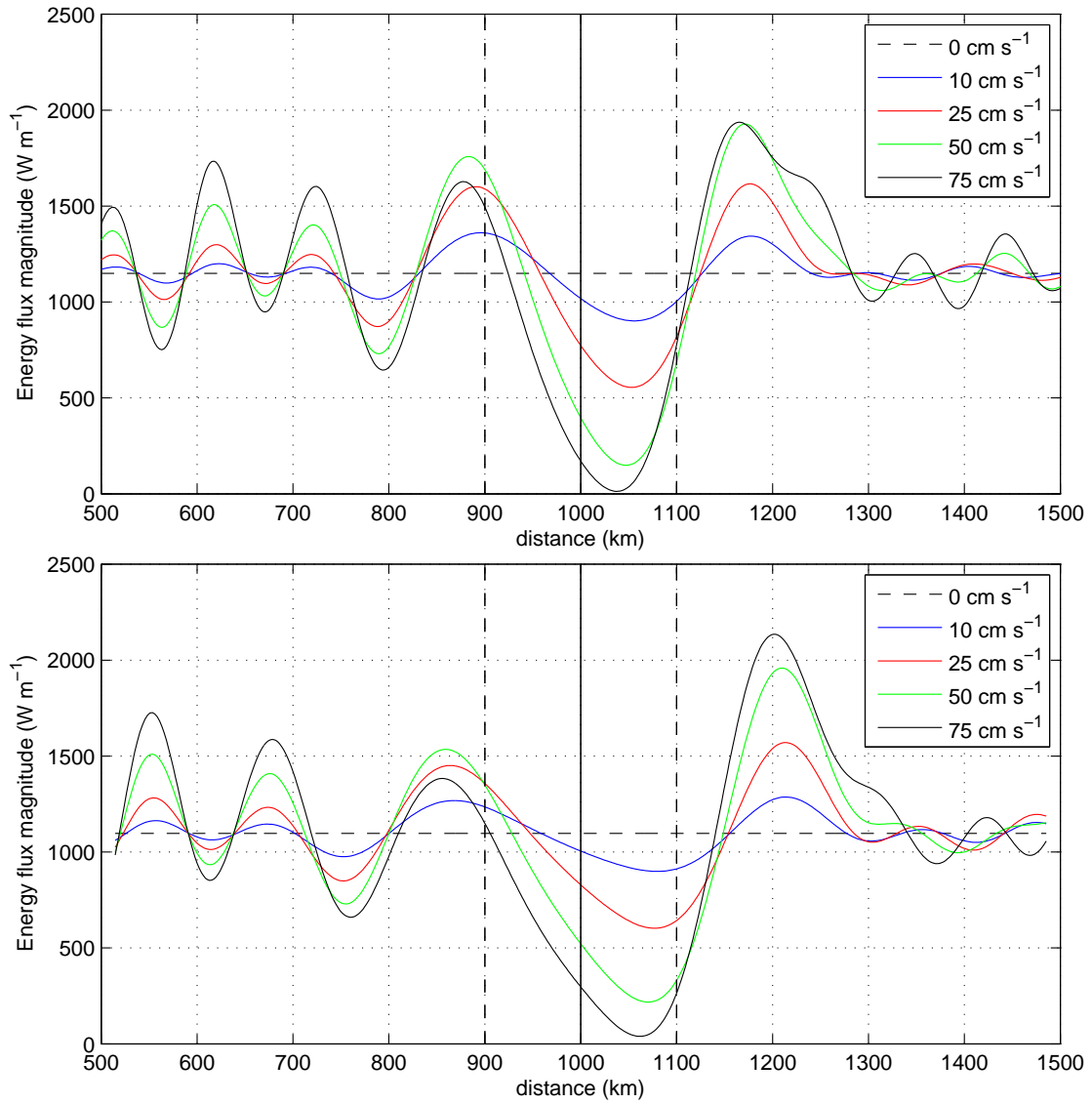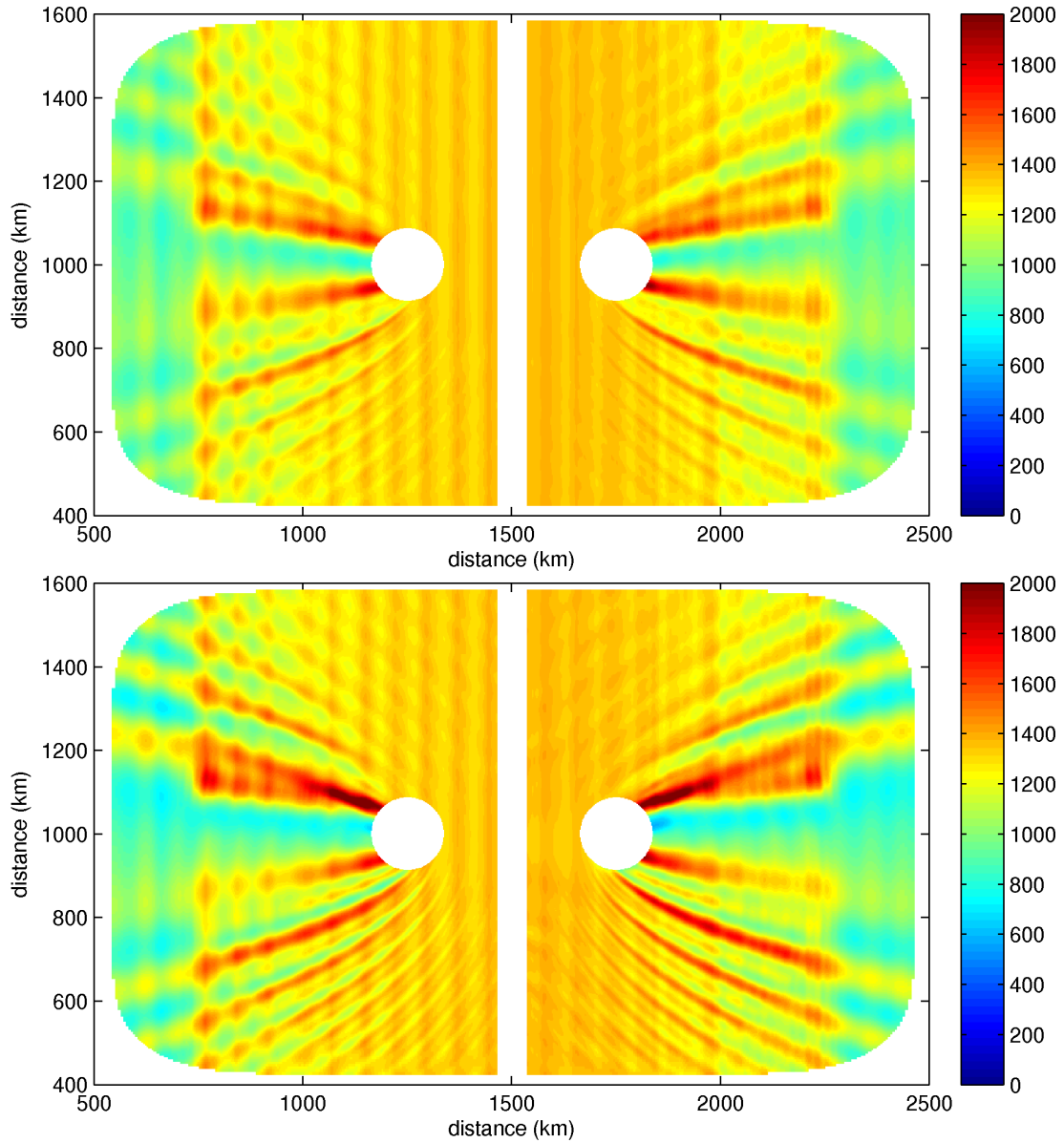
orientation of the formed beams. That is, if both eddies were anticyclonic the pattern of the beams would be symmetrical about $y = x$ instead of about $y = 0$. By visual inspection we see that the intensity of the beams compares well although small differences are visible. The asymmetry between cyclonic and anticyclonic eddies may explain the small differences in the the eddy flux magnitude features.

4.3.6 Vertical decomposition

A vertical decomposition into modes is applied to the velocity and density fields after 25 tidal periods have elapsed. Treating run A1 as the reference and looking at the modal breakdown of energy from the other "A" runs showed no significant energy transfer between modes. Variations on each mode were less than 1 percent compared to the reference case. However, there was some energy transferred from the zonal to the meridional velocity field, although the horizontal sum matches the reference case. The zonal to meridional exchange is explained by the fact that the direction of propagation has been modified somewhat in the wake of an eddy.

The results of the vertical decomposition provides $u_n(x, y)$ which, when plotted, gives some insight into the mechanism causing the focusing and shadow beams. The decomposition results from run A3 are used to plot $u_n(x, y)$ for the first 3 modes and are presented in Figures 4.24 through 4.26. The units of the colour scale are m s^{-1}, however, the large values are difficult to interpret in terms of the original flow field velocity. The orthogonality condition reduces the magnitude of the vertical mode structure functions $\phi_n(z)$ and the values of u_n are misleadingly large. This is not important in that we are seeking interference patterns and are not immediately concerned with the exactly values of u_n.

From the figures showing $u_n(x, y)$, we notice that directly in the wake of the eddies there is a substantial alteration of the otherwise y-independent pattern. Common to all three figures, in the vicinity of the "primary focusing beam", we see a constructive interference pattern. To the south of this is a destructive pattern. Moving even further south results in a band of alternating constructive and destructive interference patterns.

However, the intensity of the interference is not consistent between the three modes. The mode 1 waves are the least distorted by the eddy. Mode two shows a pattern most like the energy flux diagrams shown earlier in this section, as does mode 3. The interference pattern of mode 1 suggests a small contribution to the forming of the beams. Mode 2 is twice the amplitude of mode 3 so we expect that the contribution from mode 2 is most important in forming the beams.

The strength of the interference can be related to the group speed and wavelength of the waves. Mode 1 has the fastest group speed and the largest wavelength and spends the least time in the eddy. Thus its phase adjustment is small. Mode 2 has half the group speed and wavelength. From the interference pattern we see that its phase is adjusted substantially, causing strong interference contributing to the focusing/shadow regions. Mode 3 is similar to mode 2.

Figure 4.24: Zonal baroclinic velocity from run A3 projected onto mode 1 after 25 tidal periods. Units are m s^{-1}.

Figure 4.25: Zonal baroclinic velocity from run A3 projected onto mode 2 after 25 tidal periods. Units are m s^{-1}.

Figure 4.26: Zonal baroclinic velocity from run A3 projected onto mode 3 after 25 tidal periods. Units are m s^{-1}.

The run A1 is extended beyond 25 tidal periods to 100 tidal periods. The $u_n(x, y)$ is shown for modes 2 and 3 after 75 tidal periods in Figures 4.27 and 4.28 (mode 1 matches with Figure 4.24). The energy flux magnitude is shown after 75 tidal periods in Figure 4.29. These figures support the notion that interference patterns of the mode 2 waves dominates the formation of shadow/focusing regions with contributions from mode 1 and 3. Higher modes may also make a contribution to the focusing but are dwarfed in magnitude by the first three modes.
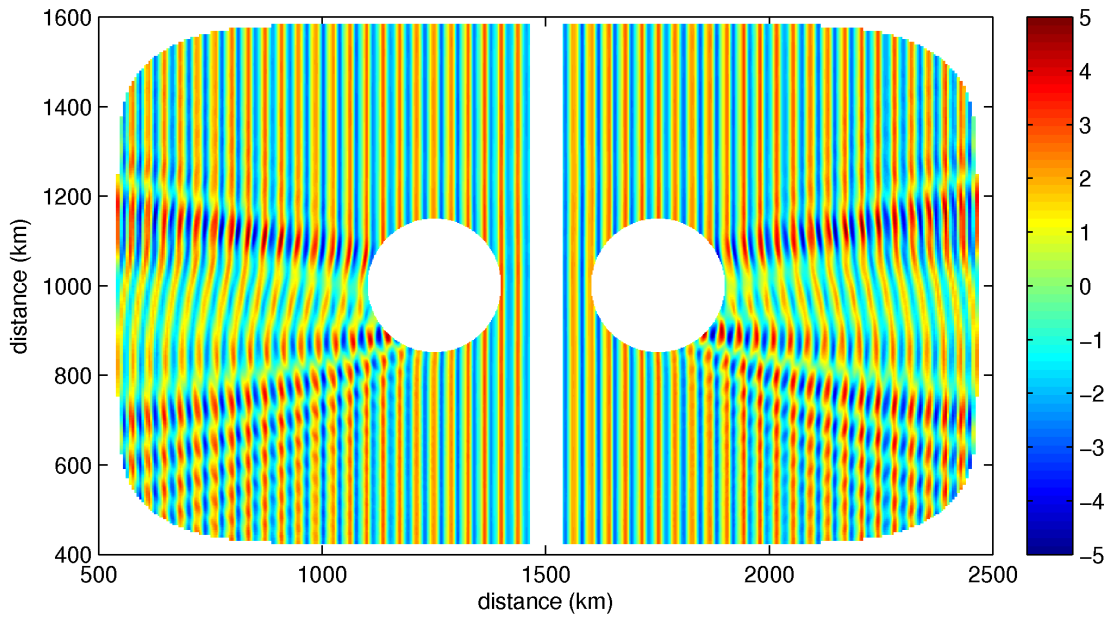
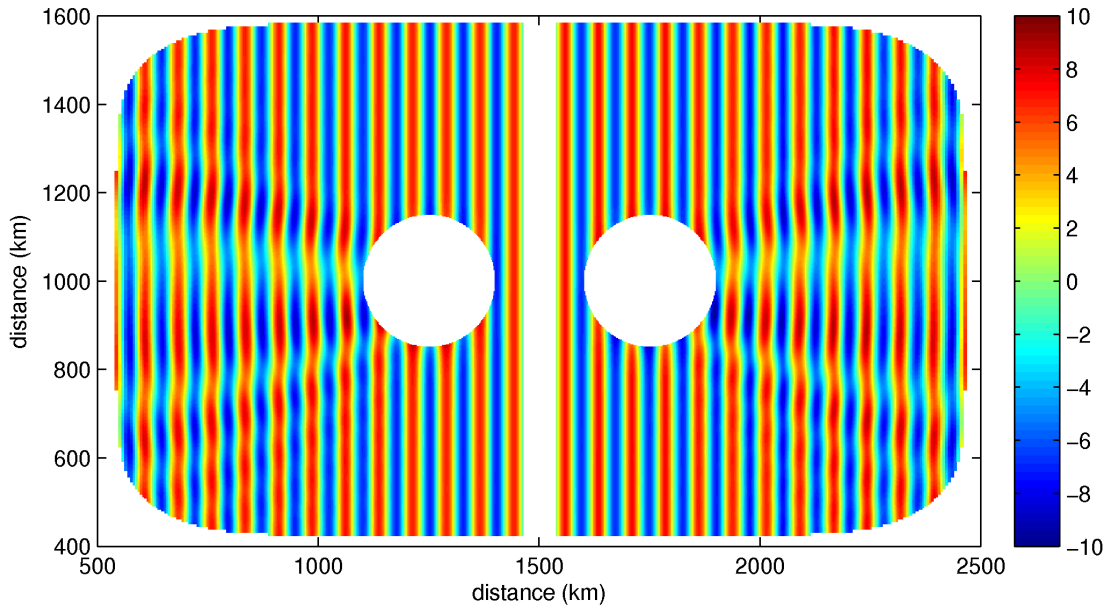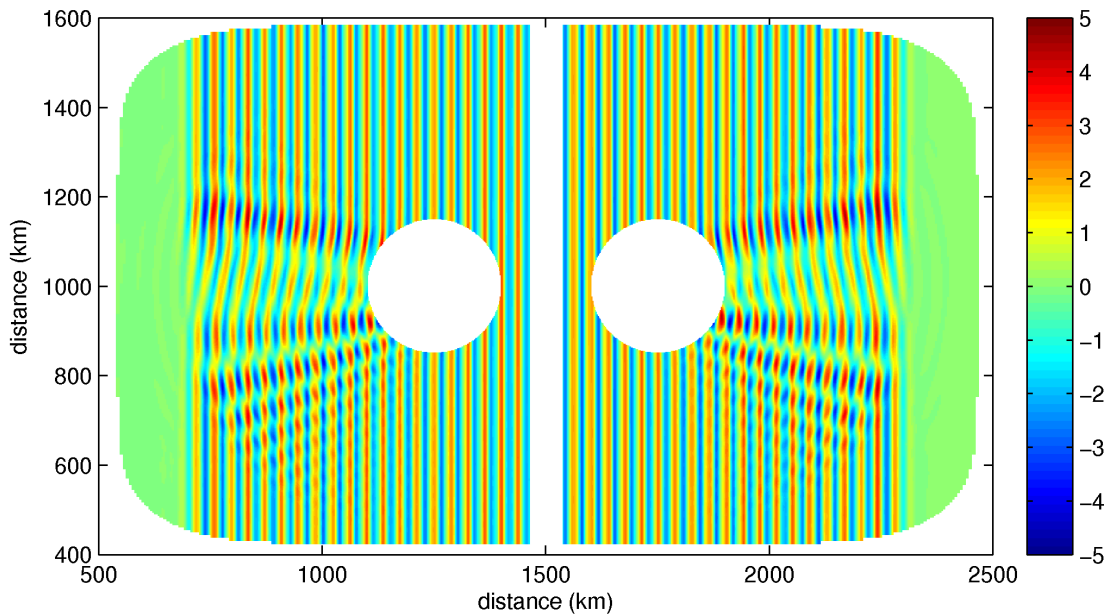Figure 4.27: Zonal baroclinic velocity from run A3 projected onto mode 2 after 75 tidal periods. Units are m s^{-1}.

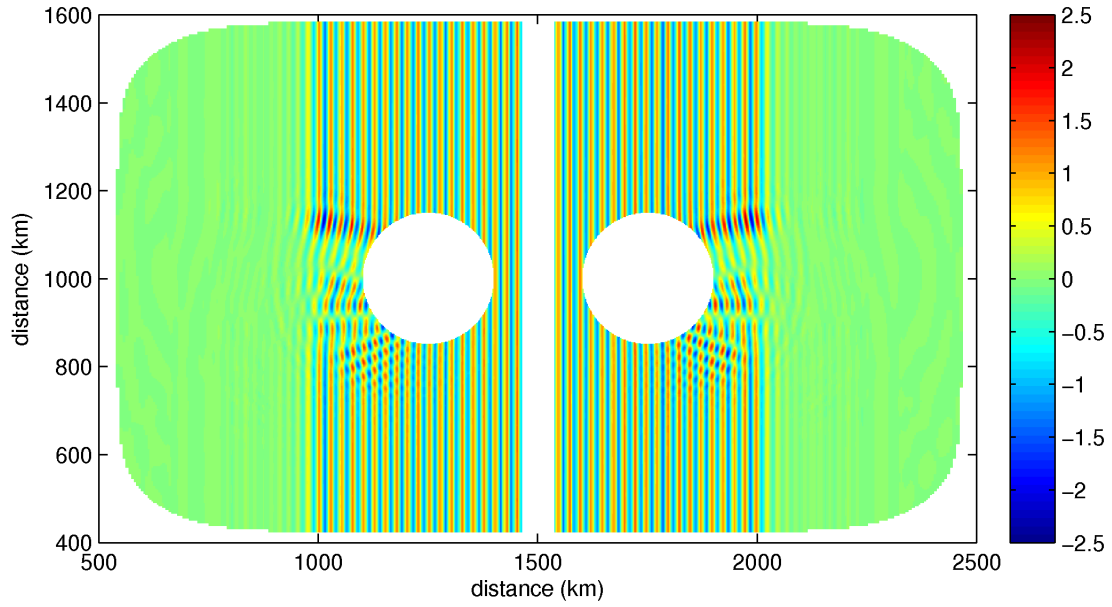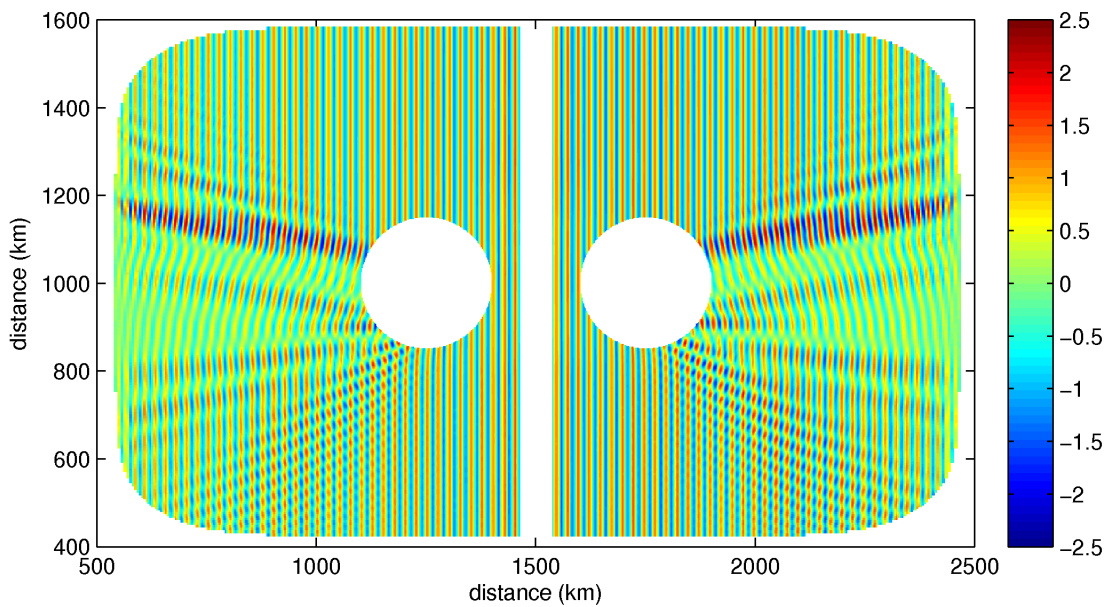Figure 4.28: Zonal baroclinic velocity from run A3 projected onto mode 3 after 75 tidal periods. Units are m s^{-1}.
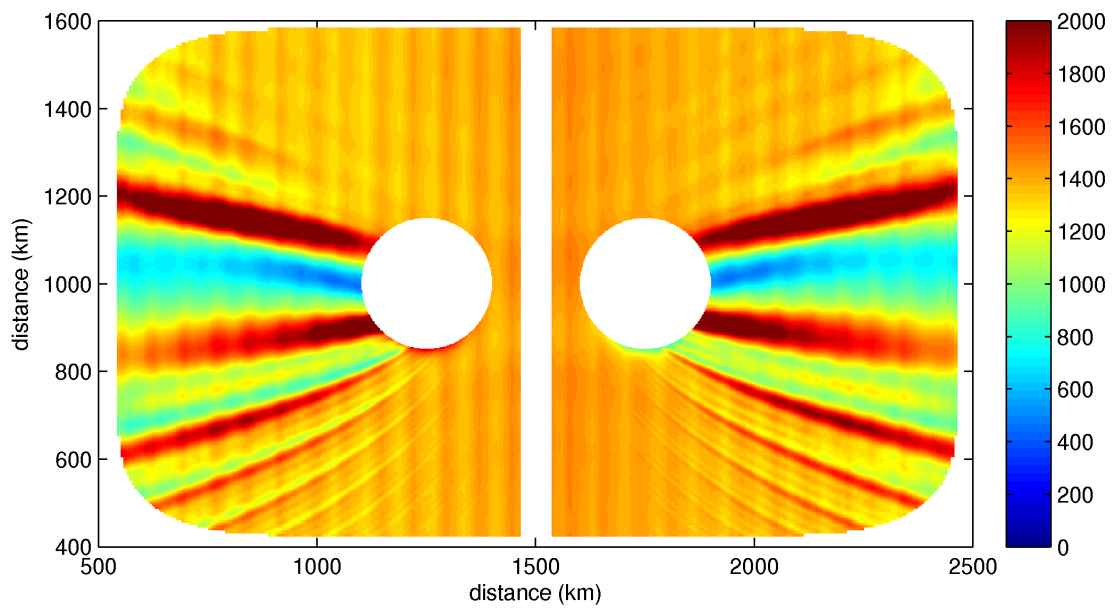
Figure 4.29: Baroclinic energy flux magnitude after 75 tidal periods for the A3 run. L_E is 50 km and U_θ is 25 cm s^{-1}. Units are W m^{-1}.

Chapter 5

Conclusion

The results from this thesis are shown, first for the internal wave configuration, then for the eddy configuration and finally for the interaction experiments.

5.1 Summary

Internal Gravity Waves

Internal waves were generated by flow over a Gaussian ridge and a comparison of the horizontal baroclinic and vertical velocities match well with analogue simulations performed by Dr. Lamb's IGW model. Differences are observed in energy flux magnitude; the MITgcm overestimates IGW by approximately 10 percent. The group velocity of internal waves produced by the MITgcm exceed the expectation from the analytical formula provided in the background section. This may partly explain the discrepancy in energy flux magnitude.

Eddies

Eddies are initialised and geostrophically adjusted. The excess sea-surface height that the model is initialised with is partly converted to kinetic energy because the adjusted eddies have larger magnitudes than they had at initialisation. This is consistent with geostrophic flow theory; excess potential energy is converted to kinetic as a system undergoes geostrophic adjustment. Gravity waves are also emitted as the eddy adjusts.

Eddy-wave interaction

The results from this thesis show that the effect of eddies on the internal wave field is primarily to cause beams of constructive and destructive interference in their wake.

No significant exchange of energy between modes was measured when comparing the energy levels of the internal wave field with and without an eddy. Some energy was transferred from the zonal component to the meridional component of horizontal velocity, however the sum remained the same at least to two decimal places.

The redirection of internal waves is of interest. The focusing and shadow zones that are formed beyond the eddy can fluctuate substantially in terms of energy flux magnitude. The energy flux in the shadow zones can be reduced to almost zero. In the focusing regions the energy flux magnitude can be doubled.

Decomposition of the horizontal flow field showed interference patterns that depended on the wave mode. Mode 1 was least affected by the eddy, and modes 2 and 3 were affected substantially. The beam patterns of interference coincides with the locations of the beams observed in the vertically integrated energy flux magnitude plots.

The regions of where intensification has happened may lead to increased interaction between internal waves. This may accelerate the cascade of energy to small scales. A more detailed is needed to determine the magnitude of this effect, if it is at all present.

5.2 Future work

Future work on the effects of mesoscale eddies on the internal wave field should consider the following issues:

- Use higher resolution to resolve higher mode waves,

- Longer simulations to allow higher mode waves to interact with the eddies,

- More than one eddy. For example, placing a second eddy in a focusing region may yield interesting interactions,

- Further optimise model parameters: tune or replace the Shapiro filter for dealing with grid scale noise, non-hydrostatic formulation, etc.,

- Resolve the reason for the above expected internal wave group velocities in the MITgcm,

- More model runs to further explore the parameter space,

- Use sub-mesoscale eddies as their length scale is more favourable for interaction.

APPENDICES

Appendix A

MATLAB M-files

A.1 Internal wave eigenvalue problem

This M-file implements the procedure described in Section 2.2.12 for finding the vertical structure of internal gravity waves of fixed frequency.

```matlab
function [PHI,LAMBDA,DPHI] = mdeigiw(modes,NZ,opts)
% Solve the eigenvalue problem for internal waves
% input: modes — number of modes to extract
%        NZ    — number of Chebyshev points to use
%        opts  — options struct for passing parameters
%                (which stratification, f, omega, etc)

H=opts.H; f=opts.f; wm2=opts.wm2; g=opts.g; RHO0=opts.RHO0;

% using Chebyshev from dmsuite
[z, Dz_zz] = chebdif(NZ, 2);
z=-0.5*(z'+1)*H;
Dz = Dz_zz(:,:,1);
Dzz = Dz_zz(:,:,2);

% Get N^2(z) profile
N2=(-g/RHO0)*drhobar(z,opts);

% Construct A & B matrices for generalised eigenvalue problem
A = Dzz;
%B = diag((N2 — wm2*wm2) / (wm2*wm2—f*f)); % nonhydrostatic
B = diag((N2) / (wm2*wm2—f*f));            % hydrostatic

% trim ends to enforce zero Dirichlet conditions
A=A(2:end-1,2:end-1);
B=B(2:end-1,2:end-1);

% now solve the eigenvalue problem
[V,EV]=eig(A,-B);
[evs ii]=sort((diag(EV)),'ascend');
```

```
31  efs = V(:,ii);
32
33  % extract first 'modes' modes
34  PHIcut = efs(:,1:modes);
35  LAMBDA = evs(1:modes);
36
37  % append zero endpoints
38  PHI=zeros(NZ,modes);
39  PHI(2:end-1,:)=PHIcut;
40
41  % compute DPHI as well
42  DPHI=Dz*PHI;
43
44  end
```

A.2   Quasigeostrophic eigenvalue problem

This M-file implements the procedure described in Section 2.3.1 for finding the mode 1 vertical structure of an eddy described by quasigeostrophic theory.

```
1   function [PHI,LAMBDA] = mdeig(mode,NZ,opts)
2   % Solve the eigenvalue problem for quasigeostrophy
3   % input: mode - which mode to extract
4   %        NZ   - number of Chebyshev points to use
5   %        opts - options struct for passing parameters
6   %               (which stratification, f, omega, etc)
7
8   H=opts.H; f=opts.f; g=opts.g; RHO0=opts.RHO0;
9
10  % using Chebyshev from dmsuite
11  [z, Dz_zz] = chebdif(NZ, 2);
12  z=-0.5*(z'+1)*H;
13  Dz = Dz_zz(:,:,1);
14
15  % Get N^2(z) profile
16  N2=(-g/RHO0)*drhobar(z,opts);
17
18  % Construct E matrix
19  EFULL = Dz*(diag(f*f./N2))*Dz;
20  E  = EFULL(2:end-1, 2:end-1);
21  E0 = EFULL(2:end-1, 1       );
22  EN = EFULL(2:end-1, end     );
23
24  % prepare eigenvalue problem with
25  % ends modified to enforce d/dz phi_n = 0
26  B0=[Dz(1,1) Dz(1,end); Dz(end,1) Dz(end,end)];
27  B1=[Dz(1,2:end-1) ; Dz(end,2:end-1)];
28
29  % Construct A matrix for MATLAB's eig function
30  A = E - [E0 EN]*inv(B0)*B1;
```

```
31
32  % now solve the eigenvalue problem
33  [V,EV]=eig(-A);
34  [evs ii]=sort((diag(EV)),'ascend');
35  efs = V(:,ii);
36
37  for n=1:NZ-2
38      % extract the current eigenvalue/eigenfunction
39      cev = evs(n); cef = efs(:,n);
40
41      % determine "mode" of this eigenfunction by zero crossings
42      nzc=nnz(sign(cef(2:end))-sign(cef(1:end-1)));
43
44      % export desired mode
45      if nzc == mode
46          % compute the endpoints and append them
47          p0pN = -inv(B0)*B1*cef;
48          phi = [p0pN(1); cef; p0pN(end)];
49
50          % let the first point be positive
51          PHI = phi ./sign(phi(end));
52
53          % return the eigenvalue also
54          LAMBDA=cev;
55
56          % quit after we've found the desired mode
57          return
58      end
59  end
60  end
```

A.3   Grid spacing

This M-file produces a grid spacing by following the method described in Section 3.3.

```
1   function [x, dx] = getres(nx, L, dxmin, frac, smth, dispflag)
2   % Determines the variable grid spacing given a few parameters
3   % L = length of dimension
4   % dxmin = desired dx at the centre of the domain
5   % frac = fraction of the domain requested at low resolution (0.5)
6   % smth = how smooth/sharply to transition between resolutions (20)
7   % dispflag = flag to turn on plotting the prodecure as it goes
8
9   if nargin == 2
10      fprintf('Using fixed resolution: L=%.0f km, n=%d\n',L/1e3,nx);
11      dx=(L/nx)*ones(1,nx);
12  else
13      fprintf('Using variable resolution: L=%.0f km, n=%d, ', ...
14                  L/1e3,nx);
```

```matlab
     fprintf('dxmin=%.1f km, frac=%.3f, smth=%.1f\n', ...
             dxmin/1e3,frac,smth);
     A = smth; B = frac; C = dxmin;
     D = (L/nx -C) / (1-B); % rough estimate for D

     x=linspace(0,L,nx);
     dx=C + D*0.5*(2 + tanh(A*(x/L - 1/2 - B/2)) - ...
                       tanh(A*(x/L - 1/2 + B/2)));

     flag=1; scal=1e20; npass=0;
     while(flag)
         npass=npass+1;
         if abs(abs(scal)-1) < 1e-5
             if abs(sum(dx) -L) < 1e-8
                 flag=0;
             end
         end
         if npass>1e4
             disp('problem: npass>1e4');
             disp('did not converge, consider using more points');
             return;
         end
         scal = (L) / sum(dx);
         scal = (scal -1)/10 + 1; % don't scale too much per iter
         scal = min(scal,1.01); scal=max(0.99,scal); % 1% change max
         D=D*scal;

         dx=C + D*0.5*(2 + tanh(A*(x/L - 1/2 - B/2)) - ...
                           tanh(A*(x/L - 1/2 + B/2)));
         x = cumsum([dx(1)/2 0.5*(dx(1:end-1)+dx(2:end))]);

         if (D < 0.1*dxmin)
             disp('problem: D<dxmin: need fewer points');
             return;
         end
         if (D > L)
             disp('problem: D>L: need more points');
             return;
         end

         if(dispflag)
             clf;
             subplot(2,1,1); plot(x,dx,'b',x,dx*L/sum(dx),'k')
             subplot(2,1,2); semilogy(x,abs((dx - dx*L/sum(dx))))
             drawnow
         end
     end
     fprintf('scal=%.5f, D=%.3f, npass=%d\n',scal,D,npass);
end
fprintf('--> min dx: %.3f km, max dx: %.3f km', ...
         min(dx)/1e3,max(dx)/1e3);
fprintf('--> sum(dx) = %.10f\n',sum(dx));
x = cumsum([dx(1)/2 0.5*(dx(1:end-1)+dx(2:end))]);
end
```

Appendix B

MITgcm input files

This appendix shows the namelist input files used with the MITgcm for the internal wave-eddy simulations. The input files for the other configurations are similar and are not reproduced here.

Main MITgcm parameters file `data`:

```
# ====================
# | Model parameters |
# ====================
#
# Continuous equation parameters
 &PARM01
 tRefFile='MD.tRef',
 sRefFile='MD.sRef',
 viscAz=0.E-4,
 viscAh=0.E2,
 viscAhMax=0.E2,
 no_slip_sides=.FALSE.,
 no_slip_bottom=.FALSE.,
 viscA4=0.E9,
 viscA4Max=0.E9,
 diffKhT=0.E3,
 diffKzT=0.E-5,
 diffKhS=0.E3,
 diffKzS=0.E-5,
 f0=0.5e-4,
 beta=0.E-11,
 useConstantF=.TRUE.,
 tAlpha=1.7E-4,
 sBeta =7.6E-4,
 gravity=9.81,
 gBaro=9.81,
```

```
 rhoConstFresh=1028.0,
 rhoConst=1028.0,
 rhoNil=1028.0,
 rigidLid=.FALSE.,
 implicitFreeSurface=.TRUE.,
 nonlinFreeSurf=0,
 exactConserv=.TRUE.,
 vectorInvariantMomentum=.TRUE.,
 tempStepping=.FALSE.,
 momViscosity=.FALSE.,
 momForcing=.FALSE.,
 eosType='LINEAR',
 hFacMin=0.25,
 nonHydrostatic=.FALSE.,
 readBinaryPrec=64,
 saltAdvScheme=4,
 tempAdvScheme=4,
#- not safe to use globalFiles in multi-processors runs
#globalFiles=.TRUE.,
 &

# Elliptic solver parameters
 &PARM02
 cg2dMaxIters=1000,
 cg2dTargetResidual=1.E-13,
 cg3dMaxIters=400,
 cg3dTargetResidual=1.E-13,
 &

# Time stepping parameters
 &PARM03
 niter0=0,
 nTimeSteps=10801,
 deltaT=103.5,
 abEps=0.1,
 pChkptFreq=0.0,
 chkptFreq=0.0,
 dumpFreq=22356.0,
 monitorFreq=2484.0,
 writePickupAtEnd=.TRUE.,
 &

# Gridding parameters
 &PARM04
 usingCartesianGrid=.TRUE.,
```

```
usingSphericalPolarGrid=.FALSE.,
delXfile='MD.dx',
delYfile='MD.dy',
delRfile='MD.dr',
 &

# Input datasets
 &PARM05
bathyFile='MD.topo',
hydrogSaltFile='MD.S.init',
hydrogThetaFile='MD.T.init',
uVelInitFile='MD.U.init',
vVelInitFile='MD.V.init',
pSurfInitFile='MD.eta.init',
 &
```

Open boundaries parameter file `data.obcs`:

```
# Open-boundaries
 &OBCS_PARM01
OB_AMPL=5.0d-2,
OB_OMEGA=1.405257046694307d-04,
OB_RAMP=.FALSE.,
OB_Ieast=540*-1,
OB_Iwest=540*1,
useOBCSsponge=.FALSE.,
 &
```

Shapiro filter parameter file `data.shap`:

```
# Shapiro Filter parameters
 &SHAP_PARM01
shap_filt_uvStar=.FALSE.,
shap_filt_TrStagg=.FALSE.,
Shap_funct=2,
nShapT=2,
nShapUV=2,
nShapTrPhys=0,
nShapUVPhys=0,
Shap_Trtau=22356.,
Shap_uvtau=22356.,
 &
```

MYPACKAGE parameter file `data.mypackage`:

```
&MYPACKAGE_PARM01
    myPa_N0 = 1e-3,
    myPa_T0 = 10.,
    myPa_S0 = 35.,
    myPa_RHOBAR = 1,
    myPa_U0File = 'MD.U.init',
    myPa_V0File = 'MD.V.init',
&
```

Appendix C

MITgcm FORTRAN modifications

C.1   OBCS boundary conditions

This file, `obcs_calc.F`, implements the boundary conditions to force a barotropic tide at the west boundary and a radiation condition at the east boundary. Some irrelevant code is omitted for brevity.

```fortran
1  #include "OBCS_OPTIONS.h"
2
3        SUBROUTINE OBCS_CALC( bi, bj, futureTime, futureIter,
4       &                      uVel, vVel, wVel, theta, salt, etaN,
5       &                      myThid )
6  C     |==============================================================|
7  C     | SUBROUTINE OBCS_CALC                                         |
8  C     | o Calculate future boundary data at open boundaries          |
9  C     |   at time = futureTime                                       |
10 C     |==============================================================|
11 C     |                                                              |
12 C     |==============================================================|
13        IMPLICIT NONE
14
15 C     === Global variables ===
16 #include "SIZE.h"
17 #include "EEPARAMS.h"
18 #include "PARAMS.h"
19 #include "GRID.h"
20 #include "OBCS.h"
21 #ifdef ALLOW_PTRACERS
22 #include "PTRACERS_SIZE.h"
23 #include "PTRACERS_PARAMS.h"
24 #include "PTRACERS_FIELDS.h"
25 #include "OBCS_PTRACERS.h"
26 #endif /* ALLOW_PTRACERS */
```

```
27
28  C       == Routine arguments ==
29        INTEGER bi, bj
30        INTEGER futureIter
31        _RL futureTime
32        _RL uVel (1—OLx:sNx+OLx,1—OLy:sNy+OLy,Nr,nSx,nSy)
33        _RL vVel (1—OLx:sNx+OLx,1—OLy:sNy+OLy,Nr,nSx,nSy)
34        _RL wVel (1—OLx:sNx+OLx,1—OLy:sNy+OLy,Nr,nSx,nSy)
35        _RL theta(1—OLx:sNx+OLx,1—OLy:sNy+OLy,Nr,nSx,nSy)
36        _RL salt (1—OLx:sNx+OLx,1—OLy:sNy+OLy,Nr,nSx,nSy)
37        _RL etaN (1—OLx:sNx+OLx,1—OLy:sNy+OLy,nSx,nSy)
38        INTEGER myThid
39
40  #ifdef ALLOW_OBCS
41
42  C       == Local variables ==
43  C       I,J,K        — loop indices
44  C       I_obc, J_obc — local index of open boundary
45  C       msgBuf       — Informational/error meesage buffer
46  C       zomega, zampl — frequency and magnitude of tide
47  C       zomega2, zc, zH, zeta0, zf, zeta — temp variables
48        INTEGER I, J , K, I_obc, J_obc
49        CHARACTER*(MAX_LEN_MBUF) msgBuf
50        _RL zomega, zampl
51        _RL zomega2, zc, zH, zf, zeta0, zeta, zramp
52
53  C       ! constants: set them in data.obcs
54        zomega = OB_OMEGA
55        zampl = OB_AMPL
56
57        zomega2 = zomega*zomega
58        zH = abs(rF(Nr+1))
59        IF (OB_RAMP) THEN
60          IF( futureTime .lt. 0.5*PI/zomega ) THEN
61            zramp = 0.5*(1 — cos(2*zomega*futureTime))
62          ELSE
63            zramp = 1. d 0
64          ENDIF
65        ELSE
66          zramp = 1. d 0
67        ENDIF
68
69  #ifdef ALLOW_OBCS_BALANCE
70        _RL Tr_T, Ar_T, Tr, Ar
71  #endif /* ALLOW_OBCS_BALANCE */
72  #ifdef ALLOW_PTRACERS
73        INTEGER iTracer
74  #endif /* ALLOW_PTRACERS */
75
76
77  #ifdef ALLOW_DEBUG
78        IF ( debugLevel .GE. debLevB )
79     &        CALL DEBUG_ENTER('OBCS_CALC',myThid)
80  #endif
```

```
81
82  #ifdef ALLOW_OBCS_EAST
83  C      Eastern OB
84  #ifdef ALLOW_DEBUG
85        IF ( debugLevel .GE. debLevB )
86       &     CALL DEBUG_MSG('OBCS_CALC: East',myThid)
87  #endif
88        IF (useOrlanskiEast) THEN
89  #ifdef ALLOW_ORLANSKI
90          CALL ORLANSKI_EAST(
91       &          bi, bj, futureTime,
92       &          uVel, vVel, wVel, theta, salt,
93       &          myThid )
94  #endif
95        ELSE
96          DO K=1,Nr
97            DO J=1-Oly,sNy+Oly
98              I_obc=OB_Ie(J,bi,bj)
99              IF (I_obc.ne.0) THEN
100               zf = fCori(I_obc,J,bi,bj)
101               zc = sqrt(gravity*zH*zomega2/(zomega2-zf*zf))
102               OBEu(J,K,bi,bj)=(zc/zH)*etaN(I_obc-1,J,bi,bj)
103               OBEv(J,K,bi,bj)=0.
104               OBEt(J,K,bi,bj)=tRef(K)
105               OBEs(J,K,bi,bj)=sRef(K)
106  #ifdef ALLOW_NONHYDROSTATIC
107               OBEw(J,K,bi,bj)=0.
108  #endif
109  #ifdef NONLIN_FRSURF
110               OBEeta(J,bi,bj)=0.
111  #endif
112              ENDIF
113            ENDDO
114          ENDDO
115        ENDIF
116  #endif /* ALLOW_OBCS_EAST */
117
118  C ————————————————————————————————————————————
119
120  #ifdef ALLOW_OBCS_WEST
121  C      Western OB
122  #ifdef ALLOW_DEBUG
123        IF ( debugLevel .GE. debLevB )
124       &     CALL DEBUG_MSG('OBCS_CALC: West',myThid)
125  #endif
126        IF (useOrlanskiWest) THEN
127  #ifdef ALLOW_ORLANSKI
128          CALL ORLANSKI_WEST(
129       &          bi, bj, futureTime,
130       &          uVel, vVel, wVel, theta, salt,
131       &          myThid )
132  #endif
133        ELSE
134          DO K=1,Nr
```

```
135            DO J=1-Oly,sNy+Oly
136               I_obc=OB_Iw(J,bi,bj)
137               IF (I_obc.ne.0) THEN
138                 zf = fCori(I_obc,J,bi,bj)
139                 zc = sqrt(gravity*zH*zomega2/(zomega2-zf*zf))
140                 zeta0 = zramp * zampl * (zH/zc)
141                 zeta = etaN(I_obc,J,bi,bj)
142                 OBWu(J,K,bi,bj)=-(zc/zH)*
143      &                  (zeta - zeta0*sin(zomega*futureTime))
144                 OBWv(J,K,bi,bj)=0.
145                 OBWt(J,K,bi,bj)=tRef(K)
146                 OBWs(J,K,bi,bj)=sRef(K)
147 #ifdef ALLOW_NONHYDROSTATIC
148                 OBWw(J,K,bi,bj)=0.
149 #endif
150 #ifdef NONLIN_FRSURF
151                 OBWeta(J,bi,bj)=0.
152 #endif
153               ENDIF
154             ENDDO
155           ENDDO
156         ENDIF
157 #endif /* ALLOW_OBCS_WEST */
158
159 C ————————————————————————————————————————————————————————————
160
161 #ifdef ALLOW_OBCS_NORTH
162 C        Northern OB
163 #ifdef ALLOW_DEBUG
164       IF ( debugLevel .GE. debLevB )
165      &      CALL DEBUG_MSG('OBCS_CALC: North',myThid)
166 #endif
167       IF (useOrlanskiNorth) THEN
168 #ifdef ALLOW_ORLANSKI
169         CALL ORLANSKI_NORTH(
170      &          bi, bj, futureTime,
171      &          uVel, vVel, wVel, theta, salt,
172      &          myThid )
173 #endif
174       ELSE
175         DO K=1,Nr
176           DO I=1-Olx,sNx+Olx
177             J_obc=OB_Jn(I,bi,bj)
178             IF (J_obc.ne.0) THEN
179               OBNv(I,K,bi,bj)=0.
180               OBNu(I,K,bi,bj)=0.
181               OBNt(I,K,bi,bj)=tRef(K)
182               OBNs(I,K,bi,bj)=sRef(K)
183 #ifdef ALLOW_NONHYDROSTATIC
184               OBNw(I,K,bi,bj)=0.
185 #endif
186 #ifdef NONLIN_FRSURF
187               OBNeta(I,bi,bj)=0.
188 #endif
```

```
189              ENDIF
190            ENDDO
191          ENDDO
192        ENDIF
193 #endif /* ALLOW_OBCS_NORTH */
194
195 C ─────────────────────────────────────────────────────────────
196
197 #ifdef ALLOW_OBCS_SOUTH
198 C          Southern OB
199 #ifdef ALLOW_DEBUG
200        IF ( debugLevel .GE. debLevB )
201      &      CALL DEBUG_MSG('OBCS_CALC: South',myThid)
202 #endif
203        IF (useOrlanskiSouth) THEN
204 #ifdef ALLOW_ORLANSKI
205          CALL ORLANSKI_SOUTH(
206      &          bi, bj, futureTime,
207      &          uVel, vVel, wVel, theta, salt,
208      &          myThid )
209 #endif
210        ELSE
211          DO K=1,Nr
212            DO I=1-Olx,sNx+Olx
213              J_obc=OB_Js(I,bi,bj)
214              IF (J_obc.ne.0) THEN
215                OBSu(I,K,bi,bj)=0.
216                OBSv(I,K,bi,bj)=0.
217                OBSt(I,K,bi,bj)=tRef(K)
218                OBSs(I,K,bi,bj)=sRef(K)
219 #ifdef ALLOW_NONHYDROSTATIC
220                OBSw(I,K,bi,bj)=0.
221 #endif
222 #ifdef NONLIN_FRSURF
223                OBSeta(I,bi,bj)=0.
224 #endif
225              ENDIF
226            ENDDO
227          ENDDO
228        ENDIF
229 #endif /* ALLOW_OBCS_SOUTH */
230
231 #ifdef ALLOW_PTRACERS
232 *** UNUSED CODE NOT REPRODUCED FOR THIS APPENDIX ***
233 #endif /* ALLOW_PTRACERS */
234
235 #ifdef ALLOW_OBCS_PRESCRIBE
236 *** UNUSED CODE NOT REPRODUCED FOR THIS APPENDIX ***
237 #endif /* ALLOW_OBCS_PRESCRIBE */
238
239 #ifdef ALLOW_OBCS_BALANCE
240 *** UNUSED CODE NOT REPRODUCED FOR THIS APPENDIX ***
241 #endif /* ALLOW_OBCS_BALANCE */
242
```

```
243  #endif /* ALLOW_OBCS */
244
245  #ifdef ALLOW_DEBUG
246        IF ( debugLevel .GE. debLevB )
247     &       CALL DEBUG_LEAVE('OBCS_CALC',myThid)
248  #endif
249        RETURN
250        END
```

C.2   MYPACKAGE density profiles

This file, `mypackage_rhobar.F`, implements the two density profiles described in Section 3.1.

```
1  #include "MYPACKAGE_OPTIONS.h"
2
3        _RL FUNCTION MYPACKAGE_RHOBAR(z)
4  C     !DESCRIPTION:
5  C     Function for rhobar, customised for eddy—internal wave
        experiments.
6
7  C     !USES:
8        IMPLICIT NONE
9  #include "SIZE.h"
10 #include "EEPARAMS.h"
11 #include "PARAMS.h"
12 #ifdef ALLOW_MYPACKAGE
13 #include "MYPACKAGE.h"
14 #endif
15
16 C     == Global variables ==
17 #include "GRID.h"
18 #include "EOS.h"
19
20 C     !INPUT PARAMETERS:
21 C     z    :: depth ( m )
22       _RL    z
23
24 #ifdef ALLOW_MYPACKAGE
25 C     !LOCAL VARIABLES:
26 C              ! rhobar1
27       _RL    zgammat, zgammas
28 C              ! rhobar2
29       _RL    A, B, H, DRHO
30
31       IF ( myPa_RHOBAR .EQ. 1 ) THEN
32         zgammas = (myPa_N0*myPa_N0)/(−sBeta*gravity);
33         zgammat = 0;
34         MYPACKAGE_RHOBAR = rhoConst *
35     &              (1 − tAlpha*(zgammat*z) + sBeta*(zgammas*z))
```

```
36
37         ELSEIF ( myPa_RHOBAR .EQ. 2 ) THEN
38            A=50
39            B=400
40            DRHO=1
41       H=-rF(Nr+1)
42
43            MYPACKAGE_RHOBAR = rhoConst*(1 -myPa_N0*myPa_N0*z/gravity
44      &                        + (DRHO/rhoConst)*0.5*(1 - tanh(A*(z+B)/H)))
45         ENDIF
46  #endif /* ALLOW_MYPACKAGE */
47         RETURN
48         END
```

C.3   MYPACKAGE energy flux computations

This file, `mypackage_diagnostics_state.F`, implements the online computation of depth-integrated energy flux. Kinetic and potential energy is also computed but it is not used.

```
1   #include "MYPACKAGE_OPTIONS.h"
2
3   CBOP 0
4   C !ROUTINE: MYPACKAGE_DIAGNOSTICS_STATE
5
6   C !INTERFACE:
7         SUBROUTINE MYPACKAGE_DIAGNOSTICS_STATE(
8      I                        myTime, myIter, myThid )
9
10  C     !DESCRIPTION:
11  C     Compute kinetic, potential energies
12  C     Compute energy flux
13
14  C     !USES:
15        IMPLICIT NONE
16  #include "SIZE.h"
17  #include "EEPARAMS.h"
18  #include "PARAMS.h"
19  #ifdef ALLOW_MYPACKAGE
20  #include "MYPACKAGE.h"
21  #endif
22
23  C     == Global variables ==
24  #include "GRID.h"
25  #include "DYNVARS.h"
26  #include "RESTART.h"
27  #include "SURFACE.h"
28  #include "EOS.h"
29
30  C     !INPUT PARAMETERS:
```

```fortran
31 C       myTime   :: Current time of simulation ( s )
32 C       myIter   :: Current iteration number in simulation
33 C       myThid   :: my Thread Id number
34       _RL      myTime
35       INTEGER myIter, myThid
36 CEOP
37
38 #ifdef ALLOW_MYPACKAGE
39 C       !LOCAL VARIABLES:
40       INTEGER I,J,K,bi,bj
41       _RL MYPACKAGE_RHOBAR
42       EXTERNAL MYPACKAGE_RHOBAR
43
44 #ifdef MYPACKAGE_ENERGY
45       _RL keuprime (1—OLx:sNx+OLx,1—OLy:sNy+OLy,Nr,nSx,nSy)
46       _RL keubar   (1—OLx:sNx+OLx,1—OLy:sNy+OLy,Nr,nSx,nSy)
47       _RL petmp    (1—OLx:sNx+OLx,1—OLy:sNy+OLy,Nr,nSx,nSy)
48
49       _RL rhotmp   (1—OLx:sNx+OLx,1—OLy:sNy+OLy,Nr,nSx,nSy)
50
51       _RL ubc   (1—OLx:sNx+OLx,1—OLy:sNy+OLy,Nr,nSx,nSy)
52       _RL wu    (1—OLx:sNx+OLx,1—OLy:sNy+OLy,Nr,nSx,nSy)
53       _RL swu   (1—OLx:sNx+OLx,1—OLy:sNy+OLy,nSx,nSy)
54       _RL ubt   (1—OLx:sNx+OLx,1—OLy:sNy+OLy,nSx,nSy)
55
56       _RL vbc   (1—OLx:sNx+OLx,1—OLy:sNy+OLy,Nr,nSx,nSy)
57       _RL wv    (1—OLx:sNx+OLx,1—OLy:sNy+OLy,Nr,nSx,nSy)
58       _RL swv   (1—OLx:sNx+OLx,1—OLy:sNy+OLy,nSx,nSy)
59       _RL vbt   (1—OLx:sNx+OLx,1—OLy:sNy+OLy,nSx,nSy)
60
61       _RL pint  (1—OLx:sNx+OLx,1—OLy:sNy+OLy,Nr,nSx,nSy)
62
63       _RL efu2d (1—OLx:sNx+OLx,1—OLy:sNy+OLy,nSx,nSy)
64       _RL efv2d (1—OLx:sNx+OLx,1—OLy:sNy+OLy,nSx,nSy)
65
66       _RL za, etaupt, zubcc, etavpt, zvbcc
67       _RL zrho, zrhobarzme, zdzpe, zzme, zp
68       _RL zgammas, zgammat
69
70 #endif /* MYPACKAGE_ENERGY */
71
72 #ifdef ALLOW_DIAGNOSTICS
73       IF ( useDiagnostics ) THEN
74
75 #ifdef MYPACKAGE_ENERGY
76
77 C       MAIN LOOP OVER BI,BJ
78       DO bj=myByLo(myThid),myByHi(myThid)
79        DO bi=myBxLo(myThid),myBxHi(myThid)
80
81
82 C        Compute rho and potential energy; rho stored as it's used
     later
83          DO K=1,Nr
```

```
84            DO J=1-OLy,sNy+OLy
85              DO I=1-OLx,sNx+OLx
86                rhotmp(I,J,K,bi,bj) = rhoConst *
87       I              (1 - tAlpha*(theta(I,J,K,bi,bj)-myPa_T0)
88       I                + sBeta*( salt(I,J,K,bi,bj)-myPa_S0))
89                petmp(I,J,K,bi,bj) = gravity*rhotmp(I,J,K,bi,bj)*rC(K)
90              ENDDO
91            ENDDO
92          ENDDO
93
94  C      Find kinetic energies: 0.5*rho*u^2
95        DO K=1,Nr
96          DO J=1-OLy,sNy+OLy-1
97            DO I=1-OLx,sNx+OLx-1
98  C              Borrowing KEscheme=3 from mom_calc_ke.F
99                keuprime(I,J,K,bi,bj) = rhotmp(I,J,K,bi,bj)*0.25*(
100      &              (
101      &          uVel(I  ,J,K,bi,bj)
102      &              *(uVel(I  ,J,K,bi,bj)-myPa_U0(I  ,J,K,bi,bj))
103      &              *_hFacW(I ,J, K,bi,bj)*rAw(I ,J, bi,bj)
104      &          +uVel(I+1,J,K,bi,bj)
105      &              *(uVel(I+1,J,K,bi,bj)-myPa_U0(I+1,J,K,bi,bj))
106      &              *_hFacW(I+1,J,K,bi,bj)*rAw(I+1,J,bi,bj)
107      &               )
108      &              + (
109      &          vVel(I,J  ,K,bi,bj)
110      &              *(vVel(I,J  ,K,bi,bj)-myPa_V0(I,J  ,K,bi,bj))
111      &              *_hFacS(I, J, K,bi,bj)*rAs(I ,J, bi,bj)
112      &          +vVel(I,J+1,K,bi,bj)
113      &              *(vVel(I,J+1,K,bi,bj)-myPa_V0(I,J+1,K,bi,bj))
114      &              *_hFacS(I,J+1,K,bi,bj)*rAs(I,J+1,bi,bj)
115      &               )        )*_recip_hFacC(I,J,K,bi,bj)
116      &                           * recip_rA(I,J,bi,bj)
117
118
119                keubar(I,J,K,bi,bj) = rhotmp(I,J,K,bi,bj)*0.25*(
120      &              (
121      &          uVel(I  ,J,K,bi,bj)*myPa_U0(I  ,J,K,bi,bj)
122      &              *_hFacW(i ,j, k,bi,bj)*rAw(i ,j, bi,bj)
123      &          +uVel(I+1,J,K,bi,bj)*myPa_U0(I+1,J,K,bi,bj)
124      &              *_hFacW(i+1,j,k,bi,bj)*rAw(i+1,j,bi,bj)
125      &               )
126      &              + (
127      &          vVel(I,J  ,K,bi,bj)*myPa_V0(I,J  ,K,bi,bj)
128      &              *_hFacS(I,J,K,bi,bj)*rAs(I,J,  bi,bj)
129      &          +vVel(I,J+1,K,bi,bj)*myPa_V0(I,J+1,K,bi,bj)
130      &              *_hFacS(I,J+1,K,bi,bj)*rAs(I,J+1,bi,bj)
131      &               )        )*_recip_hFacC(I,J,K,bi,bj)
132      &                           * recip_rA(I,J,bi,bj)
133
134            ENDDO
135          ENDDO
136        ENDDO
137
```

```
138
139 C          Compute weights for UBC
140          DO J=1−OLy,sNy+OLy
141           DO I=1−OLx,sNx+OLx−1
142            za = 0.5 * dxF(I,J,bi,bj) * recip_dxC(I,J,bi,bj)
143            etaupt  = (1.0−za)*etaN(I+1,J,bi,bj) + (za)*etaN(I,J,bi,bj)
144            wu(I,J,1,bi,bj) = ( drF(1) + etaupt )*HFacW(I,J,1,bi,bj)
145            swu(I,J,bi,bj) = wu(I,J,1,bi,bj)
146            ubt(I,J,bi,bj) = wu(I,J,1,bi,bj) * uVel(I,J,1,bi,bj)
147           ENDDO
148          ENDDO
149          DO K=2,Nr
150           DO J=1−OLy,sNy+OLy
151            DO I=1−OLx,sNx+OLx
152            wu(I,J,K,bi,bj) = drF(K) * HFacW(I,J,K,bi,bj)
153            swu(I,J,bi,bj) = swu(I,J,bi,bj) + wu(I,J,K,bi,bj)
154            ubt(I,J,bi,bj) = ubt(I,J,bi,bj)
155        I                     + wu(I,J,K,bi,bj) * uVel(I,J,K,bi,bj)
156            ENDDO
157           ENDDO
158          ENDDO
159 C          Find baroclinic part of U
160          DO K=1,Nr
161           DO J=1−OLy,sNy+OLy
162            DO I=1−OLx,sNx+OLx
163            ubc(I,J,K,bi,bj) = uVel(I,J,K,bi,bj)
164        I                     − (ubt(I,J,bi,bj) / swu(I,J,bi,bj))
165            ubc(I,J,K,bi,bj) = ubc(I,J,K,bi,bj) * maskC(I,J,K,bi,bj)
166            ENDDO
167           ENDDO
168          ENDDO
169
170
171 C          Compute weights for VBC
172          DO J=1−OLy,sNy+OLy−1
173           DO I=1−OLx,sNx+OLx
174            za = 0.5 * dyF(I,J,bi,bj) * recip_dyC(I,J,bi,bj)
175            etavpt  = (1.0−za)*etaN(I,J+1,bi,bj) + (za)*etaN(I,J,bi,bj)
176            wv(I,J,1,bi,bj) = ( drF(1) + etavpt )*HFacS(I,J,1,bi,bj)
177            swv(I,J,bi,bj) = wv(I,J,1,bi,bj)
178            vbt(I,J,bi,bj) = wv(I,J,1,bi,bj) * vVel(I,J,1,bi,bj)
179           ENDDO
180          ENDDO
181          DO K=2,Nr
182           DO J=1−OLy,sNy+OLy
183            DO I=1−OLx,sNx+OLx
184            wv(I,J,K,bi,bj) = drF(K) * HFacS(I,J,K,bi,bj)
185            swv(I,J,bi,bj) = swv(I,J,bi,bj) + wv(I,J,K,bi,bj)
186            vbt(I,J,bi,bj) = vbt(I,J,bi,bj)
187        I                     + wv(I,J,K,bi,bj) * vVel(I,J,K,bi,bj)
188            ENDDO
189           ENDDO
190          ENDDO
191 C          Find baroclinic part of V
```

```
192        DO K=1,Nr
193         DO J=1—OLy,sNy+OLy
194          DO I=1—OLx,sNx+OLx
195           vbc(I,J,K,bi,bj) = vVel(I,J,K,bi,bj)
196     I                       — (vbt(I,J,bi,bj) / swv(I,J,bi,bj))
197           vbc(I,J,K,bi,bj) = vbc(I,J,K,bi,bj) * maskC(I,J,K,bi,bj)
198          ENDDO
199         ENDDO
200        ENDDO
201
202 C       Find pinternal
203        DO J=1—OLy,sNy+OLy
204         DO I=1—OLx,sNx+OLx
205          zzme = rC(1) — etaN(I,J,bi,bj)
206          zdzpe = drC(1) + etaN(I,J,bi,bj)
207          zrhobarzme =  MYPACKAGE_RHOBAR(zzme)
208          pint(I,J,1,bi,bj) =  gravity
209     I                        *(rhotmp(I,J,1,bi,bj) — zrhobarzme)*
          zdzpe
210          pint(I,J,1,bi,bj) = pint(I,J,1,bi,bj) * maskC(I,J,1,bi,bj)
211
212         ENDDO
213        ENDDO
214        DO K=2,Nr
215         DO J=1—OLy,sNy+OLy
216          DO I=1—OLx,sNx+OLx
217           zzme = rC(K) — etaN(I,J,bi,bj)
218           zdzpe = drC(K)  * hFacC(I,J,K,bi,bj)
219           zrhobarzme =  MYPACKAGE_RHOBAR(zzme)
220           pint(I,J,K,bi,bj) =   pint(I,J,K—1,bi,bj) + gravity
221     I                        *(rhotmp(I,J,K,bi,bj)—zrhobarzme)*zdzpe
222           pint(I,J,K,bi,bj) = pint(I,J,K,bi,bj) * maskC(I,J,K,bi,bj)
223
224          ENDDO
225         ENDDO
226        ENDDO
227
228
229 C       Find energy flux in U direction
230        DO J=1—OLy,sNy+OLy
231         DO I=1—OLx,sNx+OLx—1
232           zubcc = 0.5* (ubc(I,J,1,bi,bj) + ubc(I+1,J,1,bi,bj))
233           zdzpe = drC(1) + etaN(I,J,bi,bj)
234      efu2d(I,J,bi,bj) = pint(I,J,1,bi,bj) * zubcc * zdzpe
235         ENDDO
236        ENDDO
237        DO K=2,Nr
238         DO J=1—OLy,sNy+OLy
239          DO I=1—OLx,sNx+OLx—1
240           zubcc = 0.5* (ubc(I,J,K,bi,bj) + ubc(I+1,J,K,bi,bj))
241           zdzpe = drC(K)  * hFacC(I,J,K,bi,bj)
242      efu2d(I,J,bi,bj) = efu2d(I,J,bi,bj)
243     I                        + pint(I,J,K,bi,bj) * zubcc * zdzpe
244           ENDDO
```

```
245            ENDDO
246          ENDDO
247
248 C        Find energy flux in V direction
249          DO J=1-OLy,sNy+OLy-1
250           DO I=1-OLx,sNx+OLx
251             zvbcc = 0.5* (vbc(I,J+1,1,bi,bj) + vbc(I,J,1,bi,bj))
252             zdzpe = drC(1) + etaN(I,J,bi,bj)
253        efv2d(I,J,bi,bj) = pint(I,J,1,bi,bj) * zvbcc * zdzpe
254           ENDDO
255          ENDDO
256          DO K=2,Nr
257           DO J=1-OLy,sNy+OLy-1
258            DO I=1-OLx,sNx+OLx
259             zvbcc = 0.5* (vbc(I,J+1,K,bi,bj) + vbc(I,J,K,bi,bj))
260             zdzpe = drC(K) * hFacC(I,J,K,bi,bj)
261        efv2d(I,J,bi,bj) = efv2d(I,J,bi,bj)
262     I                         + pint(I,J,K,bi,bj) * zvbcc * zdzpe
263            ENDDO
264           ENDDO
265          ENDDO
266
267 C      END LOOP OVER BI,BJ
268         ENDDO
269        ENDDO
270
271
272 C      ! write states
273        CALL DIAGNOSTICS_FILL( petmp, 'POT_E   ',
274     &                         0,Nr, 0, 1, 1, myThid )
275        CALL DIAGNOSTICS_FILL( keuprime, 'KEUPRIME',
276     &                         0,Nr, 0, 1, 1, myThid )
277        CALL DIAGNOSTICS_FILL( keubar, 'KEUBAR  ',
278     &                         0,Nr, 0, 1, 1, myThid )
279        CALL DIAGNOSTICS_FILL( ubc, 'UBC     ',
280     &                         0,Nr, 0, 1, 1, myThid )
281        CALL DIAGNOSTICS_FILL( vbc, 'VBC     ',
282     &                         0,Nr, 0, 1, 1, myThid )
283        CALL DIAGNOSTICS_FILL( pint, 'PINTERN ',
284     &                         0,Nr, 0, 1, 1, myThid )
285        CALL DIAGNOSTICS_FILL( efu2d, 'EFLX_U2D',
286     &                         0, 1, 0, 1, 1, myThid )
287        CALL DIAGNOSTICS_FILL( efv2d, 'EFLX_V2D',
288     &                         0, 1, 0, 1, 1, myThid )
289
290 #endif /* MYPACKAGE_ENERGY */
291
292         ENDIF
293 #endif /* ALLOW_DIAGNOSTICS */
294
295 #endif /* ALLOW_MYPACKAGE */
296
297        RETURN
298        END
```

References

X. Carton. Hydrodynamical Modeling Of Oceanic Vortices. *Surveys in Geophysics*, 22:179–263, 2001. doi: 10.1023/A:1013779219578. 23, 45

E.T. Eady. Long waves and cyclone waves. 1:33–52, 1949. 30

C. Eden. Eddy length scales in the North Atlantic Ocean. *Journal of Geophysical Research (Oceans)*, 112:6004, June 2007. doi: 10.1029/2006JC003901. 21

C. Garrett and W. Munk. Internal Waves in the Ocean. *Annual Review of Fluid Mechanics*, 11:339–369, 1979. doi: 10.1146/annurev.fl.11.010179.002011. 9, 10, 11

A.E. Gill. *Atmosphere-Ocean Dynamics*. International Geophysics Series. Academic Press, 1981. 13

S. Gladyshev, M. Arhan, A. Sokov, and S. Speich. A hydrographic section from South Africa to the southern limit of the Antarctic Circumpolar Current at the Greenwich meridian. *Deep Sea Research Part I: Oceanographic Research*, 55: 1284–1303, October 2008. doi: 10.1016/j.dsr.2008.05.009. 25, 26

V. M. Kamenkovich, M. N. Koshlyakov, and A. S. Monin. *Synoptic Eddies in the Ocean*. D. Reidel Publishing Company, 1986. 28

W. Krauss. Internal tides resulting from the passage of surface tides through an eddy field. *J. Geophys. Res.*, 104:18323–18332, August 1999. doi: 10.1029/ 1999JC900067. iii, 1

W. Krauss, R. Döscher, A. Lehmann, and T. Viehoff. On Eddy scales in the eastern and northern North Atlantic Ocean as a function of latitude. *J. Geophys. Res.*, 95:18049–18056, October 1990. doi: 10.1029/JC095iC10p18049. 21, 24

Wentao Liu. Poincare Waves and Kelvin Waves in a Circular Lake. Master's thesis, University of Waterloo, 2009. 51

John C. Mason and David Handscomb. *Chebyshev polynomials*. Chapman and Hall/CRC, 2003. 18

James C. McWilliams. The Nature and Consequences of Oceanic Eddies. In Matthew W. Hecht and Hiroyasu Hasumi, editors, *Ocean Modeling in an Eddying Regime*, volume 177 of *Geophysical Monograph Series*, pages 5–15. American Geophysical Union, Washington DC, USA, 2008. 21

W. Munk. Internal Waves and Small-Scale Processes. In C. Wunsch and B. Warren, editors, *Evolution of Physical Oceanography*, pages 264–291. MIT Press, 1981. 10

James R. Munroe. Generation of Internal Waves over Idealized 3-D Topography by Tidal Forcing. Master's thesis, University of Waterloo, 2003. 39

R. Ray. Surface manifestation of internal tides in the deep ocean: observations from altimetry and island gauges. *Progress in Oceanography*, 40:135–162, 1997. doi: 10.1016/S0079-6611(97)00025-6. 1, 7

P. Richardson. A census of Meddies tracked by floats. *Progress in Oceanography*, 45:209–250, February 2000. doi: 10.1016/S0079-6611(99)00053-1. 29

R. Shapiro. Smoothing, Filtering, and Boundary Effects. *Reviews of Geophysics*, 8:359–387, 1970. doi: 10.1029/RG008i002p00359. 40

C. J. Talbot and A. Crampton. Application of the Pseudo-Spectral Method to 2D Eigenvalue Problems in Elasticity. *Numerical Algorithms*, 38:95–110, 2005. doi: 10.1007/s11075-004-2860-5. 15, 24

The Ring Group. Gulf Stream Cold-Core Rings: Their Physics, Chemistry, and Biology. *Science*, 212:1091–1100, June 1981. 27

K. R. Thompson and E. Demirov. Skewness of sea level variability of the world's oceans. *Journal of Geophysical Research (Oceans)*, 111:5005, May 2006. doi: 10.1029/2004JC002839. 30, 31

S. A. Thorpe. The Excitation, Dissipation, and Interaction of Internal Waves in the Deep Ocean. *J. Geophys. Res.*, 80:328–338, January 1975. doi: 10.1029/JC080i003p00328. 7, 9

M.-L. Timmermans, J. Toole, A. Proshutinsky, R. Krishfield, and A. Plueddemann. Eddies in the Canada Basin, Arctic Ocean, Observed from Ice-Tethered Profilers. *Journal of Physical Oceanography*, 38:133, 2008. doi: 10.1175/2007JPO3782.1. 29

Lloyd N. Trefethen. *Spectral Methods in MATLAB*. Software, Environments, and Tools. 2000. ISBN 0-89871-465-6. 18

J. A. Weideman and S. C. Reddy. A MATLAB differentiation matrix suite. *ACM Trans. Math. Softw.*, 26(4):465–519, 2000. ISSN 0098-3500. doi: http://doi.acm.org/10.1145/365723.365727. 18